Design and Analysis of Inner Support Structures for Double-Walled Liquid Hydrogen Storage Vessels

Nicolas Renauld

Delft University of Technology

TU Delft

Design and Analysis of Inner Support Structures for Double-Walled Liquid Hydrogen Storage Vessels

by

Nicolas Renauld

to obtain the degree of Master of Science
at the Delft University of Technology,
to be defended publicly on September 30th, 2024.

Student Number:	5762790	
Thesis Duration:	February 2024 - September 2024	
Supervisors:	Dr. Julien van Campen	TU Delft
	Dr. Ashley Chadwick	DLR
	Dr. Lars Brandt	DLR
Thesis committee:	Dr.-Ing. S.G.P. Castro	TU Delft, Chair
	Dr.ir. O.K. Bergsma	TU Delft, External
	Dr.ir. M.F.M. Hoogreef	TU Delft, External

Cover: COPV by DAWN Aerospace [1]

TU Delft DLR AeroDelft

Preface

Working on this thesis was an enjoyable and rewarding experience. The type of engineering work I was exposed to is exactly what I would like to pursue in my career. I found significant satisfaction in tackling challenges and coming up with new or improved designs. It is difficult for me to recall a single moment when I felt unfulfilled or bored with the topic.

I owe much of this positive experience to my TU Delft supervisor, Dr. Julien van Campen. From the outset, he emphasized that "this is your project" and fostered an encouraging environment that allowed me to explore my interests and develop my skills. Julien also facilitated collaboration with DLR (German Aerospace Center) and initiated contact with AeroDelft, which formed the basis of my main design case. I am deeply appreciative of his supervision and support throughout this journey.

I want to also thank my DLR supervisors, Dr. Ashley Chadwick and Dr. Lars Brandt, for their guidance through our dozen or so bi-weekly meetings. Along with the technical support, I also picked up a few personal lessons that I'll carry with me in my career.

I'd like to give a big thank you to László and Dante for reading through my report and giving me such helpful and detailed feedback.

I would like to thank my family back home—my dad, mom, sister, and grandma—for their support. I feel honoured that they made the trip from Canada more than once to visit me in Delft.

I would also like to thank my friends back home in Canada who always welcomed me back with open arms and made me feel deeply supported. A special thanks to Mike, who made the effort to travel all the way from Canada to visit me in the Netherlands and later in Germany. His personal trips to support me and spend cherished moments together meant a lot.

Additionally, I want to express my gratitude to all the amazing people I met here: the gang from the "Dutch Expedition Group", the "Study Group", and the many others who made this journey memorable.

And finally, a heartfelt thank you to Najeeba. From studying for the Fatigue exam in Quarter 1 to wrapping up the last sentence of our theses together, this entire journey has been infinitely more meaningful and enjoyable because of you. Your support, encouragement, and presence have made all the difference, and I truly can't imagine this experience without you by my side.

Nicolas Renauld
Delft, September 2024

> *"A good scientist is a person with original ideas. A good engineer is a person who makes a design that works with as few original ideas as possible."*
>
> – Freeman Dyson

Abstract

Double-walled vessels are recognized as an effective storage solution for liquid hydrogen (LH2) due to their superior thermal insulation. Similar to a thermos flask, the vacuum space between the inner cryogenic vessel and the outer vacuum shell prevents convective heat transfer, which would otherwise result in the rapid boil-off of the stored LH2. A critical component of this technology is the inner support structure which supports the inner vessel within the outer vacuum shell. It must be robust enough to handle operational loads and potential crash events specific to aviation applications, prevent excessive thermo-mechanical stresses caused by the contracting inner vessel, and minimize heat transfer through conduction. Despite its importance, there is a noticeable lack of comprehensive designs and research addressing this component, particularly in the context of aviation.

The primary objective of this thesis is to develop a design methodology for creating effective inner support structures for double-walled vessel technology. The research is grounded in a practical context through a collaboration with AeroDelft, a student team at TU Delft currently retrofitting a Sling 4 aircraft for hydrogen-powered electric flight. As part of the next milestone in their Project Phoenix, AeroDelft aims to store 6 kg of LH2 in a double-walled vessel to meet the mission's requirements.

To begin, functional, operational, and constraint requirements were established for the inner support structure. A baseline design for the inner vessel and outer shell was then developed. Subsequently, four distinct inner support structure concepts were introduced, each with its own design intents and key considerations. These concepts were subjected to various analyses, including modal, thermo-mechanical, crash loads, and heat leakage, to assess their viability and ability to meet essential functional requirements. To determine the most performative design(s), the concepts were evaluated and compared based on the following performance metrics: gravimetric efficiency, heat leakage, safety, and feasibility of manufacturing and assembly.

The analyses demonstrated that all four design concepts meet the essential functional requirements, providing a solid foundation for further development or potential prototyping. While the focus was on a vessel designed for a small aircraft, the methodology and design insights are applicable to larger systems. Hence, this research contributes to advancing cryogenic storage solutions for hydrogen-powered aviation.

Contents

Nomenclature

Abbreviations

Abbreviation	Definition
ASTM	American Society for Testing and Materials
ATP	Automatic Tape Placement
CAD	Computer Aided Design
CFRP	Carbon Fiber Reinforced Polymer
CLT	Classical Lamination Theory
CPV	Composite Pressure Vessel
CTE	Coefficient of Thermal Expansion
CVCM	Collected Volatile Condensable Material
DLR	Deutsches Zentrum für Luft- und Raumfahrt
DoF	Degree of Freedom
FEA	Finite Element Analysis
FEM	Finite Element Method/Model
GH2	Compressed Gaseous Hydrogen
LH2	Liquid Hydrogen
MLI	Multi-Layer Insulation
NASA	National Aeronautics and Space Administration
PEEK	Polyetheretherketone
RML	Recovered Mass Loss
TML	Total Mass Loss
UD	Unidirectional

1

Introduction

1.1. Hydrogen as a Sustainable Fuel for Aviation

Hydrogen as an alternative fuel for aviation is not a novel concept. Research and development efforts date back to the mid-20th century, recognizing its ability to store a lot of energy relative to its weight (high specific energy) and the fact that its combustion produces water vapor [2]. However, challenges such as storage, safety, infrastructure, and cost have historically hindered its adoption. As environmental concerns grow and technological advances are made, hydrogen is once again at the forefront of discussions on sustainable aviation.

An unavoidable downside of hydrogen is its low *volumetric* energy density, which means that the amount of energy that can be contained within a given volume is much lower than that of kerosene (jet fuel). To put this into perspective, Adler and Martins provide a striking comparison [3]:

> "If the energy that a Boeing 777-200ER carries in kerosene were stored as hydrogen at ambient temperature and pressure, the required volume would correspond to about 500 fuselages of this aircraft."

In the face of this fact, there are two practical methods to increase the volumetric energy density for aircraft use:

- **Compressed Gaseous Hydrogen (GH2):** One option is to keep hydrogen in its gaseous state and increase its pressure, usually to 350-700 bar. However, this approach requires thick-walled pressure vessels, which not only add weight but also raise safety concerns.
- **Liquid Hydrogen (LH2):** The alternative is to store hydrogen as a liquid, which exists at -253°C (20K). Operating pressures are relatively low, typically maintained between 2-6 bar. This method significantly improves the volumetric energy density and also keeps the pressure vessels relatively light, making it a more viable solution for aviation.

Table 1.1 provides a comparison of various hydrogen storage options with conventional jet fuel. Another drawback that appears is the gravimetric efficiency, which is a metric used to assess the storage efficiency of a tank. In the case of kerosene tanks, this efficiency is 100% because the tanks are part

of the wing box structure and do not add extra weight. Liquid hydrogen storage solutions provide a substantial advantage over compressed hydrogen in terms of gravimetric efficiency. However, the actual value remains uncertain. Adler and Martins estimate that evolutionary advancements may achieve efficiencies between 25% and 40%, while revolutionary advancements could potentially exceed 70%.

Table 1.1: Comparison of kerosene (Jet A-1) and hydrogen under different storage conditions [4][5][6]

Property	Jet A-1	LH2	GH2 (350 bar)	GH2 (700 bar)
Specific energy [MJ/kg]	43.2	120	120	120
Volumetric energy density [MJ/L]	34.9	8.5	2.9	4.8
Storage temperature [K]	Ambient	20	Ambient	Ambient
Storage pressure [bar]	Ambient	2-6	350	700
Tank gravimetric efficiency [%]	100	30-90	1-15	1-15

1.2. Double-Walled Vessels for LH2 Storage

While making use of liquid hydrogen improves on the issue of volumetric energy density and gravimetric efficiency, it also introduces several challenges related to storing a cryogenic liquid. These challenges include maintaining effective thermal insulation, selecting appropriate materials, and ensuring structural integrity at extremely low temperatures. Addressing these issues is crucial for the design and safety of hydrogen-powered aircraft.

In this context, double-walled vessels are recognized as effective storage solutions due to their superior thermal insulation capabilities. A critical component of these vessels is the inner support structure, which supports the inner vessel within the outer vacuum shell. Designing this support structure is not a trivial task due to several conflicting requirements. It must endure various loads, such as vibrations and crash forces, while also accommodating thermal movements to prevent excessive stress on the components. Additionally, it must be thermally efficient to minimize heat leakage through conduction.

The safety and performance of double-walled LH2 storage vessels heavily depend on the proper functioning of this inner support structure. Despite its importance, there is a noticeable lack of detailed designs and research addressing this component. Therefore, this thesis aims to develop a double-walled vessel for LH2 storage in aircraft, with a particular focus on the design of the inner support structure.

1.3. Collaboration with AeroDelft & DLR

To ground this research in a practical context, a collaboration with AeroDelft was established. AeroDelft, an ambitious student team at TU Delft, is dedicated to demonstrating the feasibility of emission-free aviation through the development of a liquid hydrogen-powered electric aircraft (Figure 1.1a). Their current project, Phoenix, involves converting a Sling 4 aircraft to be powered by hydrogen fuel cells. This manned liquid hydrogen plane is expected to take flight in 2026.

The Deutsches Zentrum für Luft- und Raumfahrt (DLR) is the German national research and technology center for aerospace. This project also involved collaboration with DLR at their Stuttgart and Augsburg locations, where expert external supervision was provided. Among many other areas of research, DLR focuses on the development of next-generation components for space and aviation, with a particular

interest in sustainable and lightweight solutions (Figure 1.1b). Their expertise in materials and technologies relevant to liquid hydrogen-powered aircraft played a key role in guiding the design and evaluation of the inner support structures for the double-walled vessel.

(a) AeroDelft's retrofitted Sling 4 hydrogen-powered electric aircraft [7]

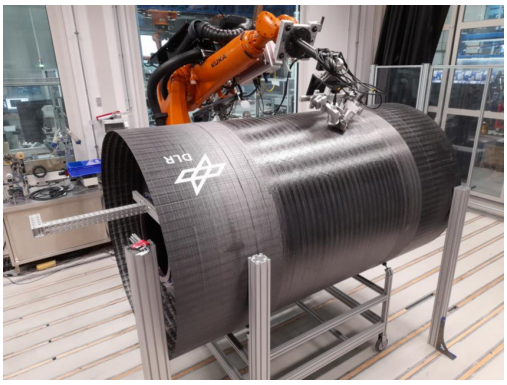

(b) Composite hydrogen tank inspection at DLR Augsburg [8]

Figure 1.1: Illustrative images of project collaborators and their technologies

1.4. Project Goal and Outline

The objective of this thesis is to develop a double-walled vessel for liquid hydrogen storage in aircraft, with a particular emphasis on establishing a design methodology for creating effective inner support structures. The main design case centers on AeroDelft's Sling 4 hydrogen-powered electric aircraft, which requires a vessel large enough to store around 6 kg of LH2. However, these concepts can also be used for vessels in larger commuter planes. Additionally, the design methodology discussed in the thesis can offer insights into designing larger tanks, including those used in retrofitted commercial aircraft.

With this, the project is organized into the following 10 chapters in the thesis document:

Chapter 2 Provides a literature review, detailing the key research areas essential for developing a double-walled vessel and the primary considerations for the inner support structure.

Chapter 3: Outlines the methodology used to develop concepts for the inner support structure. It also specifies the relevant project requirements.

Chapter 4: Focuses on developing a baseline design for the inner vessel and outer shell.

Chapter 5: Presents the conceptual designs for the inner support structures, including four distinct designs. Each design is discussed in terms of its overview, design intent, and key considerations.

Chapter 6: Prepares the groundwork for Chapter 7 by discussing the modelling and analysis approach.

Chapter 7: Demonstrates the analysis results of the inner support structure designs.

Chapter 8: Evaluates and compares the designs against key performance metrics.

Chapters 9 and 10: Conclude the thesis and offer recommendations for future work.

2

Double-Walled Vessel Technology

A double-walled vessel is a type of fuel containment system used to thermally isolate cryogenics. Similar to a thermos flask, a vacuum space between the two walls prevents convective heat transfer which would otherwise result in a high boil-off of the stored cryogenic. At its core, this construction consists of an inner pressure vessel, an inner support structure, and an outer vacuum shell, as demonstrated by the simplified schematic of Figure 2.1

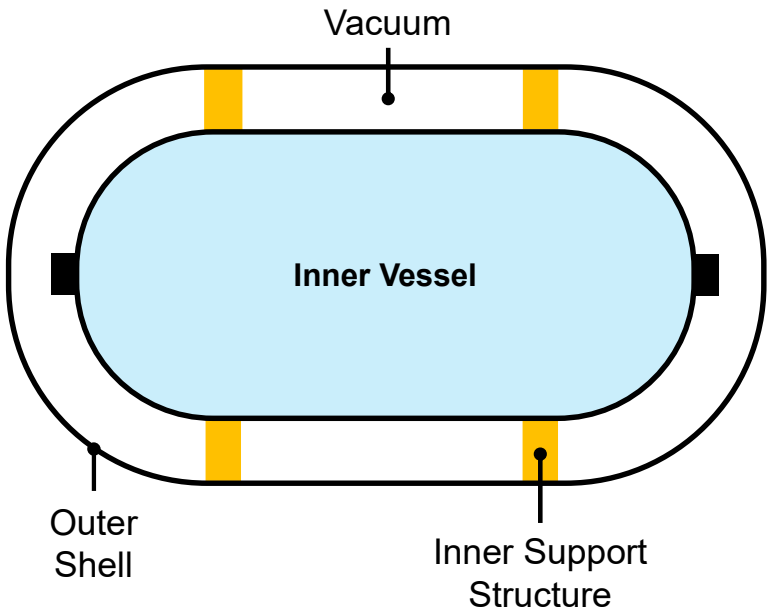

Figure 2.1: Simplified schematic a of double-walled vessel

In the literature review of this study, a comprehensive examination of several key topics relevant to the development of double-walled vacuum insulated vessels for LH2 storage will be undertaken. The review begins with an exploration of various composite pressure vessel analysis methods, including the implications of pressure and temperature variations on the free expansion of vessels. This is followed by a detailed examination of considerations for using composites at cryogenic temperatures, where material behavior under extreme cold poses unique challenges. Additionally, thermodynamic considerations

essential for understanding the operational environment of these storage systems are analyzed. The discussion extends to heat transfer and its mitigation strategies to enhance both efficiency and safety of these vessels. A critical aspect of the review involves analyzing the effect of hydrogen permeation on the vacuum space, which significantly influences overall heat transfer and vessel performance. Existing designs for the inner support structure are reviewed, identifying strengths and areas for improvement. Miscellaneous considerations that may impact the design and functionality of these vessels are also discussed. Finally, the research questions and sub-questions are laid out as the foundation for the rest of the research project.

2.1. Composite Pressure Vessel (CPV) Technology

2.1.1. CPV Analysis Methods

A pressure vessel, under internal pressure only, is subjected to a hoop stress, N_θ, and a longitudinal stress, N_x, (Figure 2.2, top). For a cylindrical construction, the hoop stress is twice that of the longitudinal stress. Analytically, researchers and designers make use of three main analysis methods for the preliminary sizing and layup of filament wound pressure vessels: netting analysis, classical lamination theory, and thick cylinder theory [9].

In netting analysis (Figure 2.2, bottom), the principle of static equilibrium is used and assumes that (a) only the fibers carry the load, and (b) there are no out-of-plane bending moments and inter-laminar shearing stresses [10]. For the cylindrical portion of the CPV, netting analysis typically begins by calculating the amount of helical layers required to withstand the longitudinal stress followed by calculating the necessary amount of hoop layers required to withstand the remaining hoop stress. Hence, this latter step subtracts the amount of hoop stress already carried by the helical layers.

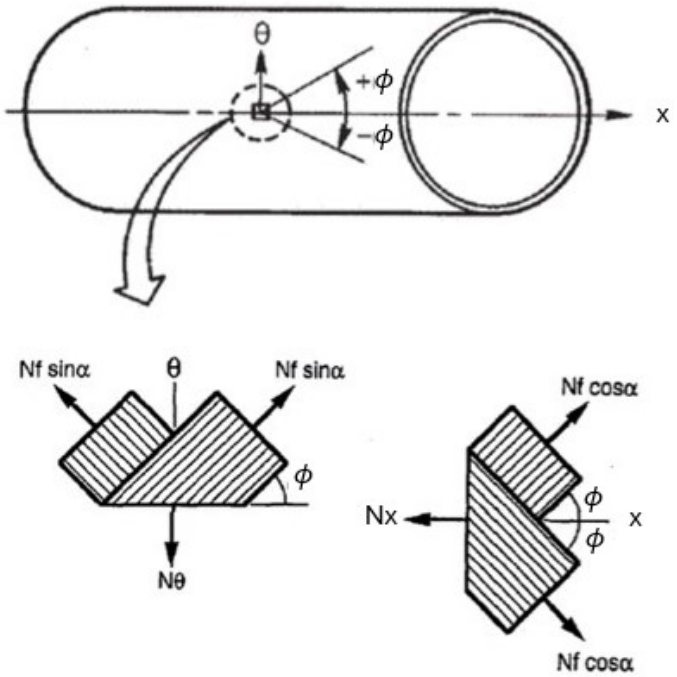

Figure 2.2: Static equilibrium of fibers used in netting analysis, adapted from [11]

.

Classical lamination theory (CLT) is an analytical method that predicts the displacement, strains, and stresses that develop in a laminate when mechanically and thermally loaded. A detailed explanation of the derivation is well beyond the scope of this chapter, but at its essence, CLT results in the construction of of an ABD matrix for a given laminate. The ABD matrix, otherwise known at the laminate stiffness matrix, establishes a relationship between the loads applied to a laminate and the resulting deformations [12].

An interesting aspect of CLT is its potential for design optimization. The terms in the ABD matrix can be expressed in lamination parameters and material invariants, making it easier to use in engineering optimization problems where the A, B, and D matrices are part of the objective function. Gürdal et al. demonstrated that this method can be employed to maximize in-plane stiffness, buckling load, natural frequency, and strength [13].

The main limitation of CLT is that it fails to capture the varying strain/stress distribution through the thickness of thick-walled pressure vessels, as it assumes plane stress. Figure 2.3 demonstrates that for a thick cylinders, when $r_o/r_i > 1.1$, the radial and hoop stress will be greatest in the inner surface and decrease along the radial direction [14].

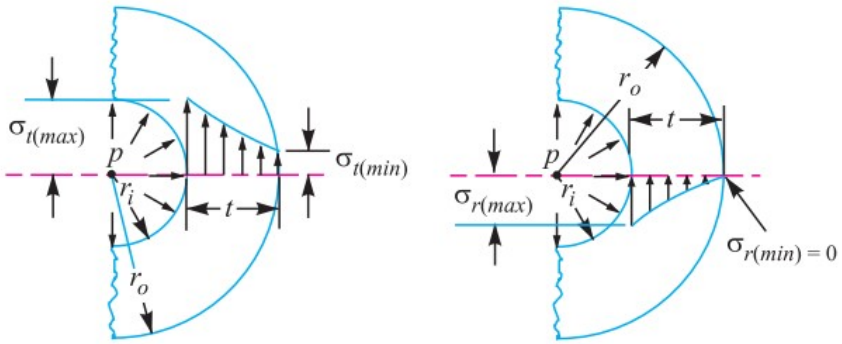

Figure 2.3: Stress distribution in thick cylinders, adapted from [14]

.

Capturing this effect requires using thick-cylinder theory based on 3D elasticity as developed by Xia [15]. Briefly, using cylindrical coordinates and defining the equilibrium equations in terms of the stress-strain and strain-displacement relations, leads to a second order differential equation. The solution to this differential equation is a displacement function and with appropriate boundary conditions, Xia then defines equations for the radial stress, hoop stress, longitudinal stress, and in-plane shear stress for every layer in the cylinder. Poorte et al. utilized this method in their exploration of cryo-compressed vacuum insulated storage vessels within the primary structure of aircraft [16].

2.1.2. Free Expansion of a Vessel Due to Pressure and Temperature Variations

Understanding how much a vessel expands or contracts in response to variations in pressure and temperature is an important consideration, especially for the design of the inner support structure. Even small dimensional variations, on the order of a few millimeters, can cause significant thermo-mechanical stresses in the support structure and the associated connections, potentially leading to material failure. This section provides analytical equations used to estimate the free expansion of *thin-walled* vessels due to pressure and temperature variations. Hence, thick-cylinder theory, as briefly discussed in the previous section, is not considered. For simplicity, the cylindrical portion away from the end caps, subjected to a hoop stress, N_θ, and a longitudinal stress, N_x, is considered. In addition, the laminate

is assumed to be symmetric and balanced to further simplify the expressions.

Free expansion of a composite cylindrical shell due to pressure

The free radial and longitudinal expansion of a thin-walled composite vessel from internal pressure are expressed as:

$$\delta_x^P = \frac{PRL}{t}\left(\frac{1}{2\overline{E}_x} - \frac{\overline{\nu}_{\theta x}}{\overline{E}_\theta}\right), \qquad \delta_\theta^P = \frac{PR^2}{t}\left(\frac{1}{\overline{E}_\theta} - \frac{\overline{\nu}_{x\theta}}{2\overline{E}_x}\right) \tag{2.1}$$

where,

- $\delta_x^P, \delta_\theta^P$ = Longitudinal and radial expansion from internal pressure [mm]
- P = Internal pressure [MPa]
- R, t, L = Radius, thickness, and length of vessel, respectively [mm]
- $\overline{E}_x, \overline{E}_\theta$ = Laminate's effective extensional modulus along x and θ, respectively [MPa]
- Effective $\overline{\nu}_{\theta x}, \overline{\nu}_{x\theta}$ = Laminate's effective Poisson's ratios

The effective laminate properties shown from equations 2.1 are defined as [12]:

$$\overline{E}_x = \frac{A_{11}A_{22} - A_{12}^2}{A_{22}t}, \qquad \overline{E}_y = \frac{A_{11}A_{22} - A_{12}^2}{A_{11}t}, \qquad \overline{\nu}_{x\theta} = \frac{A_{12}}{A_{22}}, \qquad \overline{\nu}_{\theta x} = \frac{A_{12}}{A_{11}} \tag{2.2}$$

In which the A_{ij} terms are the extensional stiffness terms the laminate's ABD matrix.

Free expansion of a composite cylindrical shell from a uniform temperature change

To begin, the coefficients of thermal expansion (CTE) of a unidirectional (UD) composite ply are known along the fiber direction (α_1) and perpendicular to the fiber (α_2). These values represent an averaged effect, reflecting the combined contributions of both the fiber and matrix materials within the composite. For a UD ply with fibers oriented at ϕ with respect to to the cylinder's axis (Figure 2.2), the ply's CTE in the $x - \phi$ coordinate frame is defined as [12]:

$$\alpha_x = \alpha_1 \cos^2\phi + \alpha_2 \sin^2\phi, \qquad a_\theta = \alpha_1 \sin^2\phi + \alpha_2 \cos^2\phi, \qquad \alpha_{x\theta} = 2(\alpha_1 - \alpha_2)\cos\phi \sin\phi \tag{2.3}$$

Where the $\alpha_{x\theta}$ can be viewed as the CTE responsible for shearing the ply from a temperature change. Note that this would only come in play when the fibres are oriented at some angle with respect to the x-axis. Hyer [12] offers a straightforward example in his textbook (pp.199-201) that highlights the influence of fiber orientation on the development of free thermal strains in composite materials. The effective laminate CTEs in the longitudinal and hoop directions for a symmetric and balanced laminate are given by [12]:

$$\overline{\alpha}_x = \frac{A_{22}\hat{N}_x^T - A_{12}\hat{N}_\theta^T}{A_{11}A_{22} - A_{12}^2}, \qquad \overline{\alpha}_\theta = \frac{A_{11}\hat{N}_\theta^T - A_{12}\hat{N}_x^T}{A_{11}A_{22} - A_{12}^2} \tag{2.4}$$

Where the $\hat{N}_x^T$ and $\hat{N}_\theta^T$ are unit thermal stress resultants defined as [12]:

$$\hat{N}_x^T = \sum_{k=1}^{N}(\overline{Q}_{11_k}\alpha_x + \overline{Q}_{12_k}\alpha_\theta + \overline{Q}_{16_k}\alpha_{x\theta})(t_k), \qquad \hat{N}_\theta^T = \sum_{k=1}^{N}(\overline{Q}_{12_k}\alpha_x + \overline{Q}_{22_k}\alpha_\theta + \overline{Q}_{26_k}\alpha_{x\theta})(t_k) \tag{2.5}$$

With $\overline{Q}_{ij_k}$ being the transformed stiffness term for ply number k with thickness t_k.

Then, the free longitudinal and radial expansion of a thin-walled composite vessel from a uniform temperature change are:

$$\delta_x^T = \overline{\alpha}_x L \Delta T, \qquad \delta_\theta^T = \overline{\alpha}_\theta R \Delta T \tag{2.6}$$

where,

- $\delta_x^T, \delta_\theta^T$ = Longitudinal and radial expansion from a uniform temperature [mm]
- R, L = Radius and length of vessel, respectively [mm]
- ΔT = Uniform change in temperature [k]

Several remarks can be made to conclude this sub-section:

(a) The free-expansion behaviour of a non-symmetric and non-balanced laminate from a uniform temperature change will result in twisting and bending of the cylinder due to coupling effects.

(b) The analysis only works for uniform temperature changes throughout the cylinder's thickness. More specifically, the unit thermal stress resultants from equation 2.5 are not valid if the temperature varies through the thickness [12].

(c) Despite a uniform temperature change, thermal stresses develop through the laminate as a consequence of the varying thermal expansions layer by layer.

(d) The material CTE values are assumed constant, but can vary with temperature.

(e) The analysis above is only valid for thin shells and not thick vessels.

(f) External constraints, such as rings around the circumference, prevent free thermal expansion and cause more complicated stress states.

(g) Certain composite layups can lead to one of the laminate CTE from equation 2.4 to be zero. This can potentially be useful for some applications, but it comes at the cost of high stresses within the layers.

2.1.3. Considerations for Composites at Cryogenic Temperatures

The composite material of the inner vessel will be exposed to cryogenic temperatures, reaching as low as 20K (-253°C). This is a significantly large ΔT considering that the vessel begins at room temperature. It is therefore essential to have some understanding of the general impact of cryogenic temperatures on composite materials and possible implications.

Thermal expansion mismatch between fibres and matrix

The fibres and resin in composite materials exhibit significant differences in their coefficients of thermal expansion (CTEs). Upon cooling, carbon fibers expand along their length while contracting transversely [17]. The surrounding resin contracts to a greater extent creating a compressive stress state along the fiber-resin interface, as depicted by Figure 2.4. Furthermore, the resin undergoes a considerable loss of ductility at cryogenic temperatures. Finally, as mentioned in remark c) of the previous subsection, thermal stresses will occur in the layers and at their interfaces. These combined effects contribute to the formation of cracks within the composite matrix.

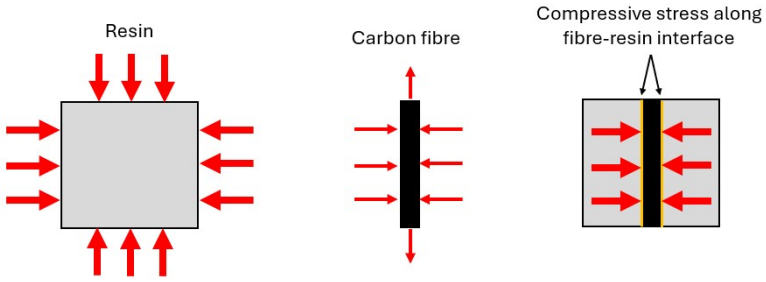

Figure 2.4: Compressive stress state along the fibre-resin interface, adapted from [18]

Permeability

Permeability is influenced by both molecular features and micro-structural features of the material. Diffusion is the process where atoms pass through the material, while leaks are caused by interconnected micro-cracks, which are influenced by both the arrangement of the layers and the thickness of the plies in the laminate [19] (Figure 2.5). The rate of diffusion through a polymer matrix depends on a number of factors which include the fibre volume, fibre type, resin type, and temperature [20]. For instance, rates of diffusion are higher in amorphous regions compared to crystalline regions because the molecular structure in amorphous areas is less packed, allowing for easier movement of gas molecules [21].

Leakage resulting from gas flow through interconnected micro-cracks is generally much greater than that caused by diffusion alone [20]. Permeability of the hydrogen within the vacuum space can lead to non-negligible gas conduction which effectively increases the heat transfer to the stored hydrogen. This concept is explored more thoroughly in section 2.3.2.

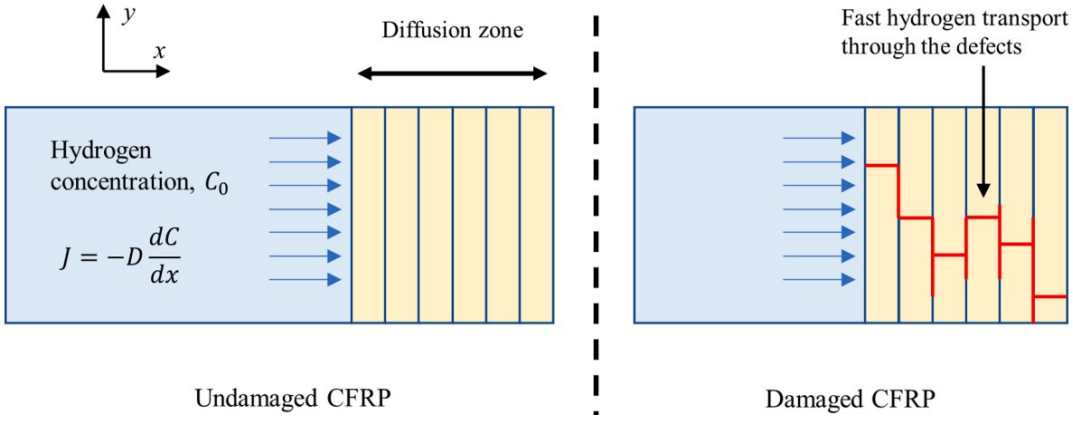

Figure 2.5: Diffusion mechanism in damaged and undamaged CFRP [19]

Research by Flanagan et al. investigated different types of carbon fibres and matrix combinations, revealing that cracks can develop even after the initial cool-down cycle [20]. Continuous thermal cycling leads to an increase in crack density or the elongation of existing cracks. In this study, PEEK with AS4 fibers (AS4-PEEK) was identified as a promising material for cryogenic storage tanks due to its resistance to micro-cracking, even after cryogenic thermal cycling. Table 2.1 summarizes the leak rates for AS4-PEEK in standard cubic centimeters per square meter per second (Scc/sm²). Notably, the leakage for undamaged[1] samples at cryogenic temperatures is two orders of magnitude lower compared to room temperature.

[1] In this context, ”undamaged” means that the micro-crack networks did not fully propagate through the entire thickness of the laminate, preventing the formation of a connected leak path.

Parameters	
Material	AS4-PEEK
Testing pressure [bar]	1
t_{ref} [mm]	1.1
Condition	**Leak Rate [Scc/sm^2]**
Un-cycled, tested at 293K	8.5×10^{-5}
Un-cycled, tested at 77K	6.5×10^{-7}
(1x) 293K-77K cycle, tested at 293K	8.5×10^{-5}
(10x) 293K-77K cycles, tested at 293K	8.5×10^{-5}
(30x) 293K-77K cycles, tested at 293K	1×10^{-4}

Table 2.1: Leak rates of AS4-PEEK under various conditions (compiled from [20])

Other points worth mentioning include:

(a) The leak rate, as measured in Scc/sm², is shown to be proportional to the pressure difference and inversely proportional to the material thickness [20].

(b) Leak rate values shown on Table 2.1 are from samples manufactured using an autoclave. Laser-assisted ATP consolidation may be prone to defects, potentially resulting in higher leak rates.

(c) In addition, helium was used as a test gas since it produces similar permeability results to hydrogen given similar molecular diameters.

(d) Katsivalis et al. investigated the permeability of thin-ply composites under mechanical loading and demonstrated that applying a tensile pre-loading up to 1.4% tensile strain did not induce micro-cracks or damage that would accelerate the diffusion process [19]. However, a primary limitation of their study is that it does not account for the complex stress state experienced by composite materials at cryogenic temperatures.

Coefficient of thermal expansion and conductivity

Other properties worth mentioning is the varying conductivity and thermal expansion with decreasing temperature, depicted through Figure 2.6. Notably, from 77K down to 4K, the thermal conductivity of the various UD-composites drop considerably. Carbon fibres, regardless of the temperature, have lowest thermal expansions among the various fiber materials.

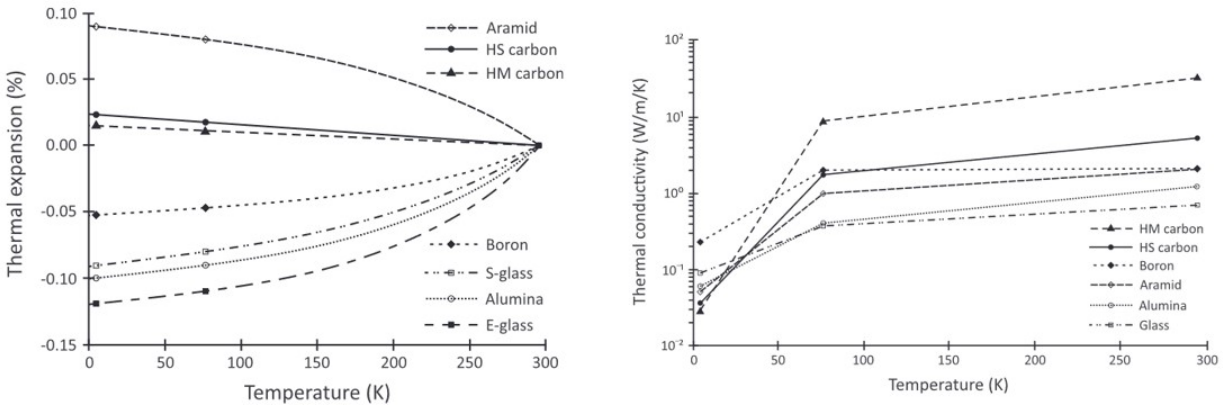

Figure 2.6: Thermal expansion [17] and conductivity [22] of varying UD-composites with decreasing temperature

2.2. Thermodynamic Considerations

One of the design considerations of a vessel used to store cryogenics, such as LH2, is the parasitic (i.e. unwanted) heat leak into the vessel. With time, this heat leak raises the internal energy of the LH2 and begins to vaporize it. When the tank is left dormant, this vaporization leads to a self-pressurization eventually leading to the venting of gaseous hydrogen. Stated explicitly, parasitic heat leakage leads to the loss of hydrogen. The following presents fundamental thermodynamic definitions, followed by an analysis method from literature used to capture the rate of pressure change over time in the vessel.

2.2.1. Energy Transfer Mechanisms

The total energy E of a stationary system is equal to to the internal energy of the fluid, U. Hence, the change in the total energy of a system is identical to the change of its internal energy. There exists three mechanisms of energy transfer that can produce this change, (1) heat transfer (2) work transfer and (3) mass flow. Each of these will briefly be defined from the perspective of an LH2 vessel.

Heat transfer, Q, increases the energy of the molecules and therefore the internal energy of the system. The mechanism behind this energy interaction is due to a temperature difference between the fluid and the surroundings[2]. For instance, the heat transfer making its way to the fluid through the support structure.

Work transfer, W, increases the internal energy from a mechanism crossing a system's boundary such as an electrical heater.

Mass flow in or out of the vessel increases or decreases the system's internal energy since mass, by definition, carries energy with it.

With this, the net change in the fluid's energy can be described by the first law of thermodynamics, as shown in the following equation:

$$E_{in} - E_{out} = (Q_{in} - Q_{out}) + (W_{in} - W_{out}) - (E_{mass,in} - E_{mass,out}) = \Delta E_{system}$$

2.2.2. Self-Pressurization from Heat Leakage

Ahluwalia and Peng developed a dynamic model used to characterize cryogenic hydrogen in an insulated pressure vessel [23]. The main assumptions in their model are as follows:

- Kinetic and potential energies of the hydrogen flowing in and out of the tank are neglected.
- When hydrogen in the tank is present in both liquid and gas forms, the mixture exists in a saturated liquid-vapor state, where both phases are in equilibrium. Therefore, the pressures and temperatures within the tank are homogeneous.

For a dormant tank, there is no mass flow in or out of the tank ($\dot{m}_{H_2}^{in} = \dot{m}_{H_2}^{out} = 0$) and no work from an electric heating element ($W_{electric} = 0$). Although, the presence of heat leakage from the environment is unavoidable ($Q_{leak} \neq 0$). In differential form, the energy balance used for the dormancy model is given as:

$$\frac{d(m_{H_2} u_{H_2})}{dt} = Q_{leak} \tag{2.7}$$

[2]The surroundings refer to everything external to the inner vessel that contains the hydrogen, as illustrated in Figure 2.1.

Namely, the change in the system's internal energy is solely caused by parasitic heat leakage from the environment. The complete derivation by Ahluwalia and Peng is meticulously laid out in Appendix A to ensure the ease of understanding for the reader. The derivation for a dormant tank experiencing heat leakage leads to the following system of coupled ordinary differential equations. These equations describe the transient evolution of pressure, temperature, and the masses of gas and liquid phases.

$$\begin{aligned}
\frac{dP}{dt} &= \left(\frac{dP_s}{dT}\right)\frac{dT}{dt} \\
\frac{dm_g}{dt} &= \frac{\frac{m_g}{\rho_g^2}\left(\left(\frac{\partial \rho_g}{\partial P}\right)_T \frac{dP}{dt} + \left(\frac{\partial \rho_g}{\partial T}\right)_P \frac{dT}{dt}\right) + \frac{m_l}{\rho_l^2}\left(\left(\frac{\partial \rho_l}{\partial P}\right)_T \frac{dP}{dt} + \left(\frac{\partial \rho_l}{\partial T}\right)_P \frac{dT}{dt}\right)}{\left(\frac{1}{\rho_g} - \frac{1}{\rho_l}\right)} \\
\frac{dm_l}{dt} &= -\frac{dm_g}{dt} \\
\frac{dT}{dt} &= \frac{(h_1 - h_g)\frac{dm_g}{dt} + Q_{leak}}{m_l\left(\frac{\partial h_l}{\partial T}\right)_P + m_g\left(\frac{\partial h_g}{\partial T}\right)_P + \left(m_l\left(\frac{\partial h_l}{\partial P}\right)_T + m_g\left(\frac{\partial h_g}{\partial T}\right) - V\right)\frac{dP_s}{dT}}
\end{aligned} \tag{2.8}$$

where,

- h_g, h_l = Specific enthalpy of gaseous hydrogen and mass of liquid hydrogen, respectively [J/kg]
- m_g, m_l = Mass of gaseous hydrogen and mass of liquid hydrogen, respectively [kg]
- P = Homogeneous pressure [Pa]
- P_s = Saturated pressure at a given temperature [Pa]
- Q_{leak} = Heat leakage in the tank [W]
- ρ_g, ρ_l = Density of gaseous hydrogen and mass of liquid hydrogen, respectively [kg/m^3]
- T = Homogeneous temperature [K]
- u_{H_2}= Specific internal energy of the total hydrogen in the tank [J/kg]
- V = Internal volume of the tank [m^3]

This model is particularly useful for estimating the venting time after refueling. Once refueling is complete, the vent lines are closed, and the tank pressure starts at 1 bar, with the temperature corresponding to the saturated vapor temperature of the LH2 at the current pressure. By knowing the vessel's volume, the initial mass of the stored LH2, an estimated value for heat leakage, and the pressure relief point, it becomes possible to estimate the time until venting. This is important for several reasons:

First, operational requirements may dictate that no venting occurs within a certain time frame after refueling to prevent hydrogen release near workers. Second, in periods of dormancy where some LH2 remains in the tank, it is essential to understand how long the tank can avoid venting. This is especially important for minimizing thermal cycling of the inner vessel, as thermal cycling can exacerbate the formation of micro-cracks. As discussed in Section 2.1.3, composite inner vessels are prone to cracking, and the combination of thermal cycling and internal pressure increases the density of these cracks and the risk of them interconnecting. Evidently, these considerations highlight the importance of having thermally efficient solutions. While knowing the amount of heat transfer entering the tank is important, understanding the time-to-vent is far more critical for optimizing the vessel's thermal performance.

Drawbacks to the homogeneous model

Homogeneous self-pressurization models, such as Ahluwalia and Peng's [23], discussed above, neglect the effect of thermal stratification, which refers to the formation of distinct thermal layers in the liquid hydrogen. This occurs due to convective flow along the tank walls, causing the lighter, warmer

fluid to accumulate at the top, where it comes into contact with the gaseous hydrogen. This warmer upper layer accelerates the pressure rise due to increased vapor generation [24]. The extent of thermal stratification is influenced by several factors, including the rate of heat transfer into the tank, the specific location of heat application, and the volume of propellant present in the tank [24].

Van Dresar et al. investigated the effects of thermal stratification in a 4.89 m^3 spherical tank at various initial liquid hydrogen fill levels and heat fluxes [25]. As shown in Figure 2.7, their results indicate that thermal stratification led to experimental pressure rise rates approximately 1.5 to 2 times higher than those predicted by the homogeneous model. This also explains why researchers who use make use of the homogeneous assumption such as Verstraete [26], Lin et al. [27], and Onorato [28], apply a correction factor of 2 when calculating the pressure rise in an LH2 tank.

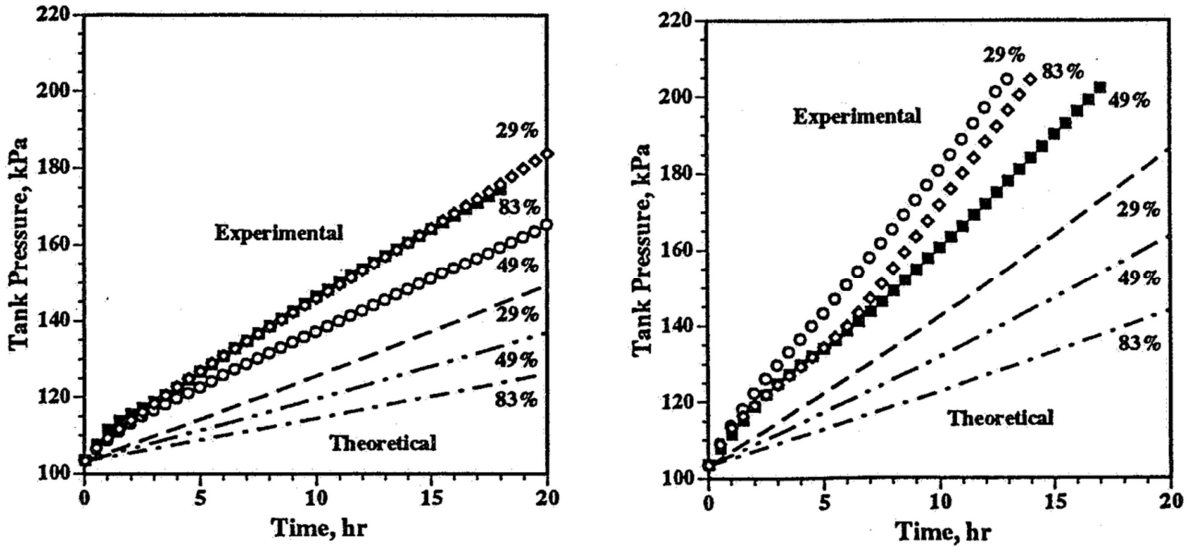

a) $q = 2.0\ W/m^2$ b) $q = 3.5\ W/m^2$

Figure 2.7: Experimental results for self-pressurization in a 4.89m^3 LH2 tank compared to predictions from the theoretical homogeneous model [**van_dresar_self-pressurizationof_1992**]

Mitigating the effects of thermal stratification has been achieved by mixing the stratified LH2. For example, NASA employed a mixing strategy that uses an axial jet mixer installed at the bottom of the tank [29]. The jet sprays cooler fluid upward, exposing it to the ullage, where the vapor at the liquid-gas interface condenses, resulting in a reduction of overall tank pressure. However, mixing cannot be repeated indefinitely, as the fluid will eventually reach a uniform temperature, at which point further mixing will no longer result in depressurization [27]. This method has been proven to be advantageous for long-duration space missions and could similarly benefit LH2 tanks in aircraft applications during extended periods of dormancy.

Other important trends

Observing the plots from Figure 2.7, the following general trends are noted:

(a) A larger heat flux results in a shorter vent time, highlighting the importance of implementing thermally efficient solutions to mitigate this effect.

(b) A higher initial LH2 fill percentage leads to a slower rate of pressure rise, as a greater mass of LH2 requires more time to absorb the necessary enthalpy of vaporization.

(c) Consistent with point (b), for a given heat leakage and initial fill percentage, a larger vessel volume results in a longer time before vent.

2.3. Heat Transfer Fundamentals and Mitigation Strategies

Section 2.2 highlighted the significance of minimizing heat leakage from the inner vessel's surroundings. Specifically, the vaporization of liquid hydrogen and subsequent venting losses result from this heat input. This section discusses the mechanisms responsible for heat transfer and explores methods to mitigate it. The basic heat transfer theory in the following few subsections are taken from fundamental textbooks such as Bergman et al. [30] and Çengel et al. [31].

2.3.1. Heat Transfer Mechanisms

Conduction

Conduction involves the transmission of energy from highly energetic particles within a substance to neighboring particles with lower energy levels due to interactions among these particles. The rate of heat conduction, Q_{cond} [W], is proportional to the temperature difference across a material, ΔT [K], and the the heat transfer area,A [m^2], but inversely proportional to length, L [m], of the layer. Specifically,

$$Q_{cond} = k \cdot A \frac{\Delta T}{L} \tag{2.9}$$

Considering the viewpoint of a double-walled LH2 vessel with a significantly large temperature differential (ΔT), reducing heat conductivity through the inner support structure involves several strategies:

- Reducing its cross-sectional area
- Increasing the length of the support, thereby elongating the thermal path
- Selecting materials characterized by significantly low thermal conductivities

Thermal radiation

Thermal radiation is the transfer of heat energy in the form of electromagnetic waves emitted by a body due to its temperature. All bodies with a temperature above absolute zero emit thermal radiation. The thermal radiation that is emitted from a body's surface is given by:

$$Q_{rad,emit} = \epsilon A_s \sigma T_s^4 \tag{2.10}$$

where,

- $Q_{rad,emit}$ = Emitted rate of thermal radiation from a surface [W]
- ϵ = emissivity of the surface
- $\sigma = 5.670x10^{-8}$, Stefan-Boltzmann constant [W/m^2K^4]
- A_s = Surface area [m^2]
- T_s = Temperature of the surface [k]

The radiative heat transfer between the outer vacuum shell and significantly cold inner vessel can be calculated using Gebhart factors [32]. This method assumes that surfaces are non-transparent, emitting and reflecting radiation diffusely[3] and uniformly. Additionally, each surface within the enclosure is assumed to have a uniform temperature, with radiation both entering and leaving each surface evenly distributed. The Gebhart factor,B_{ij}, provides the fraction of radiation emitted by surface surface i absorbed by surface j, including all reflections. Expressed as:

[3]Diffusely implies radiation is reflecting or emitting equally in all directions

$$B_{ij} = F_{ij} \cdot \epsilon_j + \sum_{k=1}^{N}((1-\epsilon_k) \cdot F_{ik} \cdot B_{kj}) \tag{2.11}$$

where,

- F_{ij} = View factor from surface i to j
- ϵ = Emissivity of the surface
- N = Amount of surfaces in the enclosure

The energy transfer from surface i to surface j is formulated as:

$$Q_{ij} = \epsilon_i \cdot A_i \cdot B_{ij} \cdot \sigma \cdot (T_i^4 - T_j^4) = -(\epsilon_j \cdot A_j \cdot B_{ji} \cdot \sigma \cdot (T_j^4 - T_i^4)) \tag{2.12}$$

where,

- ϵ = Emissivity of surface
- A = Area of surface [m^2]
- B = Gebhart factor
- $\sigma = 5.670x10^{-8}$, Stefan-Boltzmann constant [W/m^2K^4]
- T_i,T_j = Temperatures of surface i and j, respectively [K]

The appendix provides more elaborate steps used to calculate the radiative heat transfer from the outer vessel to the inner vessel using the Gebhart method. It should be noted that the method, as presented, neglects the presence of piping within the vacuum space as this would make the analysis substantially more complex.

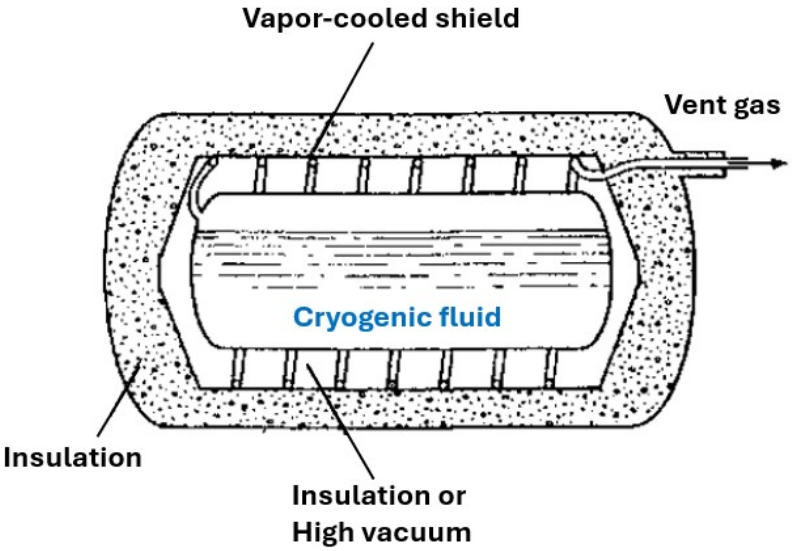

Figure 2.8: Vapor cooled shield [33]

For a given surface area, equation 2.12 dictates that thermal radiation can be lowered by minimizing the temperature difference between the walls and reducing the emissitivity. The former can be achieved with a cooled shield as depicted by Figure 2.8. The later typically involves using multi-layer-insulation (MLI). MLI is a thermal control technology commonly used to minimize heat transfer. It consists of

multiple layers of highly reflective materials, separated by low-conductivity spacers, which significantly reduce radiative heat transfer by reflecting infrared radiation between the layers [34]. This technique is widely employed in vacuum environments to insulate liquid hydrogen tanks and other low-temperature storage systems [33].

2.3.2. Hydrogen Permeation: Effect on Vacuum and Heat Transfer

The space between the inner tank and outer shell is critical in preventing heat transfer towards the stored hydrogen. Initially, it may seem that the thermal links in this space are solely the heat conductivity through the support structure and the radiation between the two walls. However, this would only hold true if a perfect vacuum was maintained at all times. Permeation of hydrogen through the CPV into this vacuum space will lead to an additional thermal link, which effectively increases the total heat flow to the stored liquid hydrogen.

The heat transfer mechanism in an imperfect vacuum is categorized as gas conduction [33]. Gas conduction is divided into two main categories: viscous state (continuum) and molecular state gas conduction. The determination of the state is characterized by the molecule's mean free path ,λ, and a characteristic length, δ,

In the context of a vacuum-insulated vessel, δ equals the perpendicular distance between the inner vessel and the outer shell. λ is the gas molecule's mean free path, or the average path length between successive collisions with neighboring molecules, expressed as[4]:

$$\lambda = \frac{k_b T}{\sqrt{2}\pi d^2 P} \tag{2.13}$$

where,

- $k_b = 1.380649 \times 10^{-23}$, is Boltzmann's constant [J/K]
- T = Temperature of the gas [K]
- P = Pressure of the gas [P]
- d = kinetic diameter of a particle [m]

Equation 2.13 notably demonstrates that the mean free path is inversely proportional to the the pressure within the vacuum space.

Viscous state gas conduction (λ << δ)

When the mean free path is much smaller than the vacuum gap, viscous gas conduction predominates. In this regime, molecules form distinct layers within the vacuum space. The collective behavior of these molecules facilitates heat transfer, as they continuously collide with neighboring molecules, transporting thermal energy from the warmer boundary to the cooler one [35]. The kinetic theory of gases has established that the gas conductivity in this viscous state remains consistent across a wide pressure spectrum, ranging from approximately 1 atmosphere down to $10\mu mHg - 100\mu mHg$ [33]. This is shown by the straight line (λ « δ) in Figure 2.9.

The conductivity of the gas in the viscous state is given by [35]:

$$k_{viscous} = \frac{1}{4}(9\gamma - 5)\eta C_v \tag{2.14}$$

where,

[4] https://www.omnicalculator.com/physics/mean-free-path#mean-free-path-definition

- $k_{viscous}$ = Thermal conductivity of the gas in the viscous state [W/m·K]
- γ = Ratio of specific heats
- η = Viscosity of the gas [Pa-s]
- C_v = Specific heat at constant volume of the gas [J/kg·K]

Remarking that equation 2.14 is independent from pressure, but varies with temperature since $\eta = f(T)$.

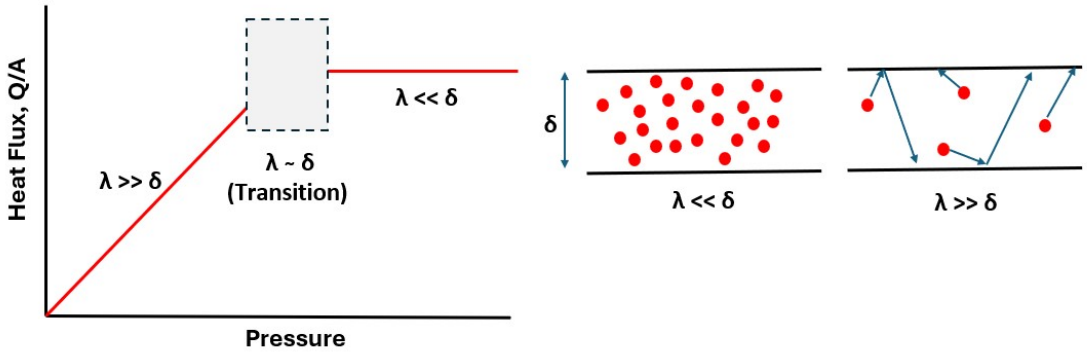

Figure 2.9: Heat transfer vs. pressure, λ = mean free path and δ = vacuum gap/space. Adapted from [33]

.

Molecular state gas conduction (λ >> δ)

At sufficiently low pressures, when the mean free path exceeds the size of the vacuum gap, gas molecules experience fewer collisions with each other and increasingly interact with the container walls instead [35]. In this state, individual molecules transport heat from one boundary to another. The resulting gas conduction is dependent on pressure, as depicted in Figure 2.9.

Molecular state gas conduction makes use of an accommodation coefficient, which represents the proportion of energy that is effectively transferred between colliding molecules and a surface, compared to the energy that would be hypothetically transferred if the molecules attained complete thermal equilibrium with the surface [35]. Is is defined as:

$$\alpha = \frac{T_i - T_r}{T_i - T_w} \tag{2.15}$$

where,

- T_i = Temperature of the impinging molecules [K]
- T_r = Temperature of the reflected molecules [K]
- T_w = Temperature of the wall [K]

$\alpha = 1$ implies that the impinging molecules reach thermal equilibrium with the wall before escaping ($T_r = T_w$). In contrast, $\alpha = 0$, signifies the impinging molecules do not undergo a change in energy prior to being reflected ($T_r = T_i$).

Some approximate values for accommodation coefficients for air and hydrogen are shown in Table 2.2 [33]. In general, α tends to 1 when the wall temperature approaches the condensing temperature of the gas.

T_w [K]	Hydrogen	Air
300	0.3	0.8-0.9
76	0.5	1
20	1	-

Table 2.2: Accommodation coefficients for hydrogen and air at different wall temperatures [33]

The molecular state heat flux is defined by Corrucini [36] as:

$$Q_{ms-hf} = \left(\left(\frac{\gamma+1}{\gamma-1} \right) \sqrt{\frac{R}{8\pi MT}} \right) \alpha P (T_2 - T_1) \tag{2.16}$$

where,

- Q_{ms-hf} = Molecular state heat flux [W/m^2]
- γ = c_p/c_v, Specific heat ratio of the gas, assumed constant
- R = 8.3145, is the molar gas constant [J/mol· K]
- P = Pressure of the gas [Pa]
- M = Molecular weight of the gas [kg/mol]
- T = Effective temperature of the non-equilibrium gas, defined in the appendix [K]
- T_1 = Surface temperature of the inner wall [K]
- T_2 = Surface temperature of the outer wall [k]
- A_1 = Surface area of the inner wall [m^2]
- A_1 = Surface area of the outer wall [m^2]
- α = Overall accommodation coefficient, define below

The overall accommodation coefficient from equation 2.16 is outlined as [36]:

$$\alpha = \frac{a_1 a_2}{a_2 + a_1(1-a_2)\frac{A_i}{A_2}} \tag{2.17}$$

with α_1 and α_2 being the accommodation coefficients of the inner and outer wall respectively. It is worth noting that equation 2.16 varies with pressure as described before (Figure 2.9).

A few remarks can be made to conclude this section:

(a) From Equation 2.14, it can be observed that the conductivity of lighter gases exceeds that of heavier gases significantly. For example, at $0°$C (273 K), the conductivity of H_2 is $175\ mW/mK$, whereas that of air is $24.7\ mW/mK$ [35]. This bears significant implications for design considerations. In scenarios where the pressure within the vacuum space gradually increases due to hydrogen permeation, resulting in a condition where the mean free path (λ) is less than the characteristic length (δ), the heat transferred to the stored hydrogen becomes substantially elevated.

(b) The graph depicted in Figure 2.9 illustrates a transitional phase existing between the viscous and molecular states. This transitional phase, approximately defined between $0.01 < \lambda/\delta < 0.3$, signifies a mixed viscous-molecular behaviour. Employing molecular state gas conduction theory will overestimate the heat conduction within this range [37].

2.3.3. Material Outgassing in Vacuum Environments

When placed in a vacuum environment, polymer-based materials undergo outgassing, releasing substances in gaseous form. These materials are commonly employed in thermal insulation, adhesives, and the matrix for composites. Outgassing products may include organic constituents inherent to the material or gases previously absorbed, such as oxygen, nitrogen, and carbon dioxide [38].

For vacuum insulated vessels, outgassing can affect the vacuum, potentially increasing gas conduction. In addition, condensation on thermal control coatings is also a concern, as it alters the rates of energy absorption and emission by the coatings [38]. Typically, the outgassing of polymeric materials intensifies with increasing temperature and decreasing pressure.

ASTM E595 classifies outgassing using three metrics [39]:

- **Total Mass Loss (TML)**: The percentage of mass reduction of a material sample, calculated by comparing its initial mass to the mass remaining after precisely 24 hours in a high-vacuum setting maintained at a temperature of 125°C.
- **Recovered Mass Loss (RML)**: The percentage of mass decrease of a material sample observed after 24 hours in a high-vacuum environment at a temperature of 125°C, followed by an additional 24-hour period of conditioning at a relative humidity (rH) of 55% and a temperature of 22°C.
- **Collected Volatile Condensable Material (CVCM)**: The mass of contaminants accumulated on a collector plate, measured at a temperature of 25°C, following 24 hours in a high-vacuum environment over a material sample, expressed as a percentage.

As outlined in the ASTM E595 standard, the Total Mass Loss (TML) should not exceed 1% by specimen weight, while the Collected Volatile Condensable Materials (CVCM) must remain below 0.1%. Pastore et al. explored the impact on polymeric composites when subjected to thermal-vacuum conditions [40]. They found that for a carbon-fiber polymer composite matrix, the TML is 1.07 % $\pm$ 0.11, the CVCM is 0.07 % $\pm$ 0.01, and the RML is 0.66 % $\pm$ 0.09.

As a general point, choosing materials with very low outgassing should be a requirement for the support structure found in the vacuum space.

2.4. Inner Support Structure

It is difficult to find comprehensive designs for the internal support structures of vacuum-insulated vessels in academic literature. While some companies involved in cryogenics may showcase their designs, these images are often unclear and lack detail for proprietary reasons. The examples presented in this section are a combination of commercial designs and some work found in literature.

2.4.1. Main Functional Requirements

The most basic function of the inner support structure of a double-walled vessel is to support the inner vessel within the outer vacuum shell. The important design aspects of this component can be defined by three main functional requirements: (1) Limit thermo-mechanical stresses caused by large temperature gradients between the inner vessel and outer shell by incorporating flexibility and allowing for movement, (2) minimizing thermal conductivity, and (3) ensuring sufficient strength and rigidity. The complexity of designing a support structure lies in the fact that these aspects are conflicting in nature.

For instance, designing for rigidity conflicts with the need to provide flexibility. Similarly, designing to minimize thermal conductivity can lead to the development of steep temperature gradients, which exacerbates the challenge of accommodating the difference in thermal contraction.

2.4.2. Existing Design Concepts

Boss-linked support structure

Figure 2.10 demonstrates a support structure design used for liquid hydrogen storage for long haul trucks [41] . In this example, a dome-shaped support structure is welded to the boss of the inner tank. The outer shell is subsequently welded to this support structure. The support structure in this application facilitates the assembly since it acts as a jig during the welding process. At first sight, the outer shell may not appear structural sound, but it is mostly only subjected to 1 atmosphere of pressure. If need be, the addition of a stiffening ring placed at center of the outer shell increases the buckling capacity.

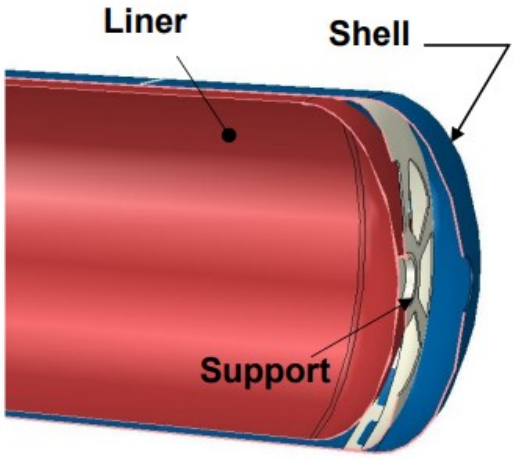

Figure 2.10: Boss-linked support structure used for long haul trucks, aluminum construction

An anticipated failure mode with this design which is not explicitly addressed by [41] stems from the large temperature gradient between the inner shell (or liner in Figure 2.10) and the outer shell. Aluminum exhibits a high CTE implying a significant contraction of the inner shell during LH2 filling. This causes the support structure to be pulled inward, generating a bending moment and shear stress at the outer shell's weld. This particular scenario emphasizes the importance of first the first functional requirement in that the support structure needs to account for the difference in thermal contraction between the inner and outer vessels.

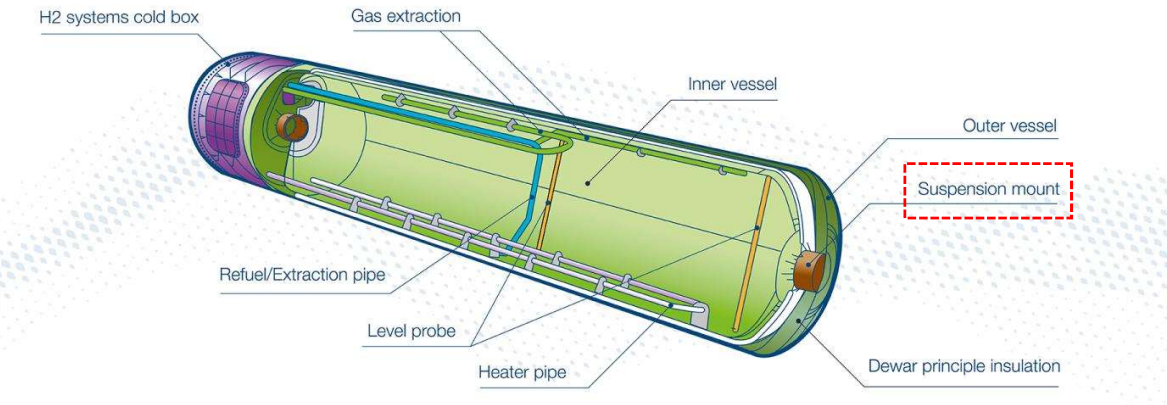

Figure 2.11: Suspension mount using the domes of each vessel [42]

Airbus has explored the use of a boss-linked suspension mount in the development of their hydrogen-powered commercial aircraft, as shown in Figure 2.11 [42]. This attachment method appears to be space-efficient. However, a significant drawback is the short thermal path between the inner and outer vessels. Additionally, the design raises concerns about how thermo-mechanical stresses will be miti-

gated, given the seemingly rigid suspension (though it should be noted that the provided image offers limited details). Regardless, its simplicity makes it a design worthy of further investigation.

Kevlar support structure

Kevlar, a material produced and patented by DuPont, is classified as an aramid, known for its high strength to weight ratio and its low conductivity. Kevlar comes in three variations: 29,49, and 149, each with slightly different properties. Kevlar-29, for instance, has a tensile strength of 2.9 GPa, a specific gravity of 1.44, and a low thermal conductivity [44]. Hence, Kevlar chords/wiring/straps have been used in applications requiring very low heat leakage and low weights [43][45][46][47].

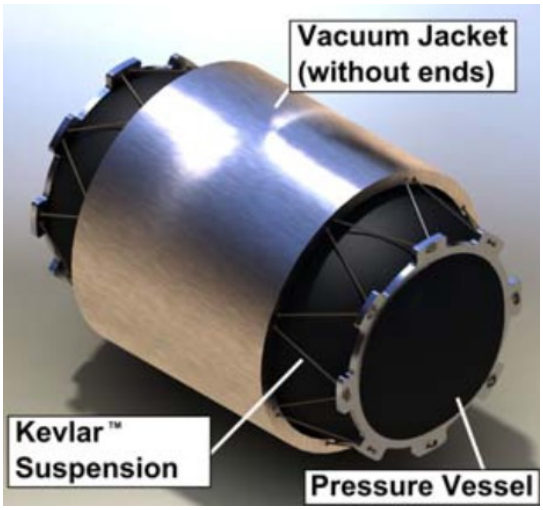

Figure 2.12: Kevlar suspension system for a hydrogen tank [43]

An interesting concept from Raymond and Reiter [43] at the Jet Propulsion Laboratory involves using Kevlar ropes to thermally isolate a hydrogen storage tank, as shown in Figure 2.12. In this design, Kevlar ropes are woven from the outer shell (vacuum jacket) to the inner vessel, creating a zigzagging pattern. Rings with slots are installed at the domes of the inner vessel, serving as anchor points for the Kevlar. Due to Kevlar's minimal compressive stiffness, the ropes are placed under tension, resulting in the inner vessel experiencing compression. This can be advantageous as it counteracts the tension generated by the internal pressure.

The Kevlar design concept depicted in Figure 2.12, as outlined in source [43], exhibits several areas where further elaboration and refinement are warranted. Firstly, the method of attachment to the vacuum jacket remains unclear based on the provided image. Additionally, although the application pertains to "hydrogen fueled vehicles", the specific context of its application is not explicitly stated. The analysis primarily focuses on thermodynamics and heat transfer, particularly in calculating boil-off losses stemming from heat leakage from the Kevlar support structure, with the tank assumed to be in a dormant state without fuel extraction. Notably, no stress analysis was conducted on this Kevlar concept. While a brief mention is made regarding its ability to withstand inertial loads, details regarding the source and magnitude of these loads are lacking. Despite efforts to investigate further developments on this concept, no significant progress has been identified since its publication. Nonetheless, given its potential significance, it remains a concept worthy of further exploration and development.

Polymer support blocks and rings

Researchers trying to tackle the issue of limiting heat leakage from the inner support structure of vacuum insulated vessels have looked into the use of blocks with good thermal insulation properties in a setup configuration to Figure 2.13 a).

Lisowski et al. compared different support materials: Polyamide, Tarnamid, Textolite, Teflon, Polycarbonate [48]. They were concerned with the design of a metal tank for transporting liquefied gases with boiling temperatures down to -196°C. In this study, Polycarbonate was the best solution, preventing the most amount of heat leak. The analysis was validated experimentally with liquid hydrogen using a 6-meter long container.

Czyżycki [49] proposed a composite support structure made of alternating polyamide and thin steel layers as shown by 2.13 c). The motivation behind this construction was to take advantage of the thermal contact conductance which acts as a barrier to heat transfer. The numerical results from this study demonstrated that having these steel layers decreased the heat flux as compared to a monolithic polyamide block. Czyżycki did not validate this proposed design experimentally.

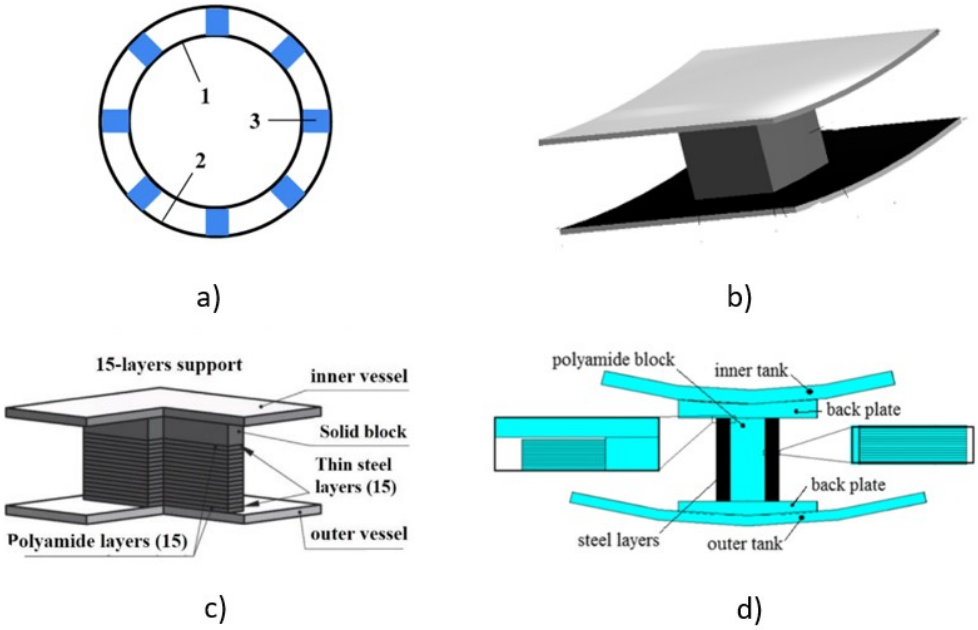

Figure 2.13: a) 1- inner vessel, 2- outer vessel, 3- supporting blocks, b) Close-up of Supporting block [48], b) Polyamide-steel block design [49], d) alternative polyamide-steel block design d) [50]

Norouzifard et al. raised concerns about the effectiveness of Czyżycki's design. They argued that since polyamide is much softer in comparison with steel, the pressure applied on the block from the weight of the inner vessel would drive the contact surface ratio to unity [50]. In other words, as the size of the vessel increases, the static pressure applied on Czyżycki's supports would increase the contact conductance to a point where a monolithic polyamide block would perform better.

Norouzifard et al. therefore proposed a new design shown by figure 2.13 d). They suggest using a solid polyamide block with layered steel plates on both sides of the block. A small gap is left between the back plates and the steel plates. Hence, the polyamide block carries the static pressure load from the weight of the inner vessel. In the event of any dynamic loading, the steel plates would come into effect to support the polyamide block. However, it is worth noting that this design has not yet been validated experimentally.

Raymond and Reiter, the researchers that investigated the Kevlar design, also looked into using G10 (Fiberglass w/ epoxy) support rings for thermal isolation [43] (Figure 2.14). The application of support rings can facilitate the assembly process and provide support to the vacuum jacket against buckling caused by 1 atm of pressure. However, the research conducted by Raymond and Reiter indicates that the use of G-10 support rings was found to have a total heat transfer 38-44 percent higher than that of the Kevlar design. Tzoumakis et al. proposed using rings made of PEEK with a I-beam cross section [51]. In this later study, the inner and outer vessel material is a 2219 aluminium alloy.

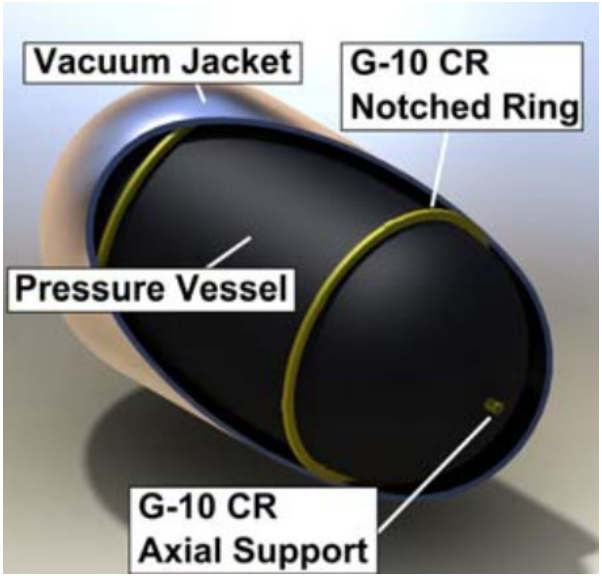

Figure 2.14: G10 (Fiberglass w/ epoxy) support ring for thermal isolation [43]

Springs

Nitin et al. optimized steel helical springs for the support structure of a 2-meter-long Dewar used for LOX storage [52]. Their analysis resulted in a spring design with a heat leakage of 1.9 W, likely due to the longer thermal path in a coil spring compared to a straight rod.

However, the design in Figure 2.15 has limitations: it is intended for a stationary Dewar, and the length of the springs do not seem to provide sufficient stiffness and stability, which could be problematic under the dynamic loads experienced in an aircraft. Initial observations suggest that even minor dynamic oscillations of an aircraft can induce resonance with such a suspension system.

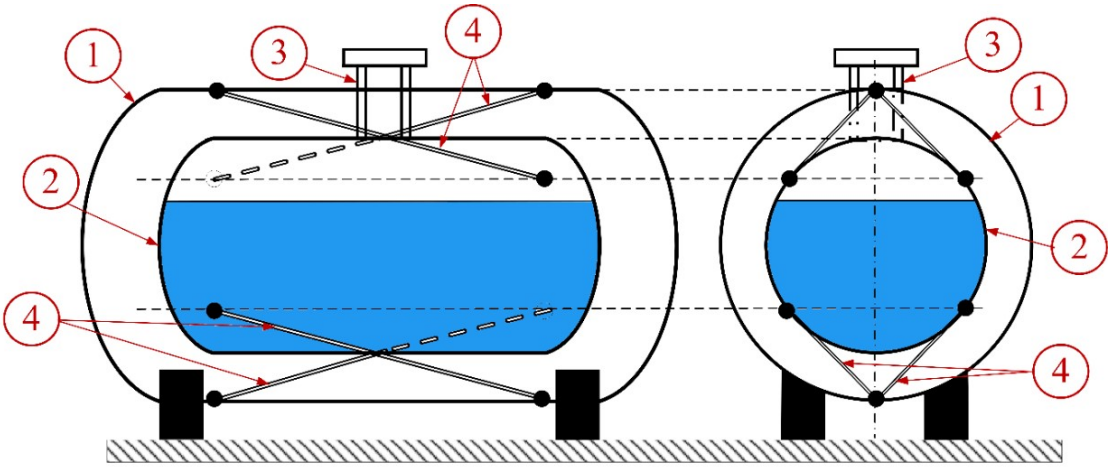

Figure 2.15: Dewar design with coiled springs (1)- Outer vessel, (2)- Inner vessel, (3)- Input/output vent, (4)- Coiled springs [52]

2.4.3. Drawing Inspiration from other Applications

In designing inner support structures for double-walled LH2 vessels, inspiration can be drawn from other applications with similar requirements. Key insights include design features, attachment methods, and design intents in response to similar functional needs. Examples from both industry and literature are provided below.

Flexure brackets for spacecraft satellite systems

Many spacecraft satellites require structural brackets that have similar functional requirements as the ones listed for the inner support structure of an LH2 vessel. Figure 2.16 below shows a satellite assembly comprising an antenna, a rotatory actuator, and a structural support bracket. During launch, satellite assemblies experience an aggressive loading environment. In orbit, the sun's heat flux causes large temperature gradients to develop between the antenna and the rotary actuator, with the rotary actuator being hidden in the antenna's shadow. As a result, the structural bracket must be designed to be compliant enough to account for the difference in thermal contraction between the antenna and rotary actuator, while providing enough rigidity and strength against the launch loading environment.

In this particular application shown by Figure 2.16, the bracket is a short and tapered cone, a structurally efficient shape that provides rigidity. At the same time, a cutout pattern is implemented between each bolted connection, which allows for the necessary compliance in both the radial and axial directions. This example demonstrates the ingenuity used by spacecraft designers to overcome conflicting requirements.

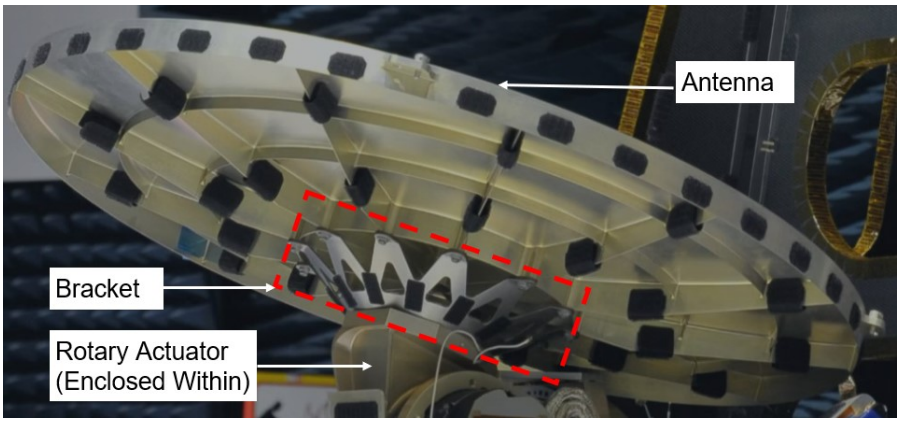

Figure 2.16: Flexure bracket for a spacecraft satellite

The primary difference between the flexure bracket in Figure 2.16 and an inner support structure for LH2 storage lies in their view on heat transfer. In space applications, high-conductivity materials for flex brackets can be advantageous, as they reduce the temperature gradient between intermediate components, which is beneficial from a thermoelastic perspective. However, for hydrogen storage, the inner support structure must resist heat conduction to prevent LH2 from boiling off.

Insulating suspension systems using kinematic mounts

A kinematic mount is a mount that restricts all six degrees of freedom (three translational and three rotational) from moving, without redundancy. Such a mount was designed by Voellmer et al. to suspend a salt pill rigidly in an adiabatic demagnetization refrigerator (Figure 2.17 top) [46]. In this design, the top end of the salt pill is constrained against the three translation directions and against an axial rotation. The bottom end of the salt pill is constrained in the plane normal to the axis, ensuring all motion is restrained, without redundancy.

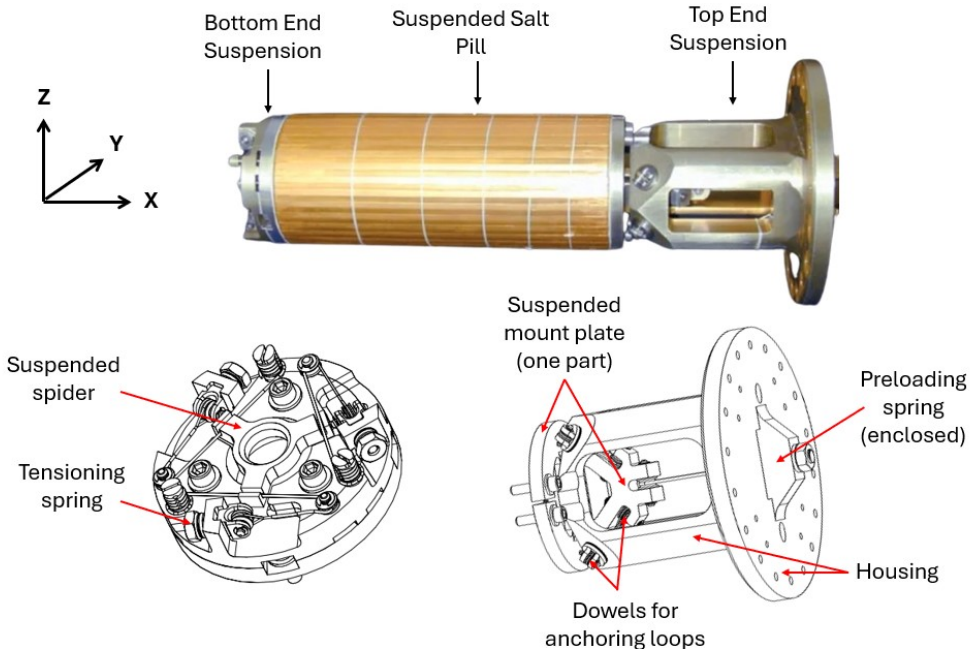

Figure 2.17: Top: Suspended salt pill. **Bottom:** detailed view of bottom and top end suspension. Adapted from: [46],[53].

The bottom two images in Figure 2.17 provide a more detailed view of how the restraints are implemented. To explain briefly, for the top end suspension, a mount plate is suspended within the housing, thanks to a set of Kevlar ropes that are under tension. A preloaded spring ensures constant tension in the assembly. At the bottom, three sets of single Degree of Constraint tensile mounts center a suspended spider that is responsible for restraining the motion perpendicular to the salt pill's axis.

The key advantage of a kinematic mount-type suspension system is that it restrains the six degrees of freedom only once. This is important because it avoids inducing stress by over-constraining any specific degree of freedom. For instance, if the salt pill contracts along its axis due to a temperature change, the system would allow this motion from the bottom end. Consequently, the setup depicted in Figure 2.17 offers valuable insights for suspending the inner CPV in a double-walled vessel design.

Dewar supports for space applications

Kitle performed research for the internal supports used for cryogenic flight Dewars [54] (Figure 2.18). The dewars must meet minimum natural frequency requirements for rocket transportation and prevent heat leaks during operation. Kitle's paper compared the use of struts and straps for supporting the inner liquid helium vessel. Briefly, struts are thin wall cylindrical tubes with end fittings attached at each end. Spherical bearings are used at both ends to ensure the moments are released and only axial loads are carried. A strap is made from two parallel sections secured at both ends with loops and dowel pins.

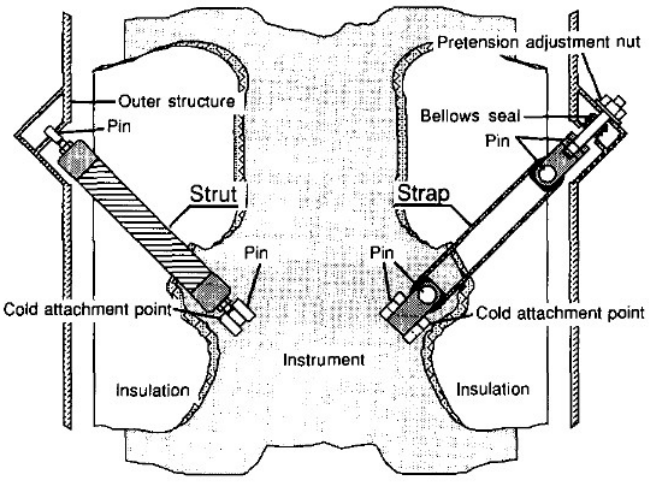

Figure 2.18: Comparison of struts and straps for cryogenic flight Dewars [54]

The insights gained from this paper are attachment methods and general design considerations for the placement and orientation of struts and straps.

Some conclusions from this paper include:

(a) Struts should be used in strength limiting cases.

(b) Straps perform better in resonant frequency limiting cases.

2.5. Miscellaneous Considerations

The following section addresses additional considerations that are relevant to double-walled vessels.

2.5.1. Bonding and Low Temperature Concerns

Attachment of the support structure to the inner vessel and outer vacuum shell can be accomplished through adhesive bonding. While bonding is typically not allowed for aircraft certification, it could be a feasible option for a test prototype. One concern is the substantial temperature drop ($\Delta T \approx -270°C$) that an adhesive bond on the inner vessel would experience.

Researchers from the Fermi National Accelerator Laboratory tested three adhesives from ambient (295K) down to 100K: Tra-Con F113, Epotek 301-2, and Hysol 9361 [55]. Table 2.3 summarizes the Elastic Modulus, Poisson's Ratio, the maximum stress of the three adhesives between ambient and 100K. Table 2.4 summarizes the CTE of the three adhesives between 250K and 100K. The elastic modulus and the strength increase substantially. The CTE is shown to decrease with decreasing temperatures.

Property	Tra-Con F113			Epotek 301-2			Hysol 9361		
	295K	100K	Percent change	295K	100K	Percent change	295K	100K	Percent change
Elastic Modulus (MPa)	2461	7627	210%	3665	6995	91%	1067	7807	632%
Poisson's Ratio	0.401	0.348	-13%	0.401	0.348	-13%	0.401	0.348	-13%
Maximum stress* (MPa)	18	49	179%	26	47	81%	8	29	266%
* Stress at 0.68% strain from a uni-axial tension test, not the ultimate tensile strength.									

Table 2.3: Properties of three different adhesives at ambient and 100K [55]

Temperature	CTEs (mm/mm-K)		
	Tra-Con F113	Epotek 301-2	Hysol 9361
250 K	7.26E-05	6.28E-05	1.04E-04
100K	5.49E-05	4.95E-05	6.82E-05
Percent change	-24%	-21%	-34%

Table 2.4: Coefficient of expansion of three different adhesives at 250K and 100K [55]

The study concluded that none of the proposed epoxies meet the NASA guideline for epoxy joints, which requires a safety factor of 2 on the stress [55]. One main reason is that the adhesive's coefficients of thermal expansion (CTEs) are too high compared to those of the substrates. Additionally, the increase in elastic modulus at cryogenic temperatures also leads to higher stress in the adhesive.

A potential candidate for an adhesive subjected to cryogenic temperatures down to 20K is MASTERBOND's EP30LTE-LO[5], which is claimed to have a very low CTE. The technical data sheet asserts the following properties at *ambient* temperatures:

- **Tensile modulus** = 3793 to 4138 MPa
- **Tensile strength** = 41.4 to 48.3 MPa
- **Coefficient of thermal expansion** = 1.5 to 1.8E-5 mm/mm°C

It could be interesting to get a sense of the magnitude of stress from a uniform temperature drop while using the EP30LTE-LO adhesive. Considering an adhesive between two identical substrates, making a symmetric and balance laminate, as demonstrated by Figure 2.19. Using the unit thermal stress resultants defined by equation 2.5, the in-plane strains are calculated as follows:

$$\epsilon_x = (a_{11}\hat{N}_x^T + a_{12}\hat{N}_\theta^T)\Delta T, \qquad \epsilon_\theta = (a_{12}\hat{N}_x^T + a_{22}\hat{N}_\theta^T)\Delta T \tag{2.18}$$

Where the a_{11}, a_{12}, and a_{22} terms are compliance matrix terms found by taking the inverse of the A matrix in the context of classical lamination theory. The in-plane stresses within the adhesive layer are then found through:

$$\sigma_x = \epsilon_x \overline{Q}_{11}(Ad) + \epsilon_\theta \overline{Q}_{12}(Ad), \qquad \sigma_\theta = \epsilon_x \overline{Q}_{12}(Ad) + \epsilon_\theta \overline{Q}_{22}(Ad) \tag{2.19}$$

With $\overline{Q}_{ij}(Ad)$ being the transformed stiffness terms of the adhesive layer.

Figure 2.19: Adhesive between two substrates

Table 2.5 demonstrates the in-plane stresses in the EPO30LTE-LO adhesive resulting from a uniform temperature drop of ΔT = -270°C for different substrates. The calculations assume constant properties for the Tensile Modulus, Poisson's ratio, and CTE because data for the EPO30LTE-LO is limited to room temperature. It is difficult to determine whether the calculations are conservative or not. This is because CTE is known to decrease with decreasing temperature, which reduces stress, while the modulus increases, leading to an increase in stress. Additionally, the adhesive strength also increases with decreasing temperature, which helps prevent failure.

Substrates	Adhesive	In-plane stress (Adhesive)
Aluminum CTE = 2.3E-5 mm/mm/°C	EP30LTE-LO CTE = 1.5E-5 mm/mm/°C	$\sigma_x = \sigma_\theta =$ -13.5 MPa
CFRP Fabric CTE ≈ 0 (both directions)	EP30LTE-LO CTE = 1.5E-5 mm/mm/°C	$\sigma_x = \sigma_\theta =$ 25.2 MPa

Table 2.5: In-plane adhesive stresses for different substrates, subjected to uniform $\Delta T = -270°C$

[5] https://www.masterbond.com/tds/ep30lte-lo?matchtype=&network=g&device=c&adposition=&keyword=&gad_source=1&gclid=Cj0KCQjw9vqyBhCKARIsAIIcLMEp3XXP_v9fStkIWfj7Mw7rcnR87VOSEVz9wf0q2fT7kBmjgbxQutMaAuK5EALw_wcB

These results demonstrate that EPO30LTE-LO can potentially be a viable adhesive for the attachment of a inner support structure to the inner vessel. However, this simplified analysis only considers a cohesive in-plane failure of the adhesive. The adhesive interface strength at cryogenic temperatures should also be considered, but this is beyond the scope of this section. Finally, Figure 2.19 shows a laminate that is free to contract and expand in the out-of-plane direction. In practice, the inner vessel, representing the bottom substrate, and the support structure, represented by the top substrate, would prevent free out-of-plane motion, leading to additional out-of-plane stresses in the adhesive.

2.5.2. Key Performance Metric: Gravimetric Efficiency

A key performance metric in hydrogen storage is the gravimetric efficiency, which measures how efficiently the vessel stores hydrogen. This is calculated as:

$$\eta_{grav} = \frac{m_{LH2}}{m_{LH2} + m_{ss}} \tag{2.20}$$

where:

- m_{LH2} = Mass of LH2 [kg]
- m_{ss} = Mass of the storage system [kg]

Typically, the calculation of gravimetric efficiency for an LH2 storage system focuses on the storage tank or vessel itself, including its insulation, structural supports, and any components directly integral to storing the hydrogen. However, whether to include piping and other auxiliary components, such as valves, sensors, and piping, depends on the scope of the analysis.

For reference, in Tzoumakis et al.'s study on an aluminum 2219 liquid hydrogen aircraft tank, only the tank structure itself was considered, excluding piping and peripheral equipment. Their optimization resulted in a gravimetric efficiency of 41% [51].

2.6. Literature Study Conclusions

This chapter has investigated the most important concepts in developing double-walled vessel technology for liquid hydrogen (LH2) storage in aircraft.

Initially, suitable analytical stress analysis methods for sizing thin or thick-walled composite pressure vessels were explored to ensure structural integrity under operational conditions. Following this, the vessel's free expansion when subjected to pressure and temperature variations was examined, highlighting its importance for designing support structures capable of withstanding these dynamic changes.

The effects of cryogenic temperatures on key material properties of composites were then considered, emphasizing the necessity of selecting materials that maintain their performance under extreme conditions. Thermodynamic considerations were explored, concluding that minimizing heat leakage is vital to prevent excessive boil-off of stored hydrogen.

This investigation naturally led to an analysis of the main heat transfer mechanisms, including radiation, general conduction, and gas conduction, and how these can be mitigated to optimize thermal insulation. Special attention was given to hydrogen permeation in the vacuum space, recognizing its significant potential to increase gas conduction, which poses a major challenge in maintaining the vacuum's insulating properties.

A significant portion of the literature review focused on the inner support structure, an essential part of double-walled vessel technology that requires careful consideration due to its impact on the vessel's

overall performance. While some ideas were found in academic literature and industrial applications, much of the research is limited in scope. For example, while support structure designs are available for long-haul trucks or stationary Dewars, there is a noticeable lack of designs suited for small aircraft, such as those used in AeroDelft's application. Additionally, companies that may have working solutions often keep their design details vague for proprietary reasons. As a result, despite the importance of internal support structures, existing literature provides limited detailed designs and analyses, underscoring a clear gap in current research.

Therefore, this thesis aims to address the lack of inner support structure concepts by investigating and developing innovative designs tailored specifically for advanced storage vessels in small aircraft applications.

2.7. Research Question and Sub-Questions

The following research and sub-questions form the basis of the project's scope:

Research question

What design methodology would facilitate the development of effective inner support structures for a double-walled vessel used in a small liquid hydrogen-powered aircraft?

Sub-questions

1. What are the critical design and performance requirements that need to be defined and satisfied for the internal support structure?
2. What are suitable analytical and numeral methods used to evaluate and verify the performance and behaviour of the internal support structure?
3. How does the choice of material for the inner and outer vessel impact the design and attachment methods of the internal support structure?

3

Methodology & Requirements

3.1. Methodology

Figure 3.1 outlines the methodology used for developing inner support structure concepts. The process followed was similar to a typical engineering design process, as described by Haik and Shanin [56]. Each step of the process is described in more detail below.

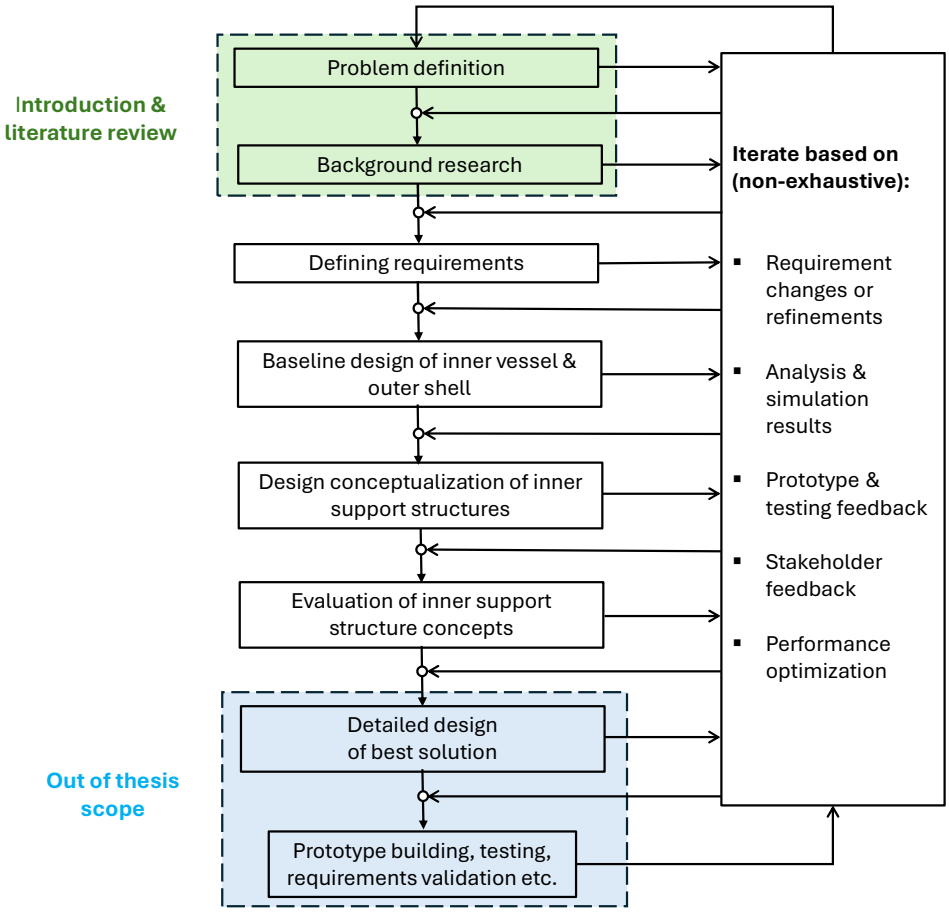

Figure 3.1: Methodology for the development of inner support structure concepts

Problem definition and background research

The engineering design process begins by clearly defining the problem, identifying the need, and understanding how it affects the broader system. Background research follows as a critical step to gather insights from previous experiences and existing solutions. This research helps avoid past mistakes and lays the groundwork for innovative approaches. As seen in the literature review, various existing inner support structure solutions were examined, even if they did not fully align with the specific design case. It is therefore possible to build up from this existing framework.

Defining requirements

Requirements establish the criteria that a given design must meet and guide the subsequent design and development phases. These include functional requirements, operational requirements, and constraint requirements. As will be shown, requirements are defined not only for the inner support structure but also for the inner vessel and outer shell used in the baseline design described in the next step. While the requirements are not exhaustive, they provide a suitable framework for the thesis scope.

Baseline design of inner vessel and outer shell

Chapter 4 is dedicated to the baseline design of the inner vessel and outer shell. Although the primary focus of the project is the development of the inner support structures, it is crucial to establish baseline designs for these components. This is because the behavior of the inner vessel and outer shell directly influences the design and performance of the inner support structure. For instance, an inner vessel made from aluminum will exhibit different thermal expansion properties compared to one made from carbon composites. Attachment methods such as welding, fastening, or bonding also depend on the material choice. Therefore, it is essential not to treat these components as black boxes.

Design conceptualization of inner support structures

In the next step of the methodology, the focus is on designing inner support structures, which are explained in detail in Chapter 5. Four designs are presented with sufficient details for analysis. Each concept is discussed to illustrate why it could be a viable solution and worth analyzing. These designs draw inspiration from solutions used in space structures, and/or build upon existing solutions.

Evaluation of inner support structure concepts

The next step in the methodology involves evaluating the inner support structure concepts. Initially, each design will undergo analysis for modal, thermo-mechanical, crash loads, and heat leakage. These preliminary analyses aim to demonstrate that the proposed concepts are viable by meeting the basic functional requirements. Following this, the designs will be evaluated based on performance criteria, including gravimetric efficiency, heat leakage prevention, safety, and feasibility of manufacturing and assembly, to determine the “best” design(s).

Out of scope

Detailed designs and analysis followed by prototype building and testing stages of the design methodology are considered out of scope for this thesis. The primary focus of this project is to establish a methodology for designing the support structure of a double-walled composite vessel, defining the requirements, and providing some preliminary designs and analysis based on this methodology. Given that this is a preliminary phase of the design cycle, detailed analysis and prototyping are beyond the scope of this work.

Iterations

Figure 3.1 illustrates the potential for iteration at every step of the engineering design process. The right-hand box lists several reasons for iteration. For example, during the Design conceptualization and evaluation steps, iterations might occur to ensure all designs are on relatively equal footing for assessment. Even small design changes can be the difference between a viable and an unviable solution. Requirement changes, like a new limit on allowable heat leakage, can prompt iterations.

3.2. Defining Requirements

Tables 3.1 and 3.2 contain the list of requirements for the project. Since the project's main focus is on developing inner support structures, Table 3.1 exclusively covers this component.

Table 3.1: List of requirements for the inner support structure

ID	Type	Description	Rationale
REQ-01	Func.	The inner support structure **SHALL** support the weight of the inner vessel and its contents during all operating conditions.	To ensure the correct functionality of a double-walled vessel, the inner vessel must be adequately supported within the vacuum space.
REQ-02	Func.	The inner support structure **SHALL** limit thermo-mechanical stresses by accommodating thermal expansion and contraction of the inner vessel.	Over-constraining the inner vessel may result in damage to surrounding components as it cools from room temperature to cryogenic temperatures.
REQ-03	Op.	The inner support structure **SHOULD** limit the heat transfer to the inner vessel to 1 Watt.	Excessive conductive heat leakage can lead to temperature fluctuations within the inner vessel, causing undesirable pressure variations leading to hydrogen venting.
REQ-04	Op.	The inner support structure **SHALL** be designed such that the fundamental frequency of the complete vessel exceeds 10 Hz when the inner vessel is filled with liquid hydrogen.	To ensure that the vessel resonant frequency is higher than the typical driving frequencies encountered in a plane.
REQ-05	Func.	The inner support structure material **SHALL** maintain adequate mechanical properties, including strength, stiffness, and toughness at cryogenic temperatures.	Ensuring the inner support structure maintains structural integrity and safety under extreme cold conditions enhances operational reliability and safety in cryogenic applications.
REQ-06	Func.	The support structure **SHOULD** require minimal maintenance and allow for ease of inspection and replacement of parts.	Minimal maintenance reduces downtime and operational costs, while easy inspection and replacement enhance the reliability and longevity of the system by facilitating prompt detection and resolution of potential issues.
REQ-07	Func.	Inner support structure materials **SHALL** minimize outgassing in accordance with the ASTM E595 standard.	Outgassing of materials releases substances in gaseous form. This is common for polymer-based materials. Consequences can include (1) degradation of material properties, (2) condensation on thermal coatings can change the rate at which the coatings absorb or transmit heat, (3) vacuum space is compromised leading to higher heat transfer.

Table 3.2 contains the requirements for the inner vessel, outer shell, and the overall structure. A note on the nomenclature: Functional requirements describe what must be achieved, Operational requirements specify how well it must be performed, and Constraint requirements define the limitations on available resources, schedule, or physical characteristics [38]. According to NASA's Systems Engineering Handbook, "SHALL" denotes a requirement, "SHOULD" indicates a goal, and "WILL" represents facts or declarations of purpose [57].

Table 3.2: List of requirements for inner vessel, outer shell, or complete structure

ID	Type	Description	Rationale
REQ-08	Op.	The inner vessel **SHALL** be designed with the following: **Operating Temperature** = 20K **Operating Pressure** = 1-5 Bar **Venting Pressure** = 6.5 Bar **Burst Pressure** = 10 Bar	Operating temperatures, operating pressures, and venting pressures based on AeroDelft requirement. Burst pressure of twice the operating pressure is deemed appropriate.
REQ-09	Op.	The complete vessel, with nominal operating temperatures and pressures, **SHALL** withstand, without structural degradation, the following ultimate load factors. These load factors are to be applied separately: **Sideward** n = 1.5 G **Forward** n = 9.0 G **Downward** n = 6.0 G	In accordance with 14 CFR 23.561 (General) for normal, utility, and commuter airplanes, the structure must be designed to give each occupant every reasonable chance of escaping injury when the provided load factors are experienced by the occupant(s). Hence, the vessel should be designed such that the prescribed loads do not cause structural degradation.
REQ-10	Op.	The inner vessel, inner support structure, and outer vessel, **SHALL** withstand at least 100 thermal cycles between room temperature and 20K without any structural degradation.	Based on AeroDelft's requirements for an average of three usages per month for three years. Thermal cycling between room temperature and 20K can induce stress on the inner vessel, the inner support structure, and outer vessel due to extreme temperature differences.
REQ-11	Op.	The vacuum **SHALL** maintain its integrity for a minimum of 15 cycles before requiring re-evacuation	AeroDelft requirement.
REQ-12	Op.	There **SHALL** be no venting of hydrogen for at least 1 hour after refueling.	One hour after refueling is deemed appropriate by AeroDelft to prevent hydrogen venting around engineers between the completion of refueling and the start of the aircraft.
REQ-13	Cons.	The inner tank **SHALL** have a volume of 91L.	AeroDelft's requirement, based on required amount of LH2 and allowances.
REQ-14	Cons.	Minimum stored hydrogen **SHALL** be 5kg, corresponding to an initial fill rate of approximately 80 percent of the inner vessel volume.	Based on AeroDelft's mission profile.
REQ-15	Func.	The outer vessel **SHALL** resist buckling under the negative pressure of the vacuum.	To prevent any compromise to the outer shell's ability to safely contain and manage a vacuum.
REQ-16	Cons.	The complete vessel **SHALL** remain within a 500mm x 500 mm x 900 mm design volume.	Based on AeroDelft's design volume which is mainly determined by the allowed entry space when the canopy is open.

4

Baseline Design of Inner Vessel & Outer Shell

With the requirements now defined, this next chapter focuses on advancing to the subsequent step of the engineering design process, as outlined in Figure 3.1. This chapter is dedicated to developing the baseline design for the inner vessel and outer shell. Since the inner support structure interfaces with these components, having a realistic design as a starting point is crucial for developing and analysing the support concepts.

This chapter begins by proposing suitable materials for both the inner vessel and the outer shell. It then proceeds to calculate the required thickness for these components. Following this, the baseline dimensions and approximate weights of the vessels are presented. Additionally, the chapter includes a heat transfer analysis that encompasses radiation and gas conduction driven by permeation, which is particularly relevant if a composite inner vessel is considered. Finally, pressure rise plots show the time before venting, while omitting the inner support structure for now.

4.1. Material Properties

The suggested material for the construction of the inner composite pressure vessel is APC-2 PEEK (thermoplastic) reinforced with AS4 fibers. Ahlborn [58] demonstrated that AS4-PEEK samples, with a $[0/90]_{4s}$ cross-ply layup, remained free of micro-cracking even after undergoing 120 cryogenic cycles. This result was based on thermal cycling of samples between room temperature and 77K. Ahlborn attributed this durability to the superior interfacial strength of AS4-PEEK.

In a separate series of tests, Ahlborn subjected AS4-PEEK $[0/90]_{4s}$ samples to tension-tension fatigue loading (R=0.1) at cryogenic temperatures of both 77K and 5K. Micro-cracks formed upon the first load cycle at both temperatures. But crack density remained nearly constant throughout additional cycles and increased progressively just before final fracture. The study did not clarify whether these initial micro-cracks were interconnected. The endurance limit for AS4-PEEK $[0/90]_{4s}$ at both 77K and 5K was found to be 53% of the ultimate tensile strength of the laminate. Notably, no significant difference was observed in the endurance curves between the two test temperatures.

However, there are limitations to applying these findings directly to the design of the baseline inner vessel. The stress state in the thin-walled vessel is bi-axial (hoop and longitudinal) rather than purely

tensile. Additionally, the composite layup used in the vessel design is expected to differ from the cross-ply configuration studied. Despite these differences, Ahlborn's research provides valuable insights for certain safety and design considerations when constructing a vessel subjected to cryogenic and pressure cycles.

In addition to this study, Funk and Sykes recommended AS4-PEEK for cryogenic aerospace applications due to its superior resistance to micro-cracking after cryogenic cycling [59]. Carbon fiber-PEEK, which is compatible with the automated tape placement (ATP) manufacturing process, has also been identified as a promising material for cryogenic storage tanks because of its high specific strength, toughness, and chemical resistance [20]. Additionally, Flanagan et al. concluded that the permeability of *undamaged* carbon fiber reinforced PEEK is sufficiently low, making it a suitable material for cryogenic storage [20].

Table 4.1 summarizes the properties used for the analysis of the baseline designs. The stiffness and coefficient of thermal expansion (CTE) values for AS4-PEEK at room temperature are referenced from Sun et al.'s paper [60], while the strength values are sourced from Tan et al.'s research [61]. Values for thermoplastic T300/N5208 [62] unidirectional lamina are provided as well. Lastly, aluminum is included as a reference material for comparison purposes [12].

Table 4.1: Room temperature properties of AS4-PEEK, T300/N5208, and a typical Aluminum

Property	**AS4-PEEK**	**T300/N5208**	**Aluminum**
Long. modulus, E_1	127.6 GPa	181.0 GPa	72.4 GPa
Trans. modulus, E_2	10.3 GPa	10.3 GPa	72.4 GPa
Shear modulus, G_{12}	6.0 GPa	7.17 GPa	27.8 GPa
Major Poisson ratio, ν_{12}	0.32	0.28	0.3
Long. CTE, α_1	0.63E$-$6/°C	0.02E$^-$6/°C	22.5E$^-$6/°C
Trans. CTE, α_2	29E$^-$6/°C	22.5E$^-$6/°C	22.5E$^-$6/°C
Long. tensile strength, X^T	2463 MPa	1500 MPa	-
Long. compressive strength, X^C	1493 MPa	1500 MPa	-
Trans. tensile strength, Y^T	102 MPa	40 MPa	-
Trans. compressive strength, Y^C	254 MPa	146 MPa	-
In-plane shear strength, S	80.81 MPa	68 MPa	-
Post-weld yield strength	-	-	172 MPa
Ply thickness (assumed), t_{ply}	0.125 mm	0.125 mm	-
Density, ρ	1.46 g/cm^3	1.6 g/cm^3	2.7 g/cm^3

4.2. Cryogenic Thermal Stress Implications for the Inner Vessel

Finding a preliminary baseline design for the inner vessel using composites becomes complex when considering the significant temperature drop caused by LH2. A uniform temperature change induces thermal stresses throughout the laminate due to the differing CTEs of each layer, potentially leading to matrix failure. For instance, a $[0/90]_s$ layup with AS4-PEEK properties from Table 4.1, subjected to a uniform temperature change from 20°C to -253°C, will generate a tensile stress of 70 MPa in the matrix. This implies that, with a $[0/90]_s$ layup, the material is already loaded to nearly 70% of its matrix strength, even before any internal pressure is applied. Using the thermoplastic T300/N5208, which has a matrix tensile strength of 40 MPa, would mean that the allowable stress in this direction is already exceeded.

Therefore, it is evident that composites with relatively high tensile matrix strengths should be prioritized for vessels subjected to cryogenic temperatures.

Table 4.2: Tensile stress in AS4-PEEK matrix caused by uniform temperature drop of -270 °C for different layups

Layup	Max tensile stress in matrix (MPa)
$[0/90]_s$	70
$[\pm 25]_s$	34
$[\pm 45]_s$	70
$[\pm 55]_s$	58
$[\pm 65]_s$	34
$[0/0]_s$	0
$[90/90]_s$	0
$[0/45/-45/90]_s$	70
Aluminum (for reference)	0

Table 4.2 presents the maximum tensile stress in the matrix for various AS4-PEEK composite layups subjected to a temperature change of $\Delta T = -270°$C. It can be observed that the matrix tensile stress is directly influenced by the stiffness and CTE characteristics of the adjacent plies, which result from their relative fibre orientations. Layups such as $[0/90]_s$ and $[\pm 45]_s$, where successive fibre angles differ by 90°, experience the highest matrix tensile stresses. In contrast, layups like $[\pm 25]_s$ and $[\pm 65]_s$ exhibit reduced matrix tensile stress due to the smaller difference in fibre angles between layers. To entirely prevent thermal stress within the laminate, the layers would need to be oriented solely at 90° or 0°.

4.2.1. Impact of Vessel Diameter on Weight Savings and Material Choice

When temperature loading is neglected, analyses indicate that the optimal winding layup for achieving the lightest vessel construction is $[\pm 55]_{ns}$ [11]. According to Table 4.2, this orientation results in a matrix tensile stress of 58 MPa under a uniform temperature change of $\Delta T = -270°$C. A noteworthy observation is that this thermal stress state will be consistent across all vessel diameters.

Figure 4.1 compares the mass per unit area of a composite (AS4-PEEK) inner vessel versus an aluminum inner vessel under a $\Delta T = -270°$C thermal load and an internal pressure of 10 bar (twice the operational pressure). For aluminum, the minimum required thickness to prevent yielding, based on a post-weld yield strength of 172 MPa and using the Von-Mises failure criteria, is indicated next to the blue tick marks. For the composite, the Tsai-Wu failure criterion is applied, with first-ply-failure being considered. The required $[\pm 55]_{ns}$ layup is shown next to the black tick marks. To simplify the analysis, only the stress in the cylindrical section of the vessel is considered, away from the the domes.

The initial thermal stress state on the composite inner vessel necessitates a thicker layup to adequately withstand the subsequent internal pressure. However, this initial thermal “handicap” remains consistent across all vessel diameters. As the vessel diameter increases, the mass of the aluminum vessel grows more rapidly compared to the composite vessel. For instance, certain composite layups, such as $[\pm 55]_{3s}$, can be effectively used for both 0.6m and 0.8m diameter vessels, whereas aluminum requires a consistent increase in its thickness.

Thus, the graph demonstrates that potential weight savings with composite materials increase with vessel diameter. This is particularly relevant for applications such as those by AeroDelft, which require relatively small vessel sizes (e.g., less than 0.5m in diameter). Unless the vessel length is significantly long, it is worth questioning whether a reduction of 0.5 kg to 1 kg justifies the added complexity and cost associated with the analysis and manufacturing of composite LH2 vessels.

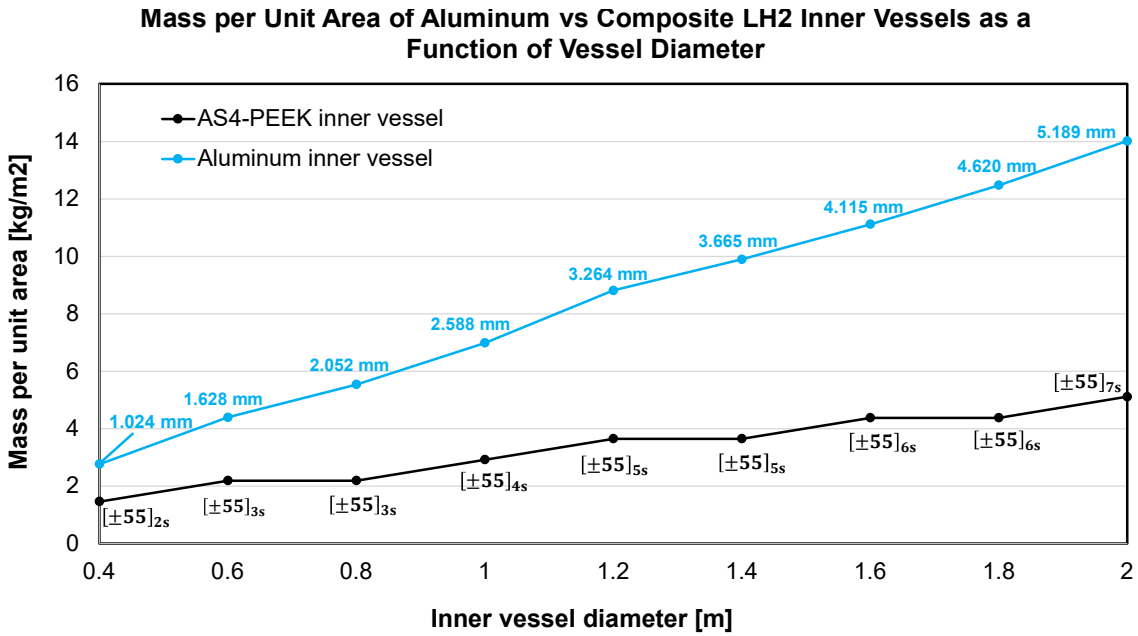

Figure 4.1: Mass per unit area of aluminum vs. composite LH2 inner vessels for varying diameters subjected to a uniform $\Delta T = -270°$C and 10 bar of internal pressure

Worth noting is that the temperature drop across the vessel is not uniform as what is assumed in this thesis. The wetted inner surface experiences cryogenic temperatures before the outer surface, and the bottom of the vessel will reach cryogenic temperatures well before the rest of the vessel. Consequently, the entire vessel will only reach the the same temperature after some time. This non-uniform temperature distribution results in a more complex stress state during the refueling period compared to a uniform temperature drop. This aspect should be considered in more detailed analyses.

4.3. Dimensions and Mass of Baseline Design

The overall dimensions of the baseline design are shown in Figure 4.2. Tables 4.3 and 4.4 list the thickness of the inner vessel and outer shell for both materials, including the chosen composite layup.

If considering only a uniform temperature loading of $\Delta T = -270°$C and an internal pressure of 10 Bar (twice the expected operating pressure), an 8-layer layup of $[90/(\pm 55)/90]_s$ for AS4-PEEK and a 1.024 mm (18 Gauge) aluminum thickness would be sufficient for the composite and aluminum inner vessels, respectively. However, the inner vessels were intentionally designed with the specifications listed in Table 4.3 to account for potential additional stresses from external loading. This approach was primarily taken to avoid resizing the inner vessels during the analyses of Chapter 7. Additionally, for the composite inner vessel, extra ± 55 layers were included to lower the stress magnitude from the internal pressure for fatigue concerns, in line with the discussion of Section 4.1.

Table 4.3: Thickness and approximate mass for the Inner vessel

Inner vessel (inputs: 20°C to -250°C & 10 Bar internal pressure)			
Material	**Thickness (oversized) [mm]**	**Density [g/cm^3]**	**Approx. mass [kg]**
AS4-PEEK $[90/(\pm 55)_3/90]_s$	2	1.46	3.2
Aluminum	1.290 (Gauge 16)	2.7	3.6

The design of the outer shell was determined by considering an external pressure of 1.25 atm, incorporating a safety factor of 1.25. The required thicknesses to prevent shell buckling for a quasi-isotropic layup using T300/N5208 and aluminum are listed in Table 4.4.

Table 4.4: Thickness and approximate mass for the outer vessel

Outer vessel (input: 1.25 atm external pressure)			
Material	**Thickness [mm]**	**Density [g/cm^3]**	**Approx. mass [kg]**
T300/N5208 $[0/\pm 45/90]_{2s}$	2	1.6	4.8
Aluminum	Gauge 12 (2.057 mm)	2.7	8.4

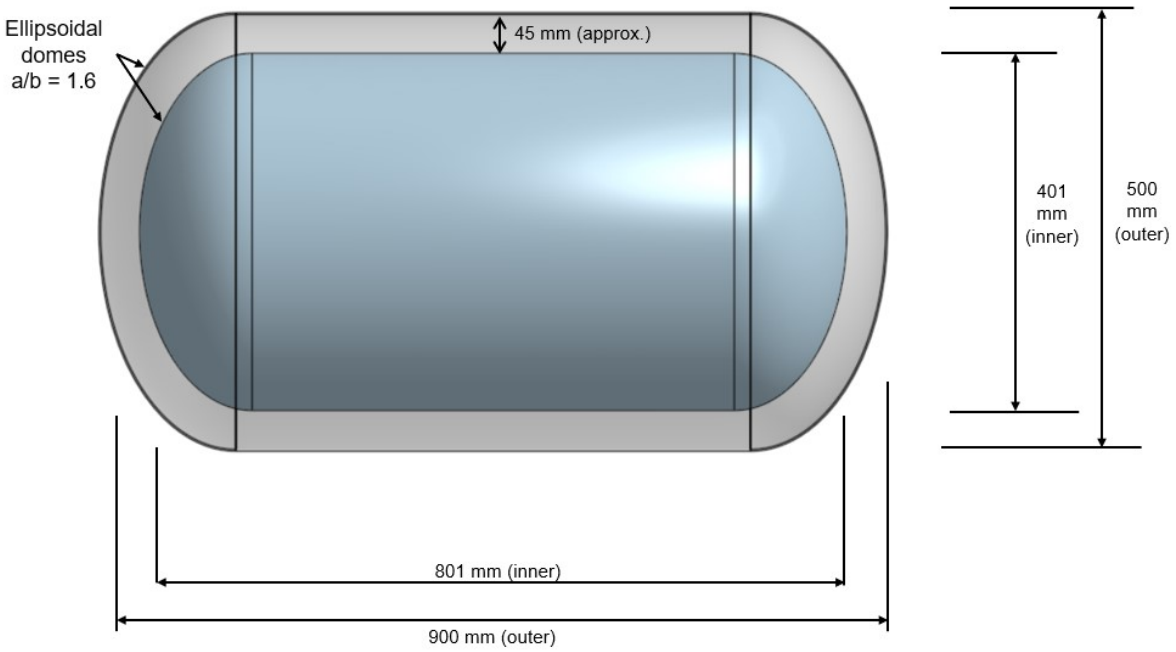

Figure 4.2: Overall dimensions of baseline design without any inner support structure

The dome shapes shown in Figure 4.2 are based on Brewer's findings [63], which indicate that elliptical domes with an a semi major axis to semi minor axis ratio (a/b) of 1.6 offer the optimal balance for minimizing both weight and vessel length.

The composite layups presented in Tables 4.3 and 4.4 are not optimized but serve as baseline designs to initiate the project. While optimization to achieve the lightest construction is recommended, it lies beyond the current project scope.

4.4. Heat Transfer & Boil-Off of Baseline Design

The following section goes into calculated the radiative heat transfer, permeation driven gas conduction, and time-to-boil off for the baseline design.

4.4.1. Radiative Heat Transfer of Baseline Design

Section 2.3.1 discussed the use of multilayer insulation (MLI) on the inner vessel to reduce heat transfer via radiation. MLI consists of multiple layers of reflective, low-emittance films [34]. Solid conduction is minimized by incorporating low-conductivity spacers between the layers, while gas conduction is minimized by maintaining a vacuum, as is the case in the current design.

The equation for the effective emissivity, ϵ^*, for highly evacuated systems (gas pressures of $10 \mu m Hg$ or less) and non-contacting layers is defined as [34]:

$$\epsilon^* = \frac{1}{\frac{1}{\epsilon_{in}} + \frac{1}{\epsilon_{out}} - 1} \left(\frac{1}{N+1} \right) \tag{4.1}$$

where,

- ϵ_{in} = Emissivity of the inside surface of the layer.
- ϵ_{out} = Emissivity of the outside surface of the layer.
- N = Number of layers.

The presence of air molecules or the permeation of hydrogen into the vacuum, leading to a gas pressure greater than 10μmHg, will increase the effective emissivity of the MLI. However, investigating this effect on the performance of the MLI is beyond the scope of this section.

Table 4.5 describes the properties of the MLI chosen. Aluminized Mylar, a simple and common form of MLI material, was chosen for the baseline design. The data is from a spacecraft thermal control design handbook [34].

Table 4.5: Characteristics of Double Aluminized Mylar MLI [34]

Characteristic	**Value**
Inside emissivity, ϵ_{in}	0.03
Outside emissivity, ϵ_{out}	0.05
Mass of single layer (g/cm^2)	0.00093
Thickness of single layer (mm)	0.0064
Temperature range (°C)	-250 to 150
Layer Count (N)	5
Effective emissivity, ϵ^*	0.0032
Surface area of inner tank (cm^2)	$\approx$ 10782
Mass of MLI (kg)	$\approx$ 0.1

The heat transfer by radiation from the outer shell (surface 2) to the inner vessel (surface 1) is given by Equation 2.12. Namely:

$$Q_{21} = -\left(\epsilon_1 \cdot A_1 \cdot B_{12} \cdot \sigma \cdot (T_1^4 - T_2^4)\right) \approx \textbf{1.5W} \tag{4.2}$$

where,

- $\epsilon_1 = epsilon^*$= 0.0032 (Table 4.5)

- A_1 = Area of surface 1 = 1.0782 [m^2]
- B_{12} = 0.98 (calculated through equation 2.11 with ϵ_2 assumed to be 0.1)
- $\sigma = 5.670 \times 10^{-8}$, Stefan-Boltzmann constant [W/m^2K^4]
- T_1, T_2 = 20K & 293K, respectively [K]

4.4.2. Permeation of Hydrogen and Gas Conduction

In Section 2.1.3, it was mentioned that Flanagan et al. investigated the permeability of carbon fiber PEEK composites for cryogenic tanks [20]. The study demonstrates that the leak rate (Scc/sm^2) is proportional to the pressure difference and inversely proportional to the material thickness. As seen from table 2.1, Flanagan et al. presented a single data point for the leak rate of un-cycled AS4-PEEK at 77K. This value is used to provide an approximate estimate of the magnitude of permeation entering the vacuum space and the resulting gas conduction. However, it should be noted that additional test data is needed, such as measuring the leak rate at 20K after subjecting the material to multiple cryogenic and load cycles, to better reflect its intended application.

The following calculation is used to find the number of moles of hydrogen entering the vacuum space and the resulting pressure assuming an ideal gas law behaviour.

$$n = \frac{\left(LR_{ref} \times \frac{\Delta P_{actual}}{\Delta P_{ref}} \times \frac{t_{ref}}{t_{actual}}\right) \times A \times time}{22414\, Scc/mol} \tag{4.3}$$

$$P_{vac} = \frac{nRT}{V_{vac}} \tag{4.4}$$

where,

- n = moles of hydrogen in vacuum space
- LR_{ref} = reference leak rate [Scc/sm^2]
- LR = leak rate [Scc/sm^2]
- $\frac{\Delta P_{actual}}{\Delta P_{ref}}$ = Pressure correction
- $\frac{t_{ref}}{t_{actual}}$ = Thickness correction
- A = Surface area of inner vessel [m^2]
- $time$ = elapsed time [s]
- $1Scc/s$ = $\frac{1}{22414}\, mol/s$ [1]
- P_{vac}= Pressure in vacuum space [Pa]
- R = 8.314, ideal gas constant [J/mol·K]
- T = Temperature of gas in vacuum [K]
- V_{vac} = Volume of vacuum space [m^3]

Table 4.6 lists the inputs used in equations 4.3 and 4.4 to estimate the pressure in the vacuum space after 5 hours, due to hydrogen permeation. The 5 hour period includes 1 hour for refueling/preparation and 4 hours of usage.

[1] https://www.nist.gov/pml/sensor-science/thermodynamic-metrology/unit-conversions

Inputs		
Material	AS4-PEEK	
$\frac{\Delta P_{\text{actual}}}{\Delta P_{\text{ref}}}$	= 5 bar / 1 bar	
$\frac{t_{\text{ref}}}{t_{\text{actual}}}$	= 1.1 mm / 2 mm	
A	$\approx$ 1.078 m^2	
Temperature of gas in vacuum	300 K (assumed)	
Time	18000 s (5 hours)	
V_{vac}	$\approx$ 0.065 m^3	
Initial vacuum pressure	0 Pa (assumed)	
Condition	**Leak rate [Scc/sm^2]**	**P$_{\text{vac}}$ after 5 hours [Pa]**
Un-cycled (tested at 77K)	6.5×10^{-7} [20]	0.0785

Table 4.6: Leak rates and resulting vacuum pressure for AS4-PEEK under specified conditions.

At this pressure, the mean-free-path, λ, of hydrogen within this vacuum space, as calculated from Equation 2.13, is 142 mm. Since λ is considerably larger than the vacuum space shown from Figure 4.2, free molecular conduction predominates. Using Equation 2.16, the molecular state heat transfer for a composite AS4-PEEK vessel after 5 hours worth of permeation is $\approx$ **35W.** This implies that permeation-driven gas conduction will significantly affect heat transfer, even over relatively short periods. This effect worsens considerably if the diffusion mechanism is governed by transport through interconnected micro-cracks as opposed to diffusion (Figure 2.5). The observed large value for gas conduction at such a minuscule pressure aligns with Corrucini's discussion that Dewars typically exhibit "several-fold smaller" heat leakage when containing liquid helium compared to liquid hydrogen. This difference is attributed to the presence of hydrogen in the vacuum space [36].

The observation above brings to light AeroDelft's operational requirement REQ-11, which mandates that the vacuum SHALL maintain its integrity for a minimum of 15 cycles before re-evacuation is required. The gas conduction observed in a liner-less AS4-PEEK design indicates that a vacuum would need to be pulled after each use.

Using a liner as an additional barrier is likely necessary for a composite inner vessel. Alternatives include employing an active vacuum system to continuously remove permeated gases, though this significantly increases weight, or applying barrier coatings to enhance the composite's impermeability. Further investigation into these options is beyond the scope of the baseline design. Additionally, metals exhibit permeation values that are 2–3 orders of magnitude lower than those of composites [19], which is why the exercise was not performed for an aluminum vessel.

4.4.3. Time-to-Vent of Baseline Design (Neglecting Inner Support Structure)

The pressure rise over time for the baseline design, excluding the contribution of the inner support structure, was calculated using the homogeneous model presented in Section 2.2.2. It was noted that the homogeneous model underestimates the actual pressure rise as it does not account for thermal stratification. Therefore, a "stratification factor" of 2 was applied, which doubles the pressure rate at every solution increment. A value of 2 was used by Lin et al. [27], in Verstrate's work [26], and by Onorato [28].

Figure 4.3 illustrates the pressure increase over time for various vessel conditions. As calculated in section 4.4.1, the tank's radiation was determined to be 1.5W. In Section 4.4.2, it was found that hydrogen diffusion through the composite caused a gas conduction heat load that reached approximately 35W at the 5-hour mark. The graph illustrates two main scenarios: one where this gas conduction leads to a significant source of heat transfer, resulting in a faster time-to-vent, and another where an ideal (or nearly ideal) vacuum prevents gas conduction, keeping the heat leak minimal. This comparison emphasizes the importance of effective vacuum management to reduce gas conduction and extend the time-to-vent.

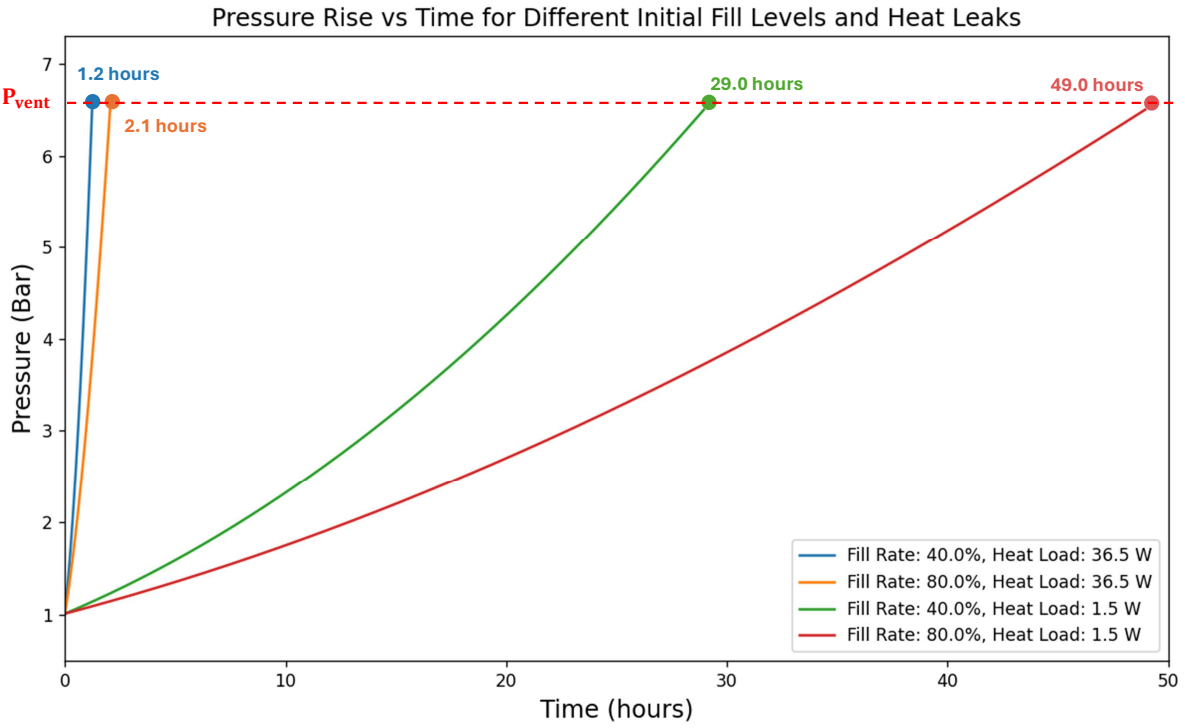

Figure 4.3: Pressure rise vs time for different conditions (P_{vent} = 6.5 bar, Strat. factor = 2, inner vessel volume = 91L), inner support structure omitted

From the plot of Figure 4.3, a couple other observations can be made:

(a) A lower LH2 initial fill rate, which corresponds to a higher proportion of gaseous hydrogen in the vessel, will result in a quicker time-to-vent compared to a higher LH2 initial fill rate. This is because, with a higher initial fill rate, the larger mass of LH2 requires more time to absorb the necessary energy (enthalpy of vaporization) to vaporize.

(b) Evident from the green and red curves in Figure 4.3, the pressure rise over time is non-linear. This behavior is likely due to the fact that as the temperature in the vessel increases, the enthalpy of vaporization decreases, allowing vaporization to occur more rapidly and thus accelerating the pressure rise.

The Python code used to produce Figure 4.3 is listed in Appendix B for reference. Another alternative to the code is making use of the BoilFAST software from the University of Western Australia [64].

5

Internal Support Structure Concepts

This chapter focuses on the conceptual design of inner support structures for double-walled vessels. In formulating these designs, a simple checklist was followed as a basic guideline to ensure that foundational functional requirements were considered and addressed. It is important to note that this checklist does not encompass the more comprehensive requirements outlined in Section 3.2; rather, it was used to ensure that critical aspects were not overlooked. The checklist is as follows:

- ☐ Does the design ensure that the inner vessel is adequately constrained in its six degrees of freedom (DoF)?
- ☐ Does the design allow thermal expansion and contraction of the inner vessel? Alternatively, does the design incorporate features to mitigate excessive thermo-mechanical stresses in the inner vessel, inner support structure, and outer shell?
- ☐ Does the inner support structure incorporate features for thermal isolation, such as materials with low thermal conductivity, designs that extend the thermal path, or minimized contact area between components?
- ☐ Based on simplified calculations, is the support structure deemed capable of withstanding the crash loads when the inner vessel is filled with LH2?

This chapter presents four distinct inner support structure designs, each with an overview, design intent, and key considerations. All designs are presented with equal detail. While the goal at this stage is not to provide detailed designs, including specific dimensions and tolerances, the provided information is sufficient for analysis.

5.1. Design 1 - Discrete Flexures

The first design concept takes inspiration from the flexible structural brackets used in spacecraft satellite systems, as depicted in Figure 2.16.

5.1.1. Overview

This design consists of individual tapered members, called “flexures”, positioned between the inner and outer vessel around the circumference (see Figure 5.1). These members are constructed from a material with a relatively low modulus of elasticity and thermal insulating properties, such as a polymer. To enhance compliance and resistance to heat transfer, triangular cutouts have been incorporated. If a higher fundamental frequency is required, or if the limit loads cannot be adequately supported, additional flexures can be added.

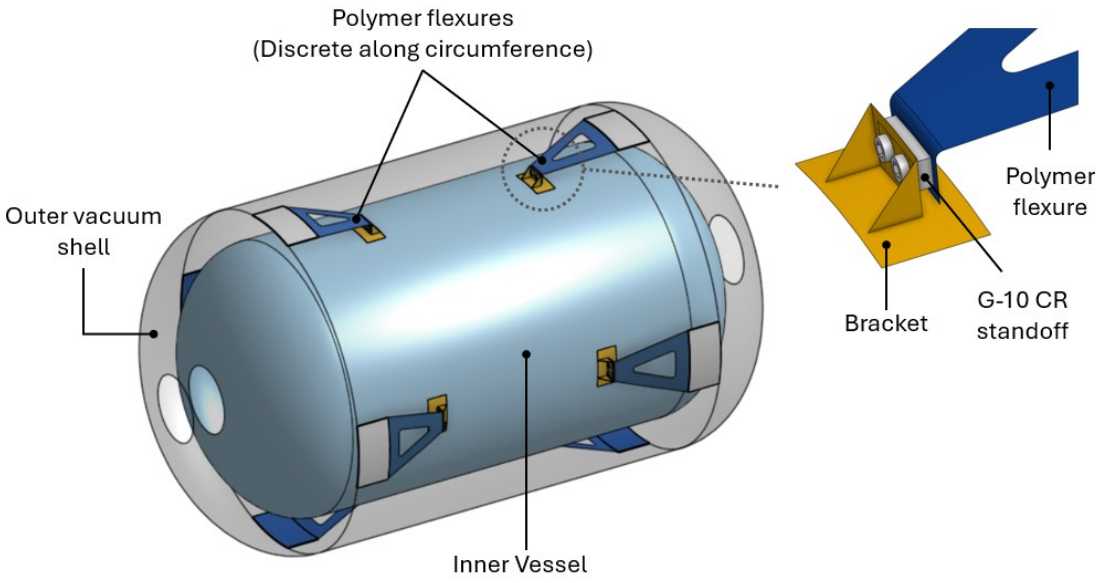

Figure 5.1: Overview of discrete flexure design

5.1.2. Design Intent

The inner vessel is inherently over constrained, but its radial and axial contraction/expansion will be absorbed by the compliant flexures, as depicted by Figure 5.2. Hence, the intent of this design, as is the case for the bracket of 2.16, is to prevent the interfacing components from being significantly stressed from large temperature gradients.

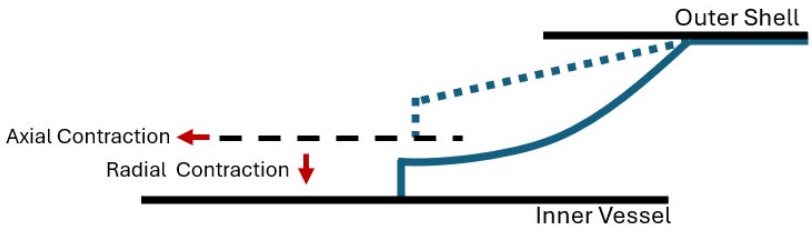

Figure 5.2: Demonstrating the design intent of flexures under an axial and radial contraction

5.1.3. Considerations

Given that the flexures are made from a polymer, the two main considerations are material outgassing and the loss of flexibility at cryogenic temperatures.

Material outgassing

As outlined in the requirements, materials with low outgassing should be prioritized to preserve the integrity of the vacuum. Section 2.3.3 establishes that materials with less than 1% Total Mass Loss (TML) are preferred. Accordingly, Polyethylene (0.58%), PEEK (0.20%), G-10 fiberglass (0.35%), and Teflon (0.01%) are viable options, whereas Nylon (2.38%) is not recommended [65].

Loss of flexibility at cryogenic temperatures

The performance of the design relies on the flexures retaining some form of their elastic properties. However, as is common for polymers subjected to cold or cryogenic temperatures, the material tends to stiffen, increase in strength, but lose ductility. Therefore polymers that have a low glass-transition temperature, such as Teflon (-103 °C [66]), should be considered. Van de Voorde [67] performed extensive testing on various polymers at cryogenic temperatures. Specifically for Teflon, the following was found:

Table 5.1: Mechanical properties of unreinforced Teflon at three different temperatures [67]

Material:	Unreinforced Teflon		
Temperature [K]	**Modulus, E [MPa]**	**Tensile strength [MPa]**	**Elongation at break [%]**
298	-	19.6	480
77	1422.5	42.2	6.5
4.2	2128.8	54.9	3.5

As shown by the elongation at break in Table 5.1, there is a considerable loss of ductility, rendering the proposed idea already questionable. Regardless, it is worth investigating whether the resulting strain from the mechanical loading will exceed the values shown in the table.

To prevent Teflon from reaching excessively low temperatures (down to 20 K), a G-10 CR ($k \approx 0.21$ W/m·K at -250°C [68]) stand-off plate can be placed between the bracket and the flexure. A simplified transient thermal analysis was conducted to estimate the temperature distribution along a typical polymer ($k \approx 0.2$-0.3 W/m·K) flexure. The results after 5 hours are shown in Figure 5.3, indicating that the base of the flexure, near the bracket, exceeds 77 K (-196°C), while the start of the triangular cutout approaches Teflon's glass transition of -103°C.

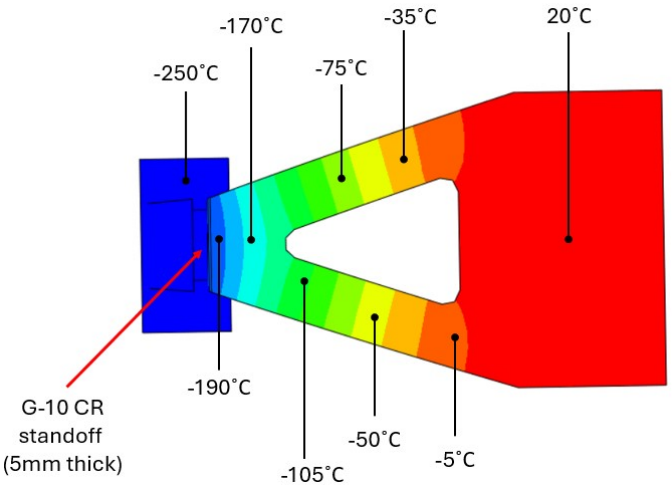

Figure 5.3: Temperature distribution through a flexure after 5 hours (≈ steady-state)

Another design consideration to mitigate the effects of cryogenic temperatures is to size

the flexures based on the dimensions of the inner vessel at cryogenic temperatures. Hence, assembly at room temperature would deform the flexures when they are at their most flexible. Once the inner vessel cools, the initial deflection/stress would be relieved. A potential issue with this approach is that some polymers like Teflon are prone to cold flow, which refers to their tendency to deform gradually under long-term continuous stress, even at temperatures well below their melting point [69]. This design/assembly approach is not investigated in this thesis, but can be an interesting consideration to make the design safer.

5.2. Design 2 - Boss Suspension

In this design, the feasibility of using the bosses of each vessel for suspension, similar to the approach shown in Figure 2.11, is explored.

5.2.1. Overview

As illustrated in Figure 5.4, hollow G-10 CR rods fit within interface flanges (navy blue) and engage axial compression springs. As a result, the outer shell interface flanges push against the outer shell, creating tension, while the inner shell interface flanges apply compression to the inner vessel. The G-10 CR rods are not bonded or fastened to the interface flanges, but a D-bore/shaft feature is used to prevent axial rotation. As may be observed from the image, the dimensions of the vacuum space were adjusted to provide more space for the rod and spring assemblies. Specifically, the radius of the inner vessel was increased, and its length was decreased.

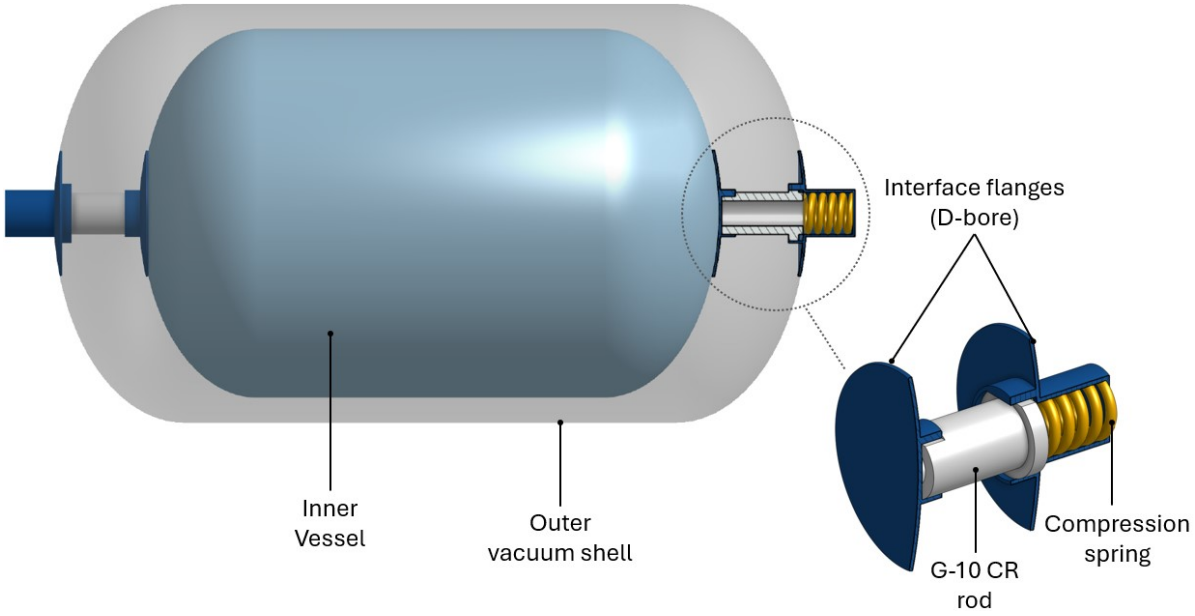

Figure 5.4: Overview of the boss suspension internal support

G-10 CR is a material made of woven fiberglass with an epoxy binder and is often used for cryogenic applications. It has a low thermal conductivity ($k \approx 0.15$ W/m·K at 20K) [68] and maintains exceptional material properties even down to 4K. Kasen et al. conducted a comprehensive study on G-10 CR for temperature ranges between 295K and 4K [70]. As mentioned in section 5.1.3 , G-10 CR has a Total Mass Loss (TML) of 0.35%, making it suitable for use in vacuum spaces [65].

5.2.2. Design Intent

The vessel can contract freely as the compression springs accommodate the movement while continuously applying compression, provided the initial spring deflection is greater than the contraction. An alternative approach would be to have a rigid attachment at one end and a slip joint at the other. However, this solution would likely require a bolted connection or adhesive bond, which is why the use of springs was considered in the first place.

The use of compression springs can be beneficial for a few reasons. Firstly, adequate compression will ensure that the G-10 CR rod counters the bending tensile stress caused by the weight of the inner vessel. Additionally, the springs create tension in the outer shell, which could increase its capacity to resist buckling under the negative vacuum pressure. It should be noted that the impact of this second point may not be very noticeable unless the pre-loads are significantly large.

5.2.3. Considerations

Given the simplicity of this concept, the main considerations at this current stage is the minimum natural frequency from the springs and the possibility of the G-10 CR rod buckling under a compressive loading.

Fundamental frequency

The springs will likely force the system to have its fundamental mode along the axis. If we consider the mass, M, of the inner vessel as being lumped between two springs with spring rates k_s , the frequency can be calculated as $f_n = \frac{1}{2\pi}\sqrt{\frac{2k_s}{M}}$. To ensure that the frequency is above 10 Hz, as per the requirements, a spring rate of approximately 20N/mm would be needed for each spring, assuming a mass total mass of 10Kg.

The springs used in Figure 5.4 have a spring rate of 95 N/m, an outer diameter of 50mm, wire diameter of 8 mm, and 60mm as the free length[1]. Hence, upon assembly, the spring would compress by roughly 10.5mm to produce 1000N worth of preload. With this setup, the fundamental mode would be 22 Hz with an inner vessel and LH2 equal to around 10 Kg.

Buckling of G-10 CR rod

Although likely not an issue for the current application given the low slenderness ratio of the rod, buckling can become an issue when dealing with long and thin-walled rods. In these particular scenarios it could be beneficial to validate that the rods do not buckle under the combination of initial compression and inertial loading. Reed et al. suggested using the following for long, thin-walled, orthotropic cylinders [72]:

$$\sigma_c = \frac{169\sqrt{(E_x/E_y)}}{195 + r/\delta} \cdot \frac{\delta/r}{[3(1-\nu^2)]^{1/2}} \tag{5.1}$$

Where, σ_c is the critical buckling stress, r is the radius, t is the wall thickness, ν is Poisson's ratio, and E_x and E_y are the axial and transverse moduli, respectively.

[1] Catalogue number 3136 from [71]

5.3. Design 3 - Kinematic Mount

The third proposed internal support structure concept design of the internal support structure is inspired by the suspended salt pill described in section 2.4.3.

5.3.1. Overview

Illustrated in Figure 5.5, this system uses Kevlar ropes to suspend the dome sections of the inner vessel from the outer shell. The navy blue adapters at the domes are used to facilitating the connections. Since ropes cannot handle compression, they must be kept under tension. To achieve this, an axial rope at the front end is tensioned, which tension the front ropes. At the back end, three ropes are tensioned individually. The back adapter features three bobbins that wrap the Kevlar ropes, securing the back side of the inner vessel.

Kevlar is proposed specifically because of its high strength and low thermal conductivity ($\approx$ 0.25 W/mK at 20K [47]). Ropes with effective diameters of 3.2mm can meet strength requirements while offering significant resistance to conductive heat transfer. Although Kevlar is mentioned, cryogenic support straps have been made out of carbon, alumina, E-glass, and S-glass [72].

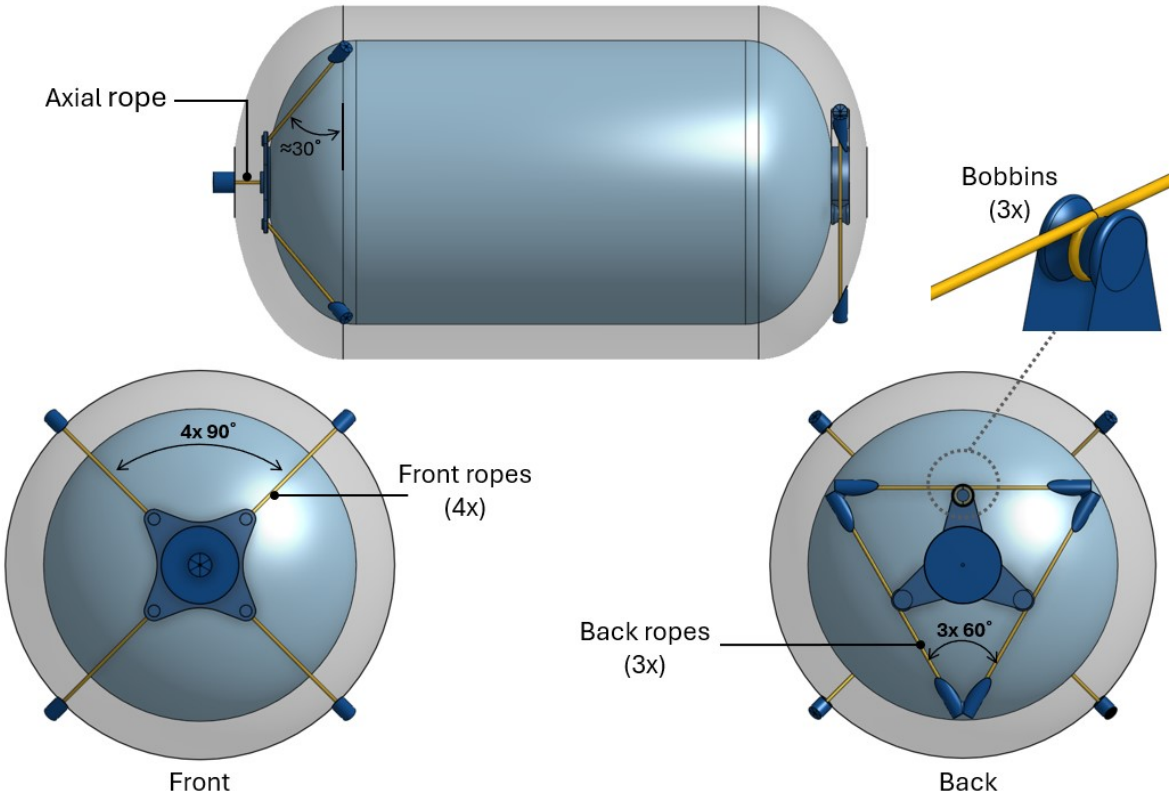

Figure 5.5: Overview of the kinematic mount internal support

5.3.2. Design Intent

Section 2.4.3 defined a kinematic mount as a mount that constrains the six degrees of freedom only once. This concept is illustrated in Figure 5.6 for the inner vessel. At the “front” end, translations Tx, Ty, and Tz are constrained. The “back” end has translations Tx and Ty, as well as rotation about the axis, Rz, constrained. Hence, any axial and radial dimensional changes do not induce stress on the inner vessel. As shown in Figure 5.5, the ropes will simply rotate about their ends to accommodate thermal

movement. This is in line with one of the main functional requirements outlined in Section 3.2, which is to limit the thermo-mechanical stresses caused by large temperature gradients by either incorporating flexibility or allowing for movement.

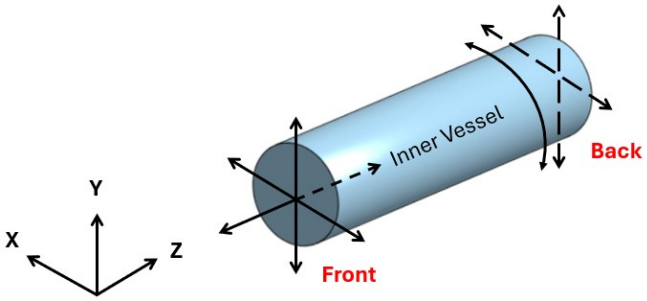

Figure 5.6: Fixed degrees-of-freedom for kinematic mount design

A secondary benefit of the kinematic design is that the ropes themselves do not experience an increase in load, other than the existing preload, when the inner vessel contracts. This is in contrast to Design 1 which relied on the flexures to comply. As a result, the load on the ropes is mostly static for the majority of the life cycle, except for general dynamic motion from the plane.

5.3.3. Considerations

The correct functioning of the inner support structure relies on the ropes having tension. Two Kevlar properties have the capacity of reducing the tension in the ropes and should be considered: coefficient of thermal expansion (CTE) and creep.

Negative CTE

The CTE, α, of Kevlar is negative, meaning that the ropes will expand when cooled by an amount approximately equal to, $\frac{\Delta L}{L} = \alpha \Delta T$. If we assume the CTE of the Kevlar-29 yarn (-4$\times 10^{-6}$/°C at room temperature [44]) is a good enough estimate for a Kevlar-29 braided rope, then the the resulting strain from a ΔT = -273°C will be +0.00192[2]. Therefore, the amount strain from the initial preload on any given rope must be greater than this value, namely,

$$P_{min} = AE\epsilon_T \tag{5.2}$$

where,

- A = Cross-sectional area [mm^2]
- E = 29 $\times$ 10^3, Modulus of braided Kevlar-29 rope, [MPa] (source: [47])
- ϵ_T = Thermal strain

For example, an 3.2mm diameter rope would require a minimum preload of 448N.

Creep

Creep, or time-dependent deformation of a material under constant stress, was quantified for braided Kevlar-29 by Duband et al. [47]. Applying a constant load of 25% of the breaking strength, it was observed that the creep increases logarithmically, about 0.15% elongation per decade. A straightforward solution provided is to re-tighten the rope after it has experienced some creep. Given the logarithmic nature of the creep, any additional strain following the initial creep will be minimal.

[2] Conservative since the entire rope does not have the same ΔT and the CTE magnitude decreases with temperature

With this said, the natural frequency of the design is independent of the preload and relies solely on the stiffness of the ropes, provided the ropes are properly taut. This can be validated by considering a suspended mass, M, between two identical axial ropes with stiffness equal to $k = \frac{EA}{L}$. The natural frequency along the axis will be: $f_n = \frac{1}{2\pi}\sqrt{\frac{2EA}{ML}}$. In other words, the amount of rope preload does not influence the natural frequency only the amplitude of oscillations.

5.4. Design 4 - Zigzagging Ropes

This final concept is heavily inspired by a design proposed by Raymond and Reiter in their paper from the Jet Propulsion Laboratory [43]. While their work provides a solid foundation, it does not delve deeply into aspects such as rope tensioning, natural frequency, and rope integrity. Therefore, the following section builds upon their design by addressing these critical factors and tailoring the solution to meet the specific requirements of this project.

5.4.1. Overview

As illustrated in Figure 5.7 the design features tensioned ropes arranged in a zigzag pattern between the inner vessel and an outer shell. The inner rings interface with the inner vessel without the need for bonding or welding, applying compressive forces when the ropes are tensioned. This configuration provides effective support to the inner vessel in axial, radial, and tangential directions while also ensuring thermal efficiency.

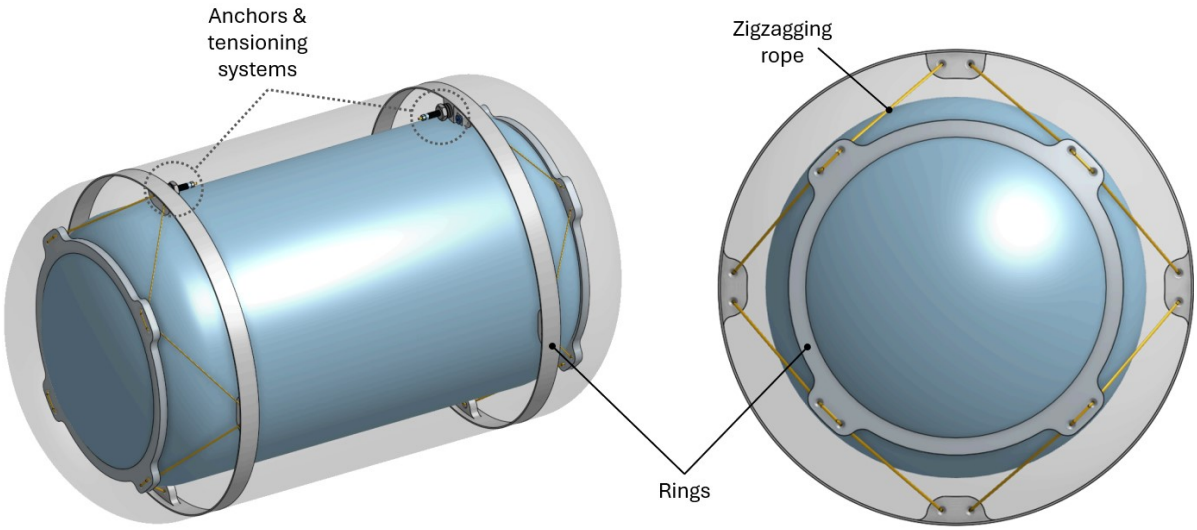

Figure 5.7: Overview of the zigzagging rope internal support

5.4.2. Design Intent

The ropes are inclined out of the radial plane, as can be seen in the left image of Figure 5.7. This design feature allows the ropes to rotate, rather than elongate, in response to the contraction of the inner vessel. Consequently, apart from the initial pretension, thermal cycles will not impose any additional stress on the inner vessel or the ropes.

One of the main advantages of this solution is its improved ergonomics compared to the kinematic mount used in Design 3, which involved significantly more components. The key adjustable parameters in developing this design can include the length and thickness of the ropes, the angles of the zigzag pattern, the number of zigzags around the circumference, and the amount of preload. Therefore, many

different combinations can be explored to meet the needs of different vessel sizes and missions.

5.4.3. Considerations

Rope creep and Kevlar's negative CTE are key considerations for this design. Mitigation strategies for these effects are explored in detail. Additionally, with outer rings included in this concept, the potential to enhance the buckling capacity of the outer shell under external pressure is examined. Methods for calculating the natural frequency based on rope stiffness and orientation are also considered, along with strategies for maintaining rope integrity. Many of these points are equally applicable to the previously discussed kinematic mount concept (design 3).

Slack prevention

As mentioned in section 5.3.3 of the previous design, Kevlar expands when cooled, which can lead to slack and compromise its support capabilities. The rope length, from the initial anchor point to the tensioning system as shown in Figure 5.7, is 2075 mm. Assuming the entire length of the rope undergoes a temperature change (ΔT) of -273°C, the rope will expand by an amount equal to $\Delta L = (2075\text{mm}) \times (-4 \times 10^{-6}\text{mm/mm/°C}) \times (-273\text{°C}) = +2.25\text{mm}$. It should be noted that this is an exceedingly conservative estimate since only the portions of ropes in contact inner vessel rings are subjected to such a large ΔT.

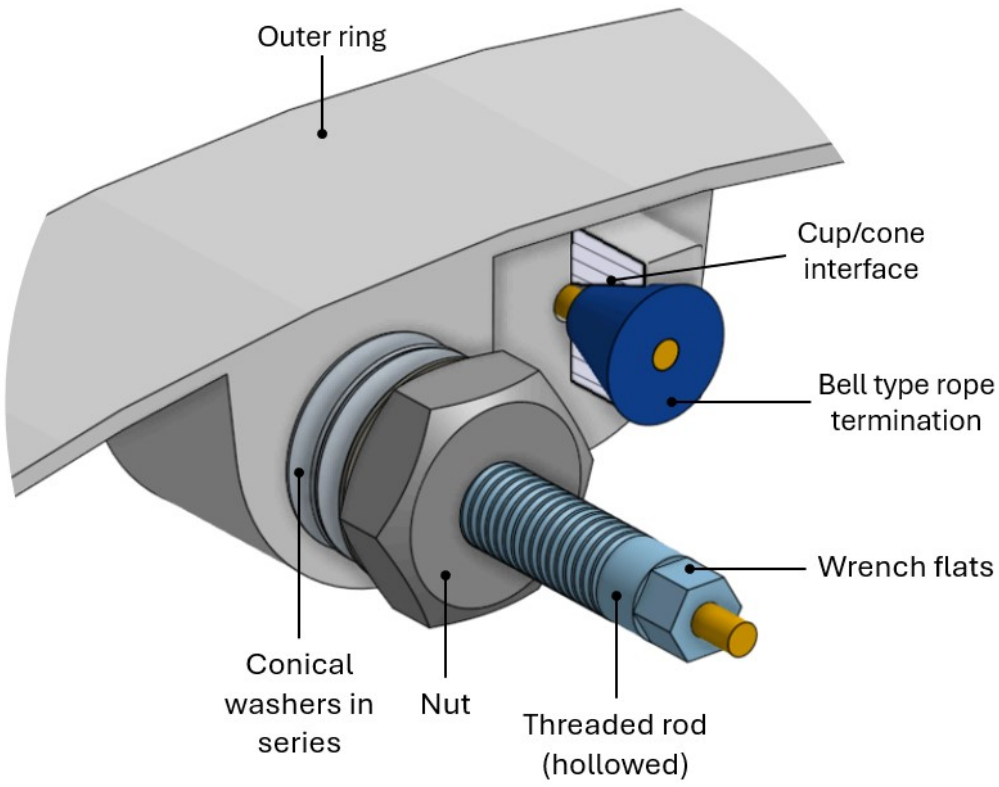

Figure 5.8: Detailed view of the anchor and tensioning system

To ensure that the zigzagging ropes maintain their preload, conical washers can be used as shown by the tensioning system of Figure 5.8. Conical washers, depicted in Figure 5.9, have a spring-like effect and are often used in bolted assemblies to prevent the loss of torque due to vibrations, thermal expansion, and creep. The spring force from a single washer is a function of the displacement and is non-linear, as shown by Almen and Laszlo [73]:

$$P = \frac{E\delta}{(1-\nu^2)M\alpha^2}\left[(h-\delta)\left(h-\frac{\delta}{2}\right)t+t^3\right] \tag{5.3}$$

where,

- P = Applied force [N]
- δ = Deflection [mm]
- h = Cone height [mm]
- t = Thickness [mm]
- a, b = Outer and inner radius from mid surface [mm]
- M = Constant that depends on a/b ratio (M=0.73 for a/b = 2.2)

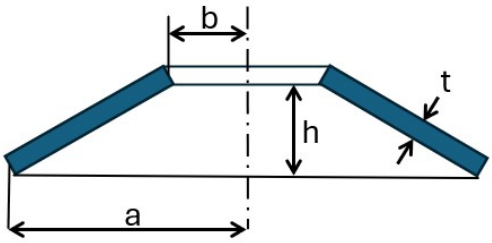

Figure 5.9: Conical washer diagram

Conical washers can be stacked to achieve different loads and deflections. Stacking two washers in parallel (facing the same direction) doubles the load capacity while maintaining the same deflection as a single washer. Conversely, stacking two washers in series (facing opposite directions) results in double the deflection for the same load as a single washer.

For instance, the load-deflection curve for a titanium conical washer with dimensions: a = 11mm, b = 5mm, t = 0.5mm, h = 1.5mm and E = 114 GPa, is shown in Figure 5.10. When four washers are stacked in series and preloaded with a deflection of 4mm, a rope tension of 550N is attained. If the ropes expand due to temperature by 2.25mm, the washer assembly accommodates this and provides a loading of 520N corresponding to a deflection of 1.75mm from the graph. Hence, conical washers can effectively maintain preload and compensate for thermal expansion by accommodating changes in deflection. This ensures stable rope tension and performance.

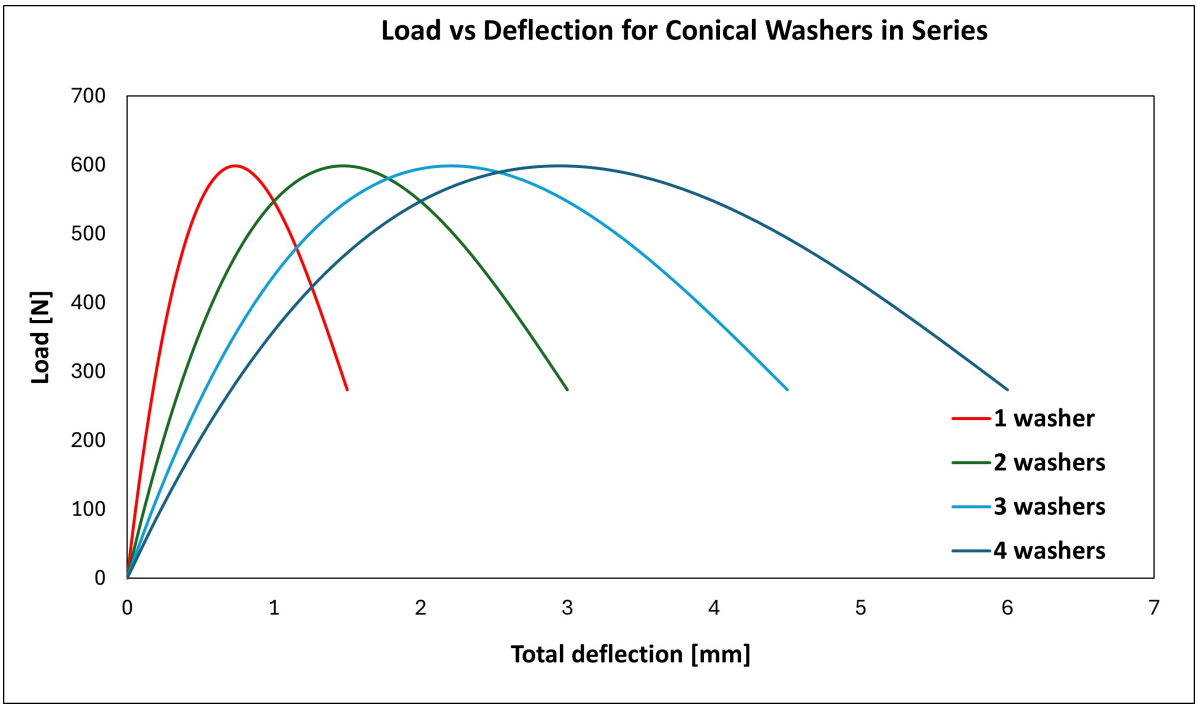

Figure 5.10: Load vs deflection for conical steel washers in series (Dimensions: a = 11mm, b = 5mm, t = 0.5mm, h= 1.5mm)

Buckling capacity increase of outer shell

The set of four aluminum rings shown in Figure 5.7 weigh approximately 2 kg. This additional weight can potentially be offset by an increase in the buckling capacity of the outer shell due to the support of these outer rings. The table below shows the required thickness of the aluminum outer shell to prevent buckling from an external pressure of 1.25 $\times$ 1 atm. In the baseline design section, it was calculated that a Gauge 12 thickness of aluminum was needed without the support of rings. The table demonstrates that the addition of the rings allows for a smaller thickness to be used. Therefore, for the current aluminum design, the addition of these rings increases the mass by 2 kg but has the potential to save 1.5 kg. Lowering the length, L, past the current point does not help much since the next possible gauge is 1.29 mm thick, which is quite thin.

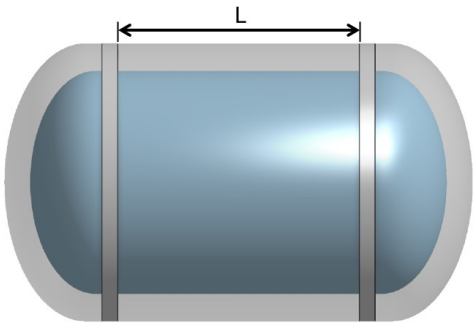

Figure 5.11: Distance between outer rings

Table 5.2: Required thickness of aluminum to prevent outer shell buckling from 1.25 $\times$ 1 atm

Length L [mm]	Required aluminium t_{shell} [mm]	Approximate mass [kg]
No rings	2.057 (Gauge 12)	8.4
560 (current)	1.707 (Gauge 14)	6.9
520	1.707 (Gauge 14)	6.9
480	1.707 (Gauge 14)	6.9
400	1.707 (Gauge 14)	6.9

The same exercise was attempted for a composite T300/N5208 outer shell, but weight savings were not possible while assuming a quasi-isotropic and balanced laminate. Currently, a $[0/\pm 45/90]_{2s}$ layup is proposed. Using a $[0/\pm 45/90]_s$ layup would lead to buckling, even with the addition of the rings. There is potential to optimize the layup and ring placement for the lightest possible construction, but this is beyond the scope of the current step and could be explored during the detailed design and optimization phase of the engineering process.

Natural frequency

The natural frequencies of the system can be determined analytically by considering the perceived stiffness of the ropes in the radial (x-y) or axial (z) directions. This is done using the square of the direction cosines between the rope and the direction of interest. For instance, the stiffness in the axial direction and the resulting natural frequency are calculated as follows:

$$\begin{aligned} k_z &= k_L \cos^2(\theta_z) \\ f_z &= \frac{1}{2\pi}\sqrt{\frac{n_r k_z}{M}} \end{aligned} \tag{5.4}$$

where,

- k_L = $\frac{EA}{L}$ = Rope stiffness [N/m]
- E = Modulus of elasticity [Pa]
- A = Cross-sectional area [m^2]
- L = Length of the rope [m]
- θ_z = Angle shown in Figure 5.12 [°]
- n_r = Number of ropes
- M = Suspended mass [kg]

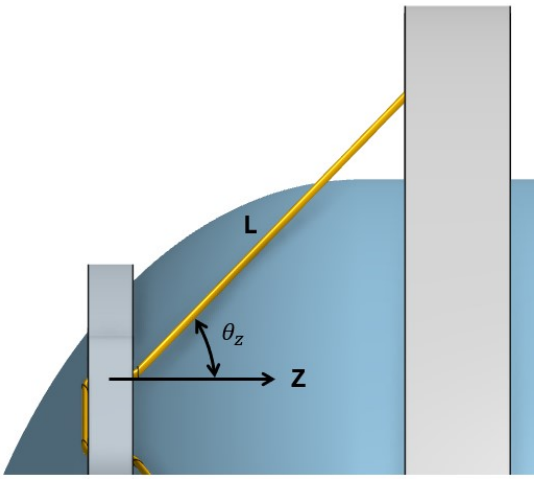

Figure 5.12: Angle of the rope with respect to the axial axis

Table 5.3 lists the values used to calculate the natural frequency in the axial direction.

Table 5.3: Rope parameters used to calculate the stiffness and expected frequency in the axial direction

Parameter	Value
Length of rope, L	0.171m
Rope diameter, D	0.0032m
Cross-sectional area, A	8.04E-6 m^2
Modulus Kevlar-29 rope, E	3E10 Pa [47]
Mass being suspended M	11.3 kg
Number of ropes, n_r	16
Stiffness of single Rope, k_L	1,411,464 N/m

Axis	Angle [°]	Stiffness[N/m]	Frequency [Hz]
z	θ_z= 55	$k_z = 464,357$ (1 rope)	$f_z = 129.1$

The frequency from Table 5.3 indicates that the stiffness of the suspension system is well above the 10 Hz minimum frequency requirement. Consequently, the rope length can be increased to enhance resistance to heat transfer, knowing that the resulting reduction in natural frequency will still meet the target criteria. As a final note, the rope angles with the radial plane were chosen such that the stiffness in the radial direction is close to the axial direction. Although, this does not need to be the case.

Rope integrity

Damaging or rupturing the rope would render the support structure entirely useless. Key considerations for ensuring rope safety and integrity include the type of termination used and measures to prevent chafing and kinking.

Rope termination is particularly critical, as the effective strength of the rope is often determined by the termination method. For instance, knot and crimp terminations can reduce the rope's breaking strength by more than 50% [74]. Recommendations for Kevlar and other high-performance fibers typically advocate for bonding [46][75]. Applied Fiber, a company specializing in fiber technologies, offers metal-bond terminations for Kevlar, including stem balls, ball shanks, cylindrical stops, and bells [74].

As illustrated in Figure 5.8, the bell-type termination is proposed for anchoring the rope to the outer ring. An integral boss feature on the outer ring creates a cup/cone interface, ensuring a compact and

secure anchor. For the tensioning side termination, a hollowed rod with epoxy is proposed such was used in [75].

Chafing and kinking can be minimized by avoiding contact between the rope and sharp surfaces and ensuring a sufficient bend radius. In the current design shown in Figure 5.7, the rings feature chamfered holes and blended edges that provide a smooth contact surface. Additionally, incorporating Teflon bushings or grommets could be considered to reduce friction and ensure that the Kevlar rope lays over a low-friction surface.

A general consideration with the rope designs (designs 3 and 4) is that concerns such as termination strength, prevention of chafing and kinking, and actual stiffness can only be fully validated through physical testing. For example, if a zigzagging rope design is considered, it would be advisable to conduct a stand-alone test on a single inner and outer ring rope assembly. A jig assembly with a load cell and screw jack could be used to strength-test the construction. Additionally, cyclic loading up to a certain percentage of the rope's strength could be considered to further increase confidence in the design. Therefore, while analytical and numerical analyses provide useful insights, they are insufficient on their own.

5.5. Design Adaptations for Aluminum vs. Composite Vessels

The design of the inner support structure is not entirely independent of the chosen vessel material, particularly when it comes to attachment methods. This is especially relevant for the inner vessel brackets of the discrete flexures in Design 1 (Figure 5.1). For an aluminum vessel, a logical joining method would be a lap-joint weld. However, if the inner vessel is made of composite material, the two primary options would be adhesive bonding or co-curing a composite bracket.

As discussed in Section 2.5.1 of the literature review, cryogenic temperatures significantly impact adhesive joints. Adhesives typically exhibit higher coefficients of thermal expansion (CTE) than their substrates. As the temperature drops, the mismatch in CTEs can lead to substantial in-plane shear stresses within the adhesive. The review concluded that adhesives like Tra-Con F113, Epotek 301-2, and Hysol 9361 are not suitable for use at such low temperatures.

However, Masterbond's EPO30LTE-LO adhesive, which has a much lower CTE than typical adhesives, could be a viable option for attaching a bracket to a composite inner vessel, as indicated by the stress results in Table 2.5.

Another option for Design 1 is to co-cure a composite bracket with the composite inner vessel. The key consideration here is to ensure that the layup of the bracket has a similar stiffness to that of the composite inner vessel, which will help prevent peeling stresses caused by the cryogenic environment.

In general, for inner support structure designs that use the vessel bosses or do not rely on rigid attachment methods—such as the boss suspension or the inner rings in the zigzagging design—the differences between aluminum and composite constructions are minimal.

5.6. Concluding Remarks

This chapter was dedicated to the "conceptualization of inner support structures" step in the engineering design process shown in Figure 3.1. It covered four different support structure concepts, providing an overview of each design, its intent, and the main considerations. The chapter began with a simplified checklist to ensure that the fundamental functional requirements were addressed in the designs. The checklist is now revisited to confirm whether the basic requirements were considered:

Table 5.4: Checklist Evaluation of Inner Support Structure Designs

Checklist question	Design 1	Design 2	Design 3	Design 4
Inner vessel constrained in six Degrees-of-Freedom?	✓	✓	✓	✓
Thermal contraction of inner vessel accounted for?	✓	✓	✓	✓
Design features and materials for thermal isolation?	✓	✓	✓	✓
Deemed capable of withstanding crash worthiness loads?	✓	✓	✓	✓

6

Analysis Methodology

With the four inner support structure concepts presented, and the primary functional and key performance requirements outlined in Section 3.2 and reiterated throughout the report, the focus now shifts to addressing a particular thesis sub-question:

> What are suitable analytical and numeral methods used to evaluate and verify the performance and behaviour of the internal support structure?

Even though analytical methods – such as those used to size vessels against pressure and temperature loads, or to estimate natural frequencies for designs involving ropes or springs – can be helpful, they quickly become insufficient when dealing with more complex geometries and analysis objectives. This limitation is already evident if considering a thermo-mechanical analysis of the Discrete Flexure (Design 1) concept. If the flexures were simple flat rectangular plates, it would be possible to estimate their state of stress analytically from an inner vessel thermal contraction. However, the situation becomes far more complicated when geometric features such as tapered cross-sections, cutouts, and fillets are introduced, as is currently the case. These complexities highlight the limitations of analytical methods, which require numerous reductive assumptions to fit complex components into a simplified equation framework.

Similar reasoning applies to modal analysis, which depends on the stiffness of the structure, among other factors. In the case of the rope designs, as discussed in Section 5.4.3, an approximation for the natural frequencies can be made by calculating the effective stiffness of the ropes in different directions. However, the ropes interact with other structural components, such as the interface flanges (Design 3) and rings (Design 4), meaning the compliance (i.e., stiffness) of these components likely will affect the modal of the structure in ways that will be difficult to capture through analytical methods.

To verify the performance requirements and design intents of the different inner support structure concepts, the **Finite Element Method (FEM)** was therefore primarily used. The Finite Element Method is a numerical technique used to approximate solutions to complex engineering problems. By discretizing a structure into finite elements, FEM provides a systematic approach to solving problems involving complex geometries, different types of material properties, and boundary conditions. This method is particularly suited for analyzing stress, strain, and deformation in structures, as well as thermal, dynamic, and non-linear behaviors [76].

This chapter outlines the general methodology used to build the Finite Element Models for the analyses discussed in the next chapter. It starts by defining the goals of the analysis and what is currently out of the scope. Next, it discusses the types of elements used for the different design concepts. It then proceeds with a description of how the CAD geometry was simplified before meshing. Following this, the FEMs for each model are presented, with annotations highlighting key features. The chapter also explains how connectors were used to simulate the spring and rod connections in the boss suspension design, and demonstrates the modeling and verification of the ropes. Additionally, there is a brief discussion on mesh refinement and the approach taken to accurately capture stresses at critical locations. Finally, the choice of boundary conditions is explained.

6.1. Defining Analysis Goals

The Finite Element Method will be employed for the following analyses, briefly outlined here and detailed in the next chapter:

- **Modal Analysis:** To identify flexible modes and ensure natural frequencies exceed a specified threshold.
- **Thermo-Mechanical Analysis:** To evaluate thermal stresses during cooling and ensure the design accommodates thermal expansion and contraction.
- **Crash-worthiness Analysis:** To verify that the structure withstands worst-case loading conditions without exceeding material limits.

At this analysis stage, fatigue life concerns are beyond the scope. However, fatigue is an important consideration for long-term safety and performance and should eventually be investigated. More complex analyses, such as damage mechanics or crash events involving a plane's floor frame crushing into the vessel, are also beyond the current scope.

6.2. Element Types

The following discusses the rationale behind the choice of elements for the various parts of the inner support structure concepts:

2D shell elements are appropriate for modeling structures that transfer both membrane stresses and bending stresses [77]. Additionally, they are well-suited for components with thicknesses that are small relative to their global dimensions. For this reason, the thin-walled inner vessels and outer shells, the flexures from Design 1, the interface flanges from Design 2, and the adapter flanges from Design 3 were modeled using 2D shell elements. The choice of using 2D shell elements over 3D elements for these components was made to avoid an excessively high node count, as the solution time grows with the cube of the number of nodes [76].

The ropes in Designs 3 and 4 were modeled using truss elements with a "No compression" material definition, accounting for the negligible stiffness of ropes under compression. Truss elements are one-dimensional rods that deform only through axial stretching [77]. The ends are hinged, meaning they do not transfer moments, in line with what is expected from a rope.

A drawback of using 2D shell elements and 1D beam/truss elements is that it requires geometry simplification (or de-featuring) to make the components suitable for meshing. The methodology followed for geometry simplification is discussed in detail in Section 6.3.

The G-10 rods in the boss suspension of Design 2 were meshed in 3D due to their relatively thick walls compared to their length. The inner rings of the zigzagging rope concept (design 4) also required 3D meshing because they are tapered to conform to the surface of the inner vessel, making it challenging to represent them with 2D shell elements.

6.3. Geometry Simplification and Other Meshing Considerations

As discussed in Section 6.2, the decision to use shell and beam/truss elements required geometry simplification to make the components capable of being meshed. An example of this process is shown in Figure 6.1, which illustrates the zigzagging rope design. A similar approach was taken for the other models. The key modifications included:

- The inner vessels, outer shells, flexures, interface flanges, and adapter flanges were converted to mid-surfaces.
- The ropes were idealized as discrete wire features connecting the centers of the holes.

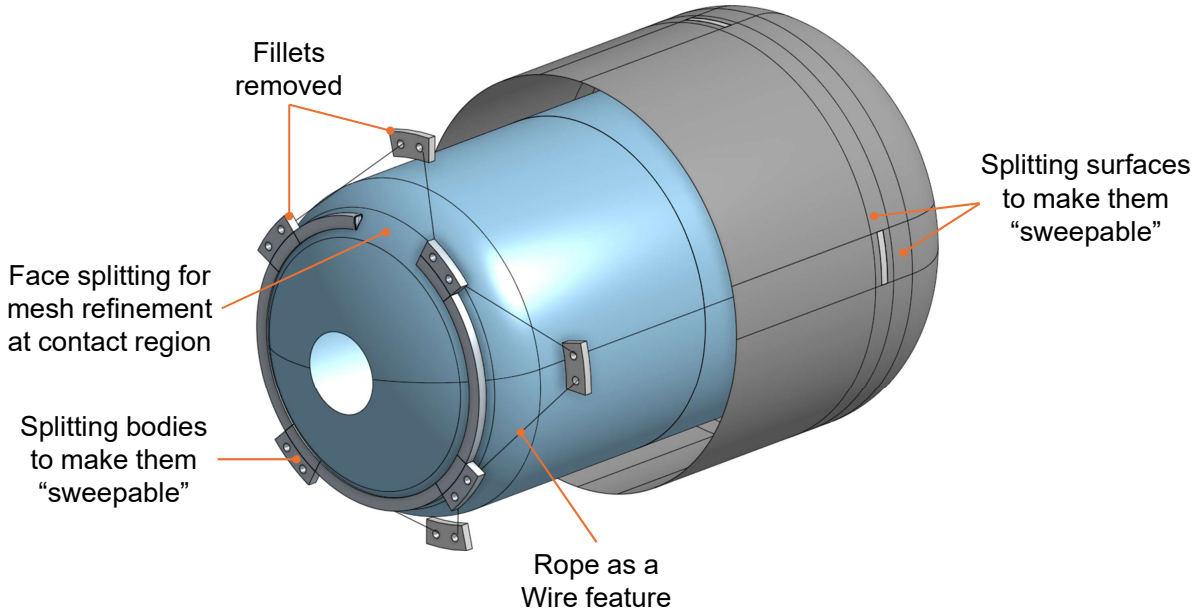

Figure 6.1: Idealization of the zigzagging rope model prior to meshing

In addition to geometric simplifications, other modifications were applied to the geometry, as illustrated in Figure 6.1. Bodies and faces were split to facilitate the creation of structured 2D quadrilateral elements or 3D hexahedral elements, which provide more accurate results with fewer elements compared to triangular and tetrahedral elements, respectively [77]. A structured mesh was achieved using the swept-meshing feature in the pre-processing environment. For 3D bodies, such as the rings, it was necessary to remove features like fillets, edge blends, and chamfers to ensure the meshing algorithm worked properly.

The decision to remove these features was mainly based on the analysis goals mentioned in Section 6.1. Since fatigue life is not currently part of the scope, capturing stress concentrations at these locations is unnecessary. Keeping these features would require tetrahedral meshing, which would increase computation time without adding value to the results. However, this is an important consideration for future analyses, as fatigue life is highly sensitive to stress concentrations - a 10% increase in stress can lead to an order-of-magnitude reduction in fatigue life [76].

6.4. Finite Element Models

Figures 6.2 through 6.5 display the meshes of the four design concepts. Most elements in these models are S4R linear quadrilateral elements. As shown in the figures, geometric defeaturing and other surface/body modifications resulted in all models being swept meshed into structured elements.

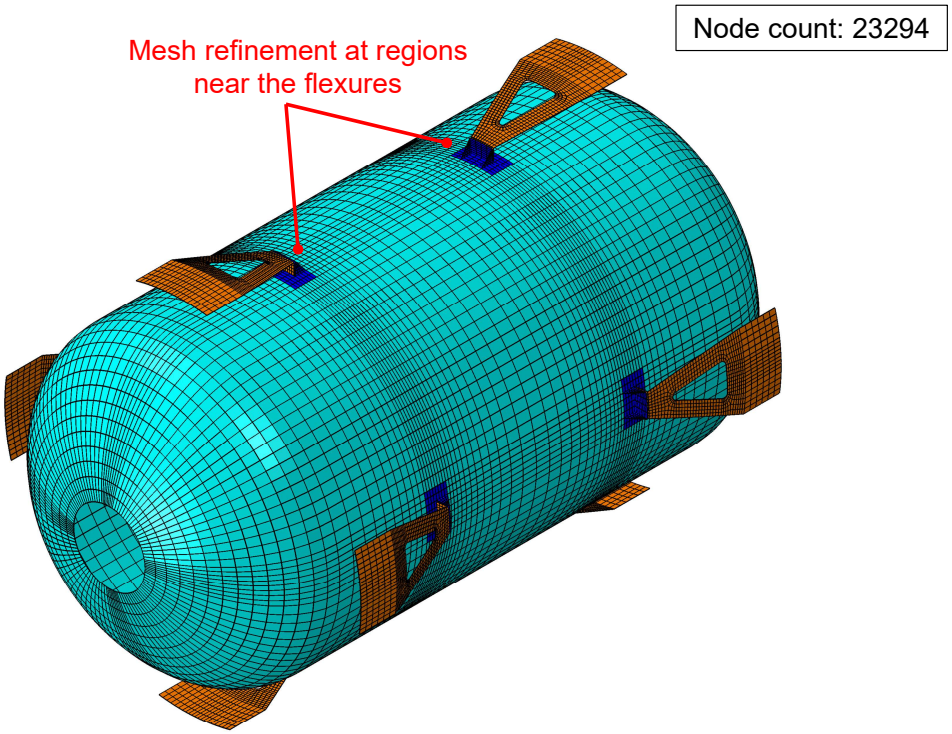

Figure 6.2: FEM of the discrete flexure design used for analysis (outer shell hidden)

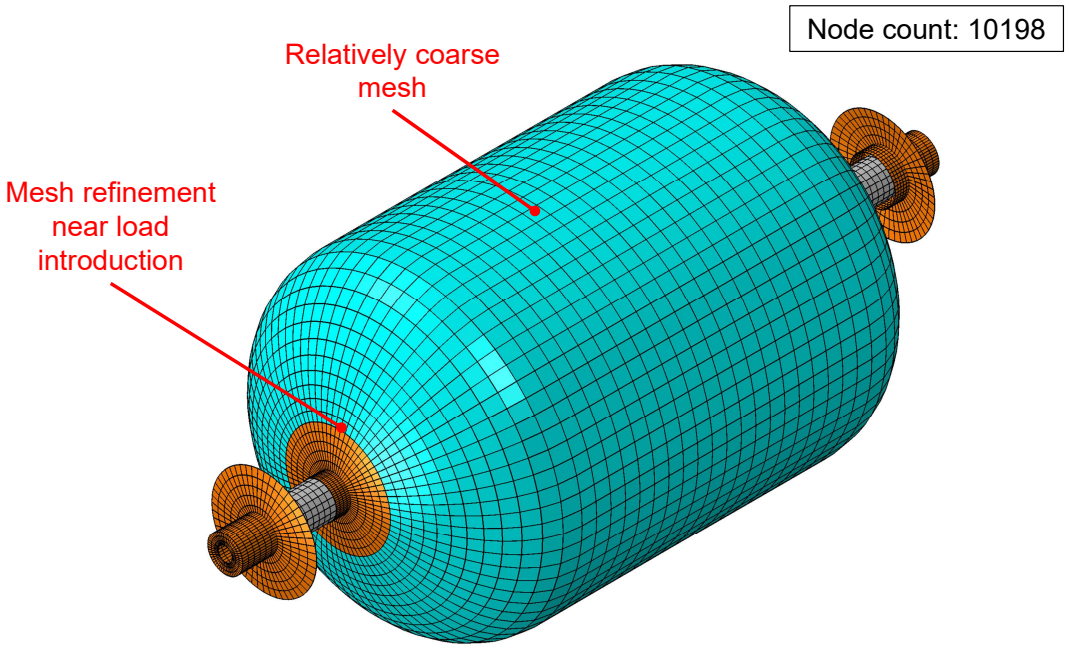

Figure 6.3: FEM of the boss suspension design used for analysis (outer shell hidden)

Local mesh refinement on the inner vessel was applied at specific locations were there is a load introduction from the inner support structures, such as next to the flexure brackets (Figure 6.2), interface flanges (Figure 6.3), adapter flanges (Figure 6.4) and ring contact surfaces (Figure 6.5). The strategy for mesh refinement and model convergence is discussed in more detail in section 6.7.

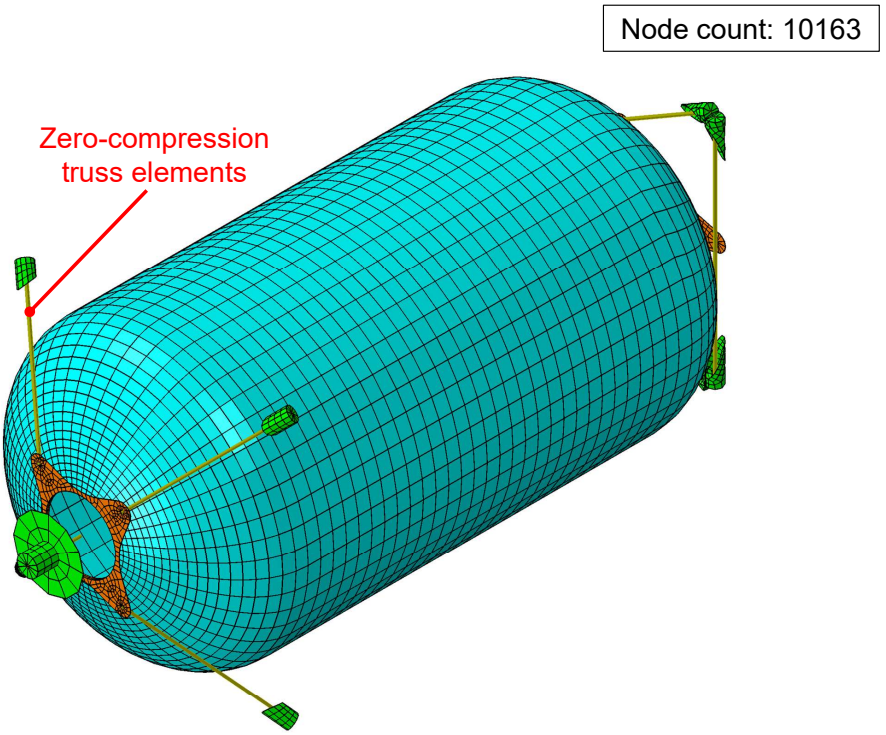

Figure 6.4: FEM of the kinematic mount design used for analysis (outer shell hidden)

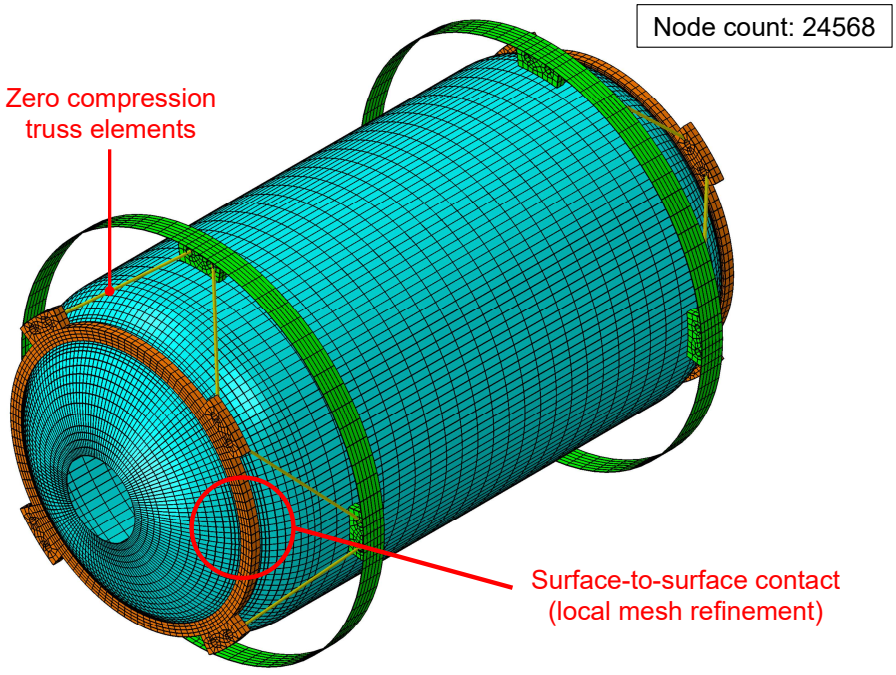

Figure 6.5: FEM of the zigzagging rope design used for analysis (outer shell hidden)

6.5. Making Use of Connectors

The boss suspension design, shown in Figure 5.4, features a G-10 rod compressed between two flanges by a spring. To prevent relative torsional motion, a D-shaft/bore feature is included. Consequently, the G-10 rod must be able to carry moments and torsion while allowing one end to slide axially inward or outward with the spring's deflection. This setup is modeled using connectors placed at the inner and outer flanges, as illustrated in Figure 6.6.

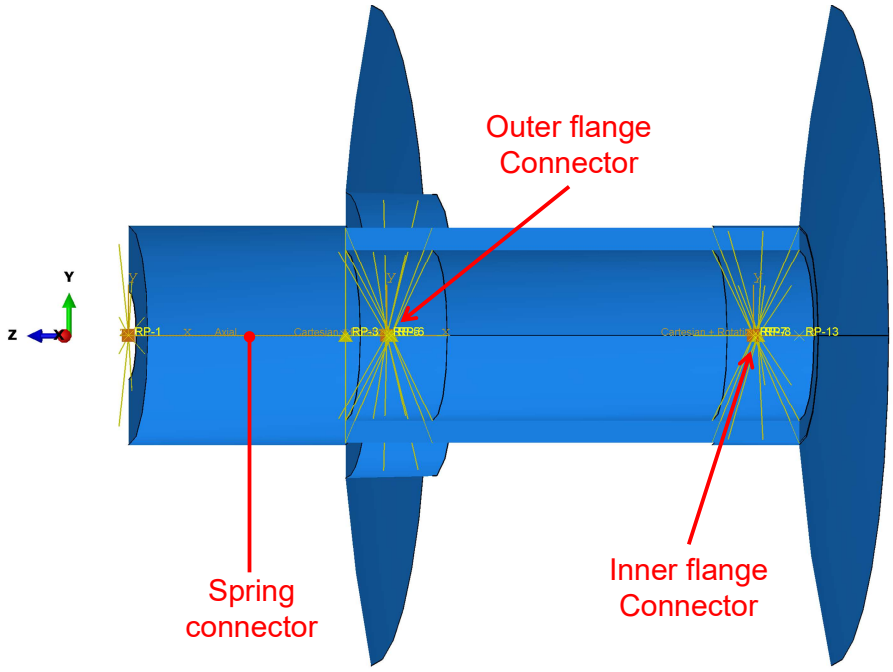

Figure 6.6: Cross-section of the spring-rod-flange model using connectors

Each connector has two nodes: one node is connected to the rod through a set of continuum distributing elements, while the other node connects to the flange via its own set of continuum distributing elements. Table 6.1 right below summarizes the stiffness for each connectors used. The outer flange connector has zero stiffness in the axial direction, z, meaning that relative motion between the rod and flange are allowed. The compressive spring is modelled as an axial connector with a stiffness of 95N/mm only when its deflection is less than 0 (under compression). If the spring elongates more than its free length, the stiffness becomes 0 N/mm.

Table 6.1: List of connectors and their stiffness in different directions

	Stiffness					
Connector name	**Translation** x	**Translation** y	**Translation** z	**Rotation** x	**Rotation** y	**Rotation** z
Spring	0	0	95 N/mm	0	0	0
Outer flange	∞	∞	0	∞	∞	∞
Inner flange	∞	∞	∞	∞	∞	∞

To verify the modeling accuracy, a spring preload of 1000 N, corresponding to an initial deflection of 10.5 mm, was applied to the model. Analytical calculations yield a nominal stress of 1.45 MPa, while the model results in a stress of 1.47 MPa, as shown in Figure 6.7.

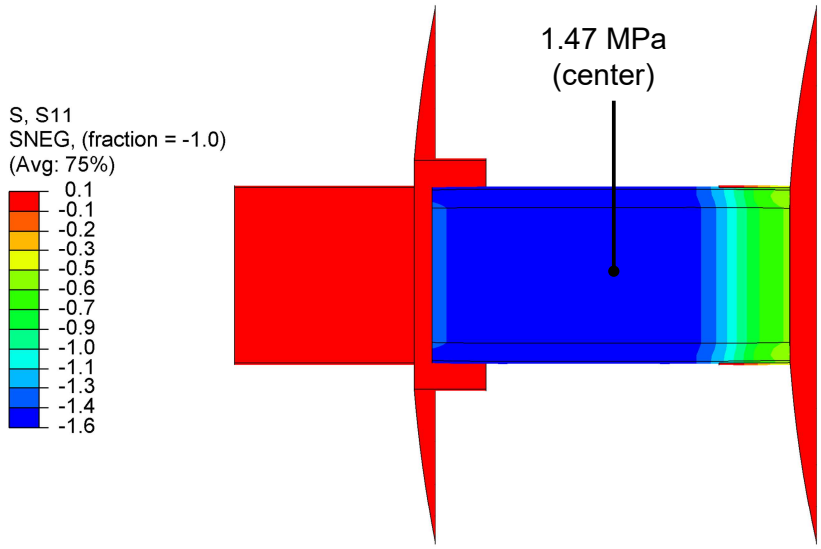

Figure 6.7: Stress in G-10 rod following spring preload (z-axis along the rod's length)

An alternative to the connector approach is to model contact between the rod and flanges, but this is computationally heavy and not needed at this stage of analysis.

6.6. Modelling of Kevlar Ropes

As previously mentioned, the Kevlar ropes are modeled using truss elements with zero compression. Figure 6.8 illustrates a stand-alone setup of the zigzagging rope design, which was used to verify the modeling intent. In this setup, the truss elements are connected from the centre of one hole to the centre of the opposite hole. Continuum distributing constraints are applied to secure the nodes of each truss element to the interior surfaces of the holes.

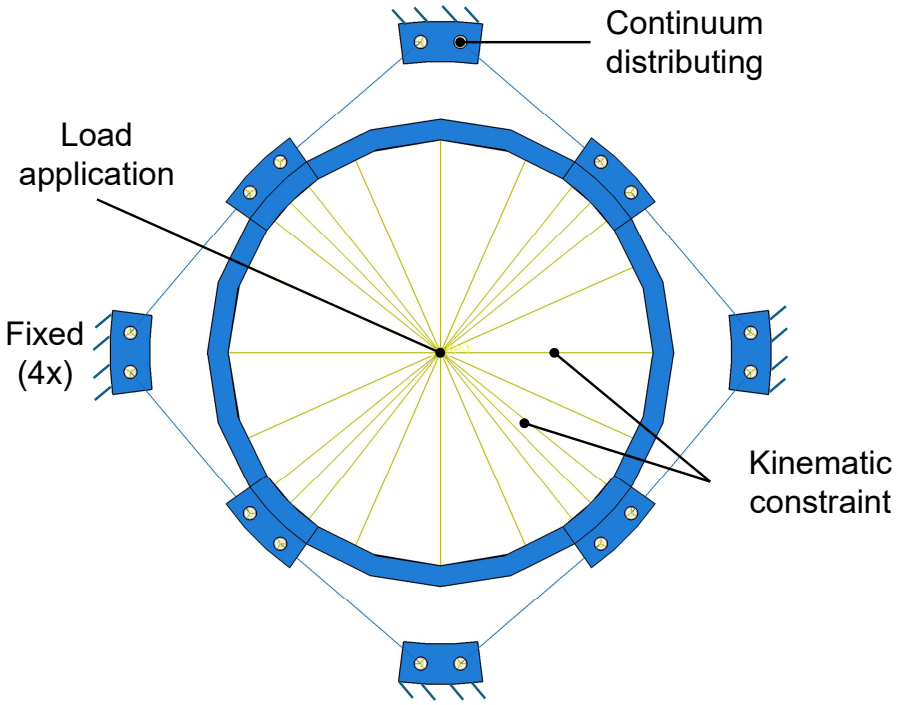

Figure 6.8: Overview of the stand alone model used to verify the modelling approach of the ropes

To verify the modelling intent, analytical calculations for the displacement of the inner ring under a load were compared to the FEA results. The analytically displacement was simply calculated as:

$$u_i = F_i / k_i \tag{6.1}$$

where,

- u_i = Displacement in the ith direction [mm]
- F_i = Force in the ith direction [N]
- k_i = Total stiffness in the ith direction (see Section 5.4.3 for calculation procedure) [N/mm]

The FEA results for a 1000 N load applied both axially and radially are shown in Figure 6.9. Table 6.2 compares the analytical and numerical results, demonstrating that they are nearly identical.

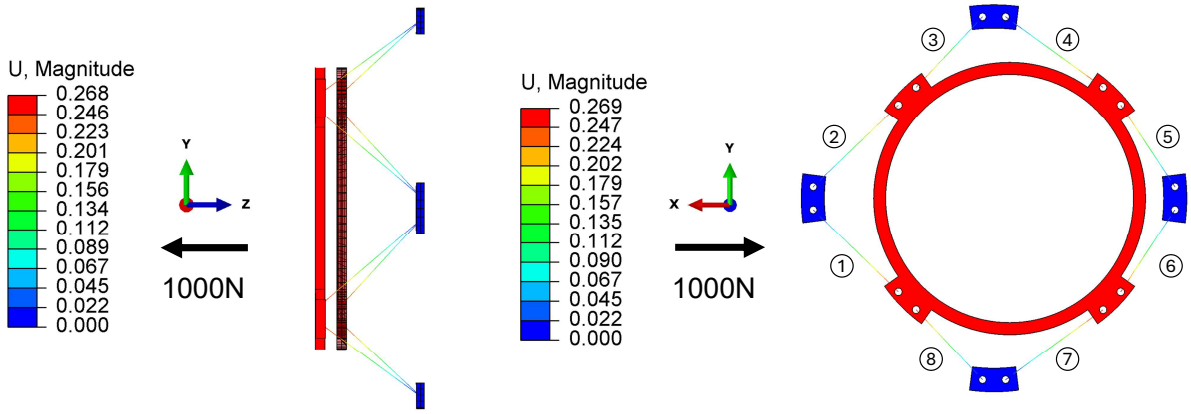

Figure 6.9: Displacements in mm for a 1000N load applied axially (left) and radially (right)

Table 6.2: Comparing the analytical and numerical displacements from a load of 1000N in both axial and radial directions

		Displacement from 1000N		
Direction	**Stiffness (8x ropes) [N/mm]**	**Analytical [mm]**	**Numerical [mm]**	**Percent difference [%]**
Axial	3714.9	0.269	0.268	0.37
Radial	3758.4	0.266	0.269	1.1

Table 6.3 shows the load change for each of the ropes from an external radial loading (Figure 6.9, right). It is interesting to observe that ropes with a preload opposite to the applied load experience an increase in overall load, while those aligned with the load see a corresponding decrease. This is a good sign, as it confirms the expected mechanics of preloaded ropes subjected to an external force.

Table 6.3: Load change in the ropes after applying 1000N in the radial direction

Rope ID	Load change (N)
1	+198.4
2	+198.4
3	-233.5
4	+233.5
5	-198.4
6	-198.4
7	+233.5
8	-233.5

The mechanics of preloaded ropes can be explained using the simplified schematic in Figure 6.10, which depicts two initially preloaded ropes in series. When an external force is applied, the resulting load in each of the ropes can be described as follows:

$$\begin{aligned} F_A &= F_P + \left(\frac{K_A}{K_A + K_B}\right) F_{ext} = F_P + \frac{1}{2} F_{ext} \\ F_B &= F_P - \left(\frac{K_B}{K_A + K_B}\right) F_{ext} = F_P - \frac{1}{2} F_{ext} \end{aligned} \tag{6.2}$$

where,

- F_A, F_B = Overall load in rope A and B, respectively.
- F_P = Initial preload
- K_A,k_B = Stiffness of rope A and B, assumed to be equal in equation 6.2
- F_{ext} = External force

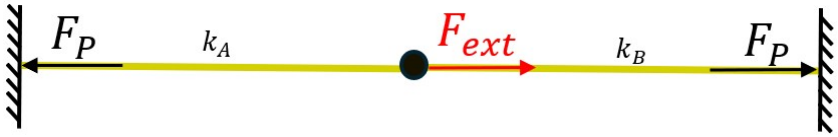

Figure 6.10: Simplified rope setup illustrating the effect of rope preload

As shown, each rope will carry half of the external load. This verification also highlights an important consideration in determining the appropriate preload for the ropes. Namely, if the external load is so high that the preload in one rope drops to zero, the other rope will bear the entire external force, which can be dangerous if it exceeds the rope's strength.

6.7. Model Convergence

Mesh refinement involves increasing the density and quality of the mesh by using smaller elements to discretize the components. This process is essential because as the mesh becomes finer, the numerical solution becomes more accurate, closely approximating the true physical behavior of the system [78].

The general process of mesh refinement used included [78]:

1. Running the simulations with a relatively coarse mesh to identify regions of peak stress and high stress gradients.
2. Refining the mesh in these regions or components and conducting a convergence study until the difference between two consecutive results is less than 5%.

Figure 6.11 demonstrates the mesh refinement process for the flexures in Design 1. The stress plots correspond to thermo-mechanical loading due to an inner vessel contraction from a temperature change of $\Delta T = -270°$C. Peak stresses are observed at the bottom corners. Initially, the coarse mesh gives a stress of 3.72 MPa, which is 7% lower than that obtained with the more refined mesh in the center of the figure. The rightmost image shows an exaggerated mesh refinement, resulting in a stress only 2.2% higher than the previous result. Therefore, the flexure with 422 elements was deemed sufficient for the analyses.

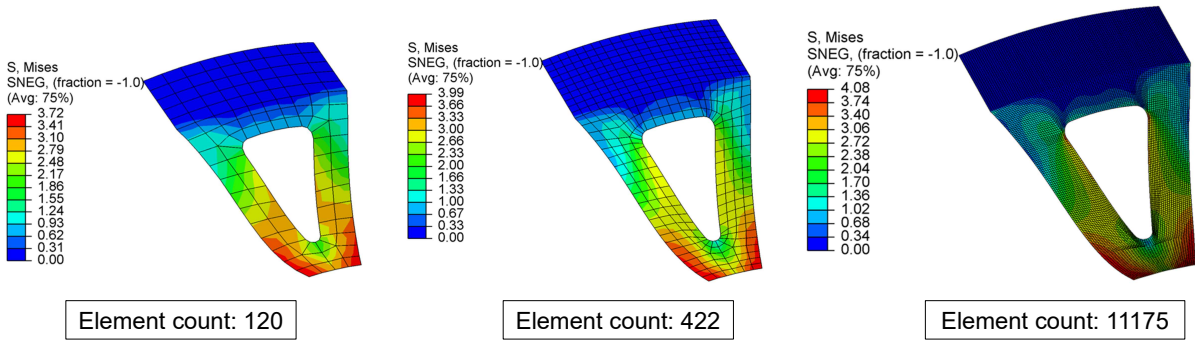

Figure 6.11: Mesh refinement on the flexures

6.8. Boundary Conditions

The common boundary condition used is fixing the boss ends of the outer shell. This secures the model without directly influencing the behavior of the inner support structure and inner vessel. Additionally, it accounts for the compliance of the outer shell, which is particularly important for Designs 1, 3, and 4.

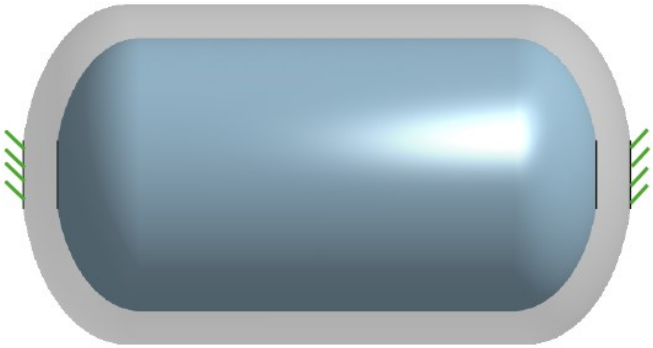

Figure 6.12: Common boundary conditions for the models

A small modification was made to the boss suspension (design 2) boundary conditions by allowing one end to move freely in the axial direction. This modification is essential for assessing the impact of the preloaded springs on the outer shell. Without this adjustment, the preloading step would result in zero stress in the outer shell, which does not accurately represent real-life conditions.

6.9. Chapter Conclusions

This chapter provided an overview of the development process for building robust finite element models of the four designs that will be analyzed in the next chapter. It highlighted the modeling methods used for representing the spring, rod, and Kevlar ropes, and included mathematical checks to verify the modeling approaches. The chapter also detailed the process of mesh refinement to ensure the accuracy of stress results. Finally, it explained the common boundary condition applied across the designs.

7

Analysis Results

This chapter focuses on analyzing the inner support structure concepts introduced in Chapter 5. It begins with a modal analysis, followed by a thermo-mechanical analysis, a crash load analysis, and a heat transfer analysis. Each section explains the reasons for performing the analyses, describes the model setup and the main assumptions, and presents the results with a brief discussion for each design concept.

7.1. Modal Analysis

The purpose of a modal analysis in the context of this project is twofold [79]:

- **Identification of flexible modes**: The first objective is to ensure that all observed modes are flexible modes and not rigid body modes. Rigid body modes refer to the natural modes of vibration where the entire structure moves as a rigid body without any deformation. If the support structure fails to constrain the inner vessel in all six degrees of freedom, such a mode would be observed. The absence of rigid body modes for the inner vessel is a strong indication that functional requirement **REQ-01** of the support structure has been satisfied.
- **Avoiding resonance**: The second purpose of modal analysis is to understand the dynamic behavior of the system. Requirement **REQ-04** specifies that the minimum natural frequency shall be above 10 Hz to ensure that the vessel's resonant frequency is higher than the typical driving frequencies encountered in an airplane. Resonance between the vessel and driving frequencies can lead to a dynamic amplification, potentially causing structural damage.

Natural frequencies depend on boundary conditions, system mass, and structural stiffness [79]. As explained in Section 6.8, all models have the same boundary conditions, where the bosses of the outer shell are constrained. For stiffness, material properties at room temperature were used. Regarding mass, the inner vessel is assumed to be completely filled with LH2, modeled by applying a non-structural mass of 6.5 kg evenly distributed over the inner vessel's surface. Hence, the effect of sloshing, or the movement of liquid hydrogen due to external forces, is neglected for this analysis. While this simplification reduces analysis complexity, it leads to an inaccurate prediction of the true dynamic behavior of the structure by ignoring changes in mass distribution, coupling of sloshing modes with structural vibrations, and varying fluid levels. Therefore, the results below do not represent the structure's actual behavior under real conditions, and this aspect may be worth investigating eventually.

Design 1: Discrete flexures

The discrete flexures made out of unreinforced Teflon provide sufficient stiffness to produce a radial translation mode at 31.5 Hz. If a higher fundamental frequency is required, more flexures can be added without compromising the design intent described in Figure 5.2.

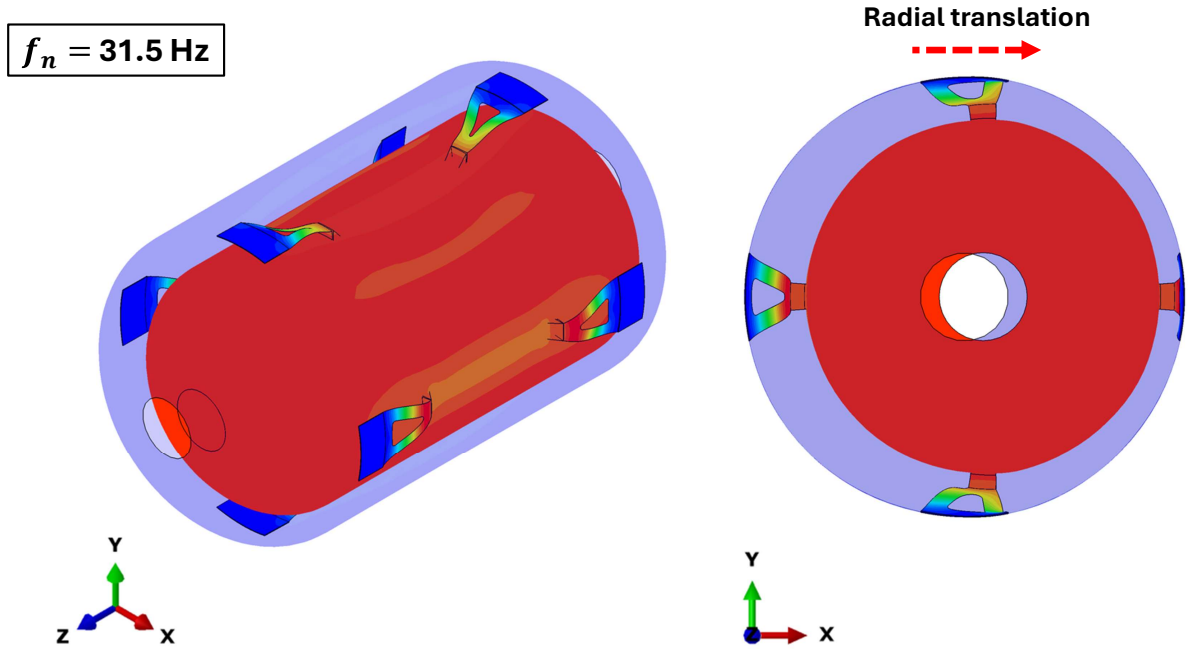

Figure 7.1: Design 1 mode shape and fundamental frequency

Design 2: Boss suspension

The resulting mode shape and frequency for the boss suspension correspond precisely to the predictions in 5.2.3. Thus, the frequency can be easily tailored by selecting an appropriate spring rate. The next mode occurs well above this one, at over 65 Hz.

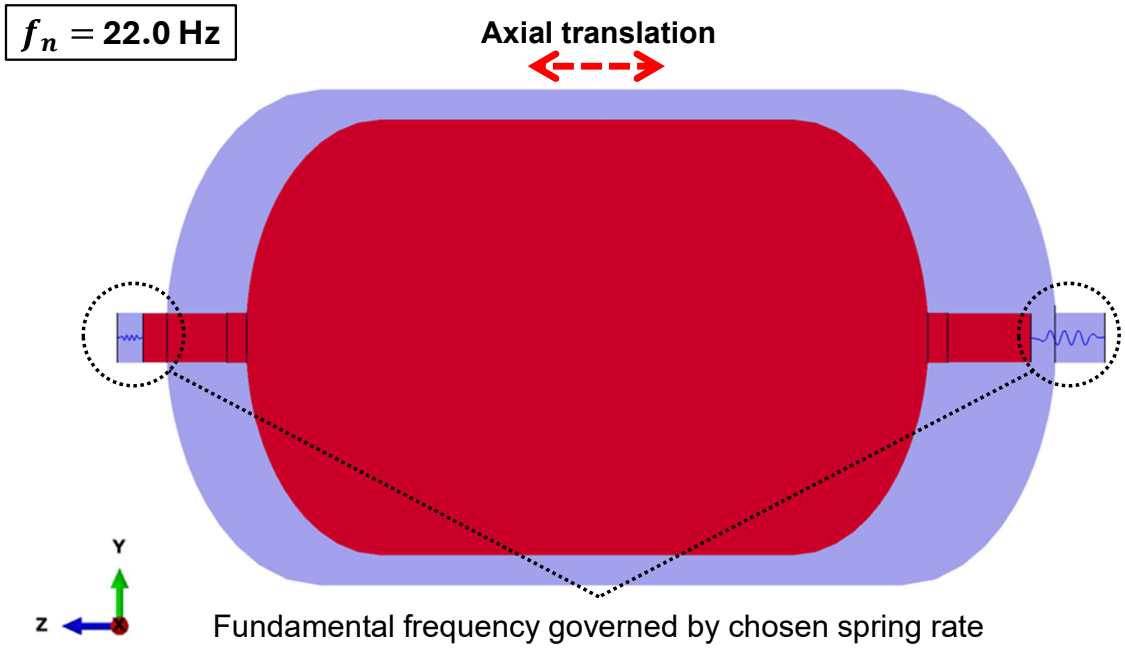

Figure 7.2: Design 2 mode shape and fundamental frequency

Design 3: Kinematic mount

The kinematic mount design results in an axial translation mode with a relatively low fundamental frequency of 37.1 Hz. This outcome is expected, as only the five front ropes contribute to axial stiffness.

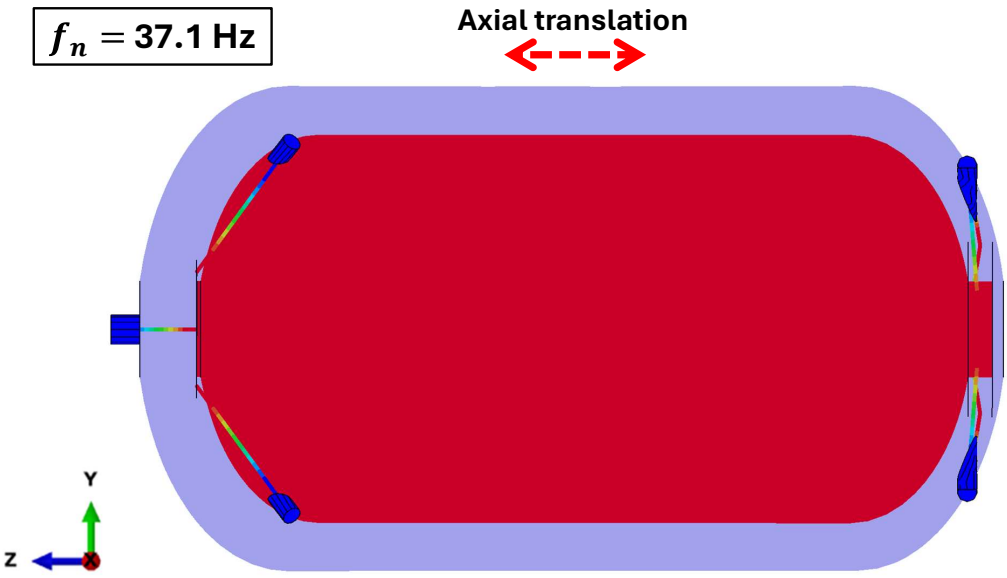

Figure 7.3: Design 3 mode shape and fundamental frequency

Design 4: zigzagging rope

Section 5.4.3 predicted the axial translation mode to be 129.1 Hz, or nearly 30% higher than the result shown in Figure 7.4. This discrepancy occurs because the rings have compliance, in line with the discussion of Chapter 6 on the limitations of analytical calculations. In fact, when a fixed boundary condition was added to the outer rings to verify this, the resulting mode was nearly 129 Hz. As anticipated, a radial translation mode follows, consistent with the stiffness results discussed in Section 6.6.

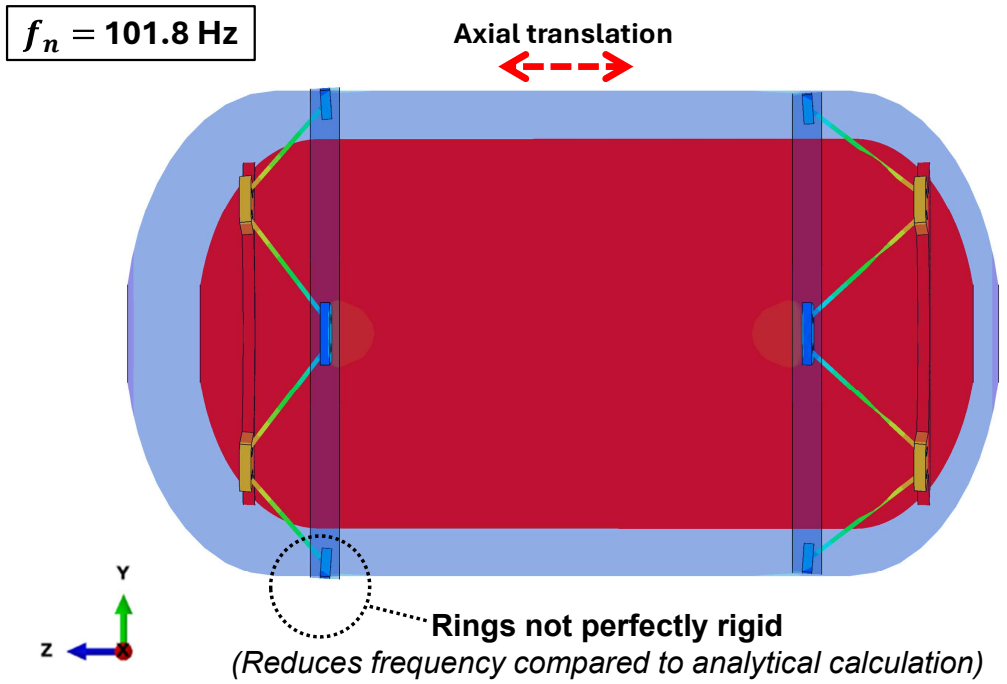

Figure 7.4: Design 4 mode shape and fundamental frequency

7.2. Thermo-Mechanical Analysis

Thermo-mechanical analysis is crucial for examining inner support structure concepts. During refueling, the thin-walled inner vessel rapidly cools from 293K (21°C) to 20K (-253°C), which can lead to significant thermal stresses if over constrained. Hence, **REQ-02** mandates a functional design that limits these stresses by accommodating the thermal expansion and contraction of the inner vessel.

To demonstrate the significance of thermo-mechanical stresses and the risks of over-constraining an aluminum inner vessel (IV) to the outer shell (OS), a series of simple simulations were conducted:

The top image in Figure 7.5 illustrates a “floating” inner vessel. In this scenario, a uniform temperature drop induces zero stress in the parts, as expected. The bottom left image shows the effect of preventing the longitudinal contraction of the inner vessel by rigidly attaching a solid aluminum rod between the bosses. The bottom right image depicts the effect of preventing the radial contraction of the inner vessel by rigidly attaching a solid aluminum ring between the adjacent shells. In both of the latter cases, it can be observed that the thin aluminum inner vessel stresses well past its yield strength.

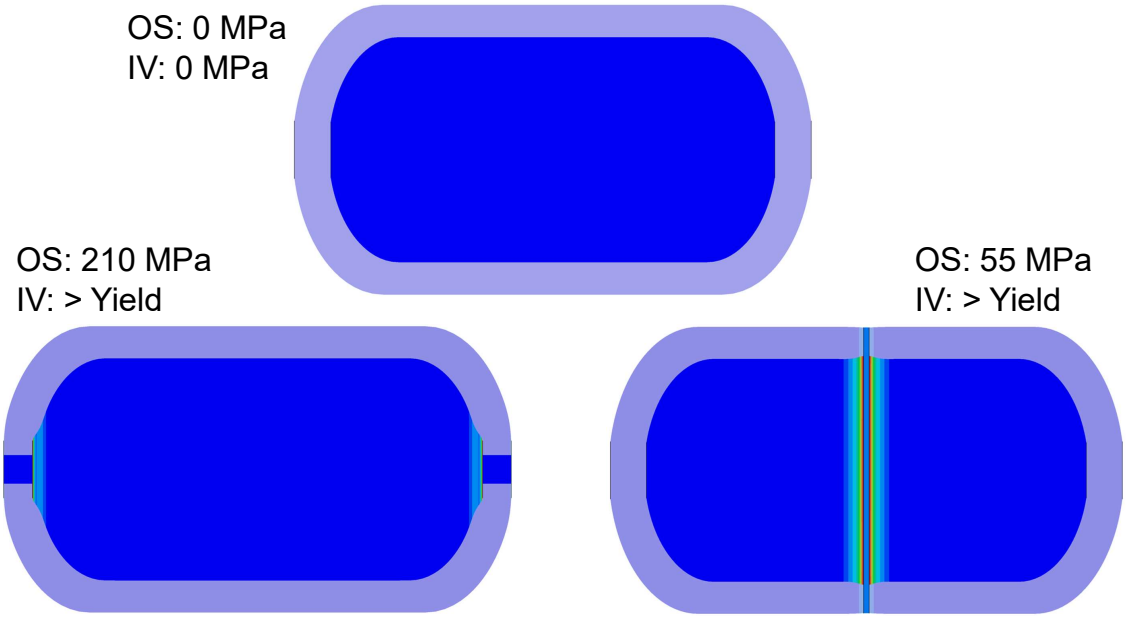

Figure 7.5: Effects of thermal loading on floating vs constrained aluminum inner vessel

The results of the thermo-mechanical analyses for the four designs are presented from Figures 7.6 through 7.9. A few points should be mentioned:

- An aluminum inner vessel is used instead of a composite one because the default state of stress from a uniform temperature change is zero. This makes it easier to observe the effects of different inner support structures on the inner vessel. Additionally, the thermal contraction of aluminum is greater than that of CFRP, which makes the analysis more conservative.
- In scenarios where preloads are applied, the stress values for preloads followed by the thermal step are shown.
- For each design, a uniform temperature drop from 293K (20°C) down to 20K (-253°C) is applied solely to the inner vessel.
- Material properties at room temperature were used.

Design 1: Discrete flexures

The deformed plot in Figure 7.6 illustrates that the unreinforced Teflon flexures effectively comply with the thermal contraction of the inner vessel, resulting in a stress of 19.9 MPa on the thin inner vessel. Although some interaction between facing flexures is observed, leading to a “dog bone” appearance, the surrounding area remains largely unstressed. This suggests that increasing the number of flexures from 8 to 12, for example, should not significantly increase the magnitude of stress, provided they are not placed too close to each other.

The resulting maximum stress and strain of the flexure are 4.0 MPa and 0.0073, respectively. This analysis assumes material properties at ambient temperature, yet the observed strain is still an order of magnitude lower than the failure strain of unreinforced Teflon at 77K, as shown in Table 5.1 (percent elongation at break/100).

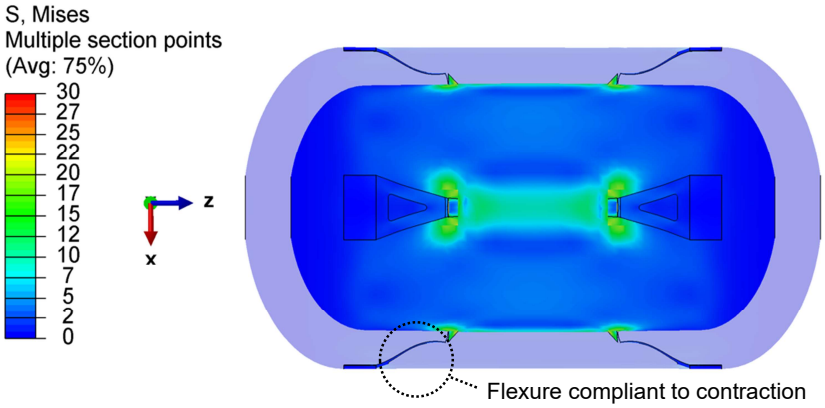

Component	Max V-M (MPa)
Inner vessel	19.9
Inner vessel to flexure brackets	29.7
Flexures	4.0
Outer vessel to flexure adhesive	1.5
Outer vessel	5.7

Figure 7.6: Design 1 stress state following thermo-mechanical loading

Design 2: Boss suspension

The compression springs used in the boss suspension design each have a spring rate of 95 N/mm. An initial compression of 10.5 mm provides a preload of 1000 N on the system, which imposes stress on the components, as seen in the table in Figure 7.7. Due to the thin aluminum thickness, the regions around the bosses are stressed, but the inner vessel remains largely unstressed. As a sanity check, it was separately verified that this preload is below the buckling limit of the dome ends of the inner vessel.

The springs effectively accommodate the thermal contraction of the vessel by expanding approximately by the same amount as the longitudinal contraction of the inner vessel. Consequently, a lower preload and stress are observed, as illustrated in the right most column.

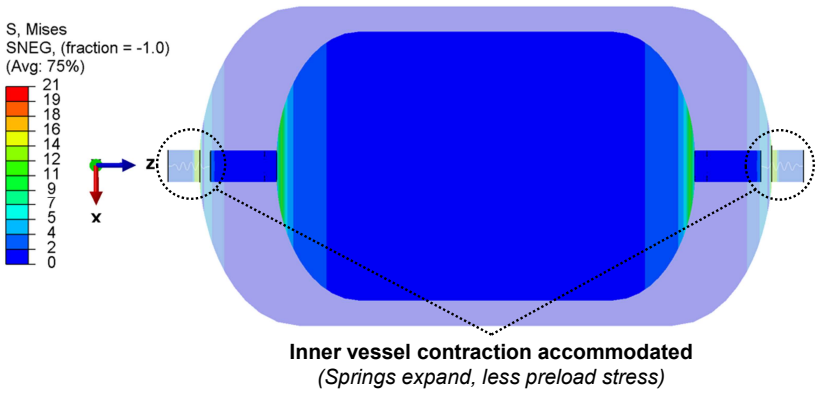

Component	Preload Only	Preload + Thermal
	Max V-M (MPa)	Max V-M (MPa)
Inner vessel	14.2	12.1
G-10 CR rods	1.5	1.1
Outer vessel	4.7	4.0
Springs (Hand calcs)	Torsion Stress (MPa)	Torsion Stress (MPa)
	227.7	193.9

Figure 7.7: Design 2 stress state following thermo-mechanical loading, springs initially compressed to 1000N

Design 3: Kinematic mount

The results from Figure 7.8 indicate that the intended purpose of the kinematic mount has been achieved. Specifically, as the inner vessel contracts, the back ropes simply rotate about their ends, allowing the vessel to move freely. The use of adapter flanges for the rope attachments ensures that the inner vessel experiences virtually zero stress from both the preload and the subsequent thermal contraction.

One possible concern with this concept is the stress on the outer vessel caused by the preloaded ropes. As indicated by the table, the current attachments on the outer vessel impose regions of localized stress. These regions may need to be reinforced.

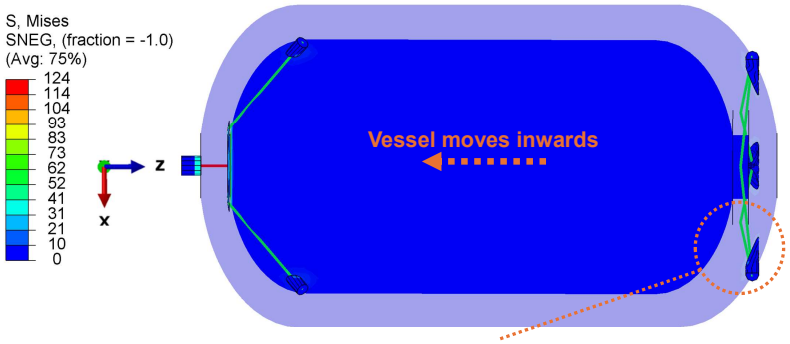

Back ropes allow inner vessel contraction
(Ropes rotate about their ends)

Component	Preload Only	Preload + Thermal
	Max V-M (MPa)	Max V-M (MPa)
Inner vessel	≈ 0	≈ 0
Outer vessel	53.2	53.2
Ropes	**Max Load (N)**	**Max Load (N)**
Axial rope	1000	1000
Front ropes	480	480
Back ropes	500	500

Figure 7.8: Design 3 stress state following thermo-mechanical loading

Design 4: Zigzagging rope

A surface-to-surface contact definition was applied between the inner rings and the inner vessel to simulate the contact pressure resulting from the rope preload. A 550 N preload produces a stress of 22.9 MPa on the inner vessel. Since the ropes are tilted relative to the radial and tangential planes of the inner vessel, thermal contraction causes the ropes to rotate about their ends rather than changing their lengths. This design intent is validated by the fact that the rope preload remains consistent across the two simulation steps.

Note that the increase in Kevlar rope length due to cooling or creep was not modeled, as the primary assumption of this model is that the conical spring washers, as shown in Figure 5.10, will maintain the preload. Consequently, this analysis primarily focuses on observing the behavior of the ropes in response to the contraction of the inner vessel.

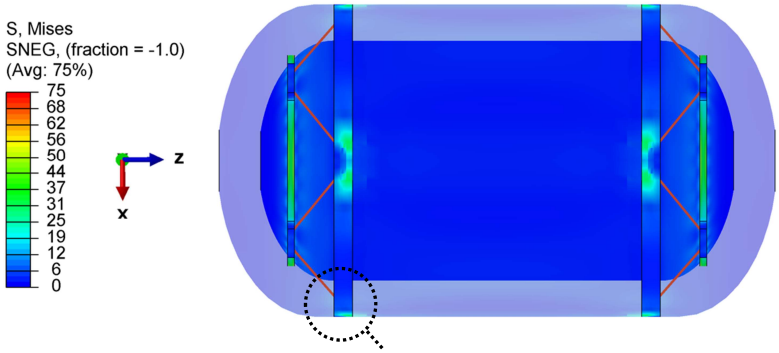

Ropes tilted from radial and tangent planes
(Accommodates vessel contraction)

Component	Preload Only	Preload + Thermal
	Max V-M (MPa)	Max V-M (MPa)
Inner vessel	22.9	22.9
Inner rings	74.8	74.7
Outer rings	29.7	29.8
Outer vessel	22.1	22.2
Ropes	**Max Load (N)**	**Max Load (N)**
	550	550

Figure 7.9: Design 4 stress state following thermo-mechanical loading

7.3. Crash Worthiness Loads

This section represents the final usage of the Finite Element Analysis and simulates the worst-case scenario loading event that the complete vessel structure will experience. A positive outcome of this analysis is that the stresses in all components remain within their structural limits.

Requirement **REQ-08** specifies that the complete structure, under nominal operating temperatures and pressures, **SHALL** withstand the following load factors:

- **Sideward:** $n = 1.5G$
- **Forward:** $n = 9.0G$
- **Downward:** $n = 6.0G$

The results, as depicted in Figures 7.10 to 7.13, illustrate the stress states of each of the four designs when subjected to a 9G load in the forward direction under operational conditions. The analysis incorporates the following sequential load steps:

1. **Preloading step** (if applicable)
2. **External Pressure step** $\rightarrow$ External pressure on the outer vessel at 1 atm (pulling a vacuum)
3. **Thermal step** $\rightarrow$ Cooling the inner vessel from 20°C to -253°C (filling the vessel with LH2)
4. **Internal Pressure step** $\rightarrow$ Nominal internal pressure of 5 bar
5. **Crash Loading step** $\rightarrow$ 9G gravity load applied in the forward (radial) direction

The results presented below focus exclusively on the 9G load in the forward direction, as this represents the worst-case scenario. Similar to the modal analysis, the inner vessel is assigned a non-structural mass of 6.5 kg, corresponding to a fully filled LH2 tank. The inner vessel and outer shell are modelled with aluminum since this is deemed as being conservative with respect to the weight and thermo-mechanical displacements. Once again, the boundary conditions involve fixing the boss-ends of the outer shell as shown in Figure 6.12 and the material properties at room temperature are used.

Design 1: Discrete flexures

The flexures react to the 9G load well, largely due to the fact that the load is distributed over the eight flexures. As a result, the Teflon flexures are well within their failure limits (see Table 5.1). The highest stress in the inner vessel is shown to occur adjacent to the flexure bracket which is an expected outcome as this is were the load is introduced.

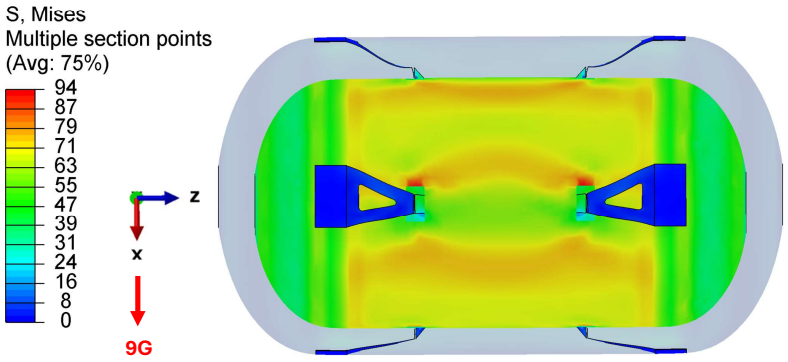

Component	Max V-M (MPa)
Inner vessel	94.4
Inner vessel to flexure brackets	66
Flexures	9
Outer vessel to flexure adhesive	5.4
Outer vessel	26.1

Figure 7.10: Design 1 stress state under combined 9G forward crash load, operational pressure, and temperature conditions

Design 2: Boss suspension

The G-10 rods are well below their strength limits. The inner vessel experiences higher stresses due to the increased radius, which in turn results in higher hoop and longitudinal pressure stresses.

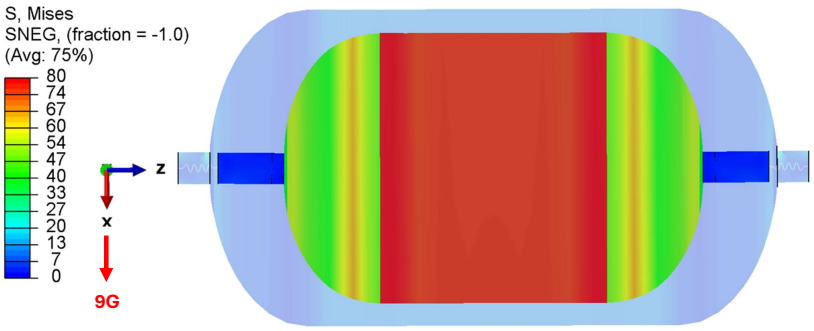

Component	Max V-M (MPa)
Inner vessel	80.3
G-10 CR rods	5.2
Outer vessel	11.8
Springs (Hand calcs)	**Torsion Stress (MPa)**
	201.6

Figure 7.11: Design 2 stress state under combined 9G forward crash load, operational pressure, and temperature conditions

Design 3: Kinematic mount

The Kevlar ropes handle the 9G loading with ease, but the inner vessel is subjected to a relatively high peak stress near the front adapter flange.

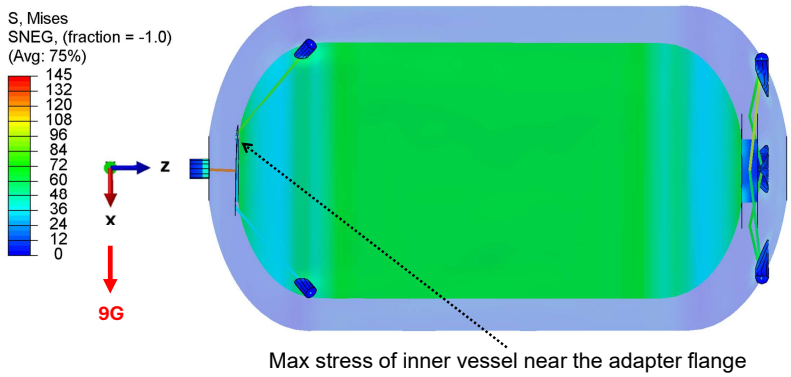

Component	Max V-M (MPa)
Inner vessel	144.5
Outer vessel	61.0
Ropes	**Max Load (N)**
Axial rope	1000
Front ropes	660
Back ropes	826

Figure 7.12: Design 3 stress state under combined 9G forward crash load, operational pressure, and temperature conditions

Design 4: Zigzagging rope

The stress concentration observed in Design 3 is no longer present in the zigzagging rope design. The inner rings and preloaded ropes ensure that the 9G loading is more or less evenly distributed along the circumference of the inner vessel domes. Hence, inner vessel's highest stress remains in the cylindrical region caused by the internal pressure and not the crash loading.

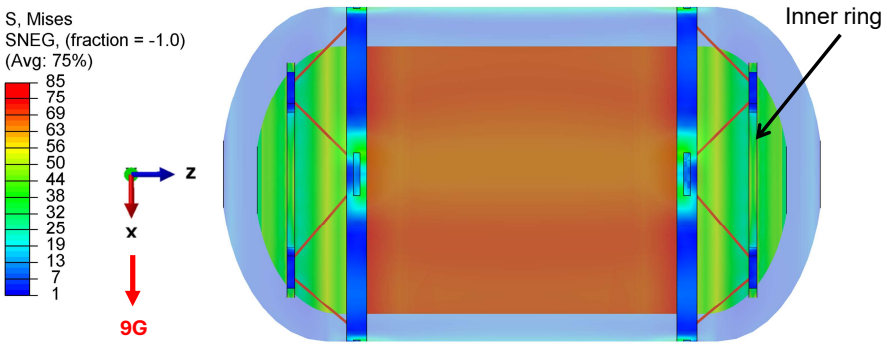

Component	Max V-M (MPa)
Inner vessel	70.7
Inner rings	85.2
Outer rings	45.2
Outer vessel	33.2
Ropes	**Max Load (N)**
	679.8

Figure 7.13: Design 4 stress state under combined 9G forward crash load, operational pressure, and temperature conditions

7.4. Heat Transfer and Time-to-Vent

Section 2.2.2 explained that any heat entering the vessel increases its internal energy, causing the liquid hydrogen to vaporize, leading to self-pressurization. Over time, this pressure buildup can reach the vent pressure set for the system, resulting in the loss of hydrogen.

AeroDelft has stipulated that hydrogen must not be vented for at least one hour after refueling to prevent exposure to hydrogen around engineers between the completion of refueling and the aircraft's start-up (**REQ-12**). To meet this requirement, a heat load of *less than* 35-40 W must enter the vessel. To promote performative designs, a maximum conductive heat transfer of 1W was imposed as a target requirement for the inner support structure, though this was specified as a "SHOULD" rather than a strict necessity (**REQ-03**).

Hence, the goal of this section is to assess the four designs based on their resistance to conductive heat transfer and the corresponding time it will take to reach the venting pressure (time-to-vent). While an in-depth thermal conduction analysis is beyond the scope of this section, it provides a preliminary calculation of the heat leakage entering the inner vessel through the different support structure concepts. As defined in Section 2.3.1, steady state conduction is given by $Q_{cond} = k \cdot A\frac{\Delta T}{L}$.

Table 7.1 summarizes the thermal conductivity values used for each design. Since conductivity varies with temperature, the average value between the two temperature extremes was used for the calculations. Table 7.2 then shows the approximate heat transfer rates in Watts for each design.

Table 7.1: Conductivity of the materials used in the proposed designs at 20K, 300K, and the average between the two.

Material	Applicable design	k (T=20 K) [W/mK]	k (T=300 K) [W/mK]	Average k [W/mK]	Source
Teflon	Design 1	0.14	0.27	0.19	[80]
G-10 CR	Design 1 & 2	0.21	0.88	0.55	[81]
Kevlar	Design 3 & 4	0.25	3.6	1.9	[68]

Table 7.2: Approximate heat transfer of each design in Watts.

Design ID	Design name	Approx. Q [W]	Considered heat path
Design 1	Discrete flexures	0.7	Through G-10 CR standoffs & Teflon flexures
Design 2	Boss suspension	2.1	Through hollow G-10 CR rod only
Design 3	Kinematic mount	0.3	Through Kevlar ropes only
Design 4	Zigzagging ropes	0.4	Through Kevlar ropes only

The conductive heat transfer values presented in Table 7.2 may either overestimate or underestimate the actual heat transfer depending on how thermal conductivity varies with temperature. Additionally, factors such as contact conductance, which introduces additional resistance to heat transfer, have not been considered. However, for the initial phase of analysis, these values are deemed adequate.

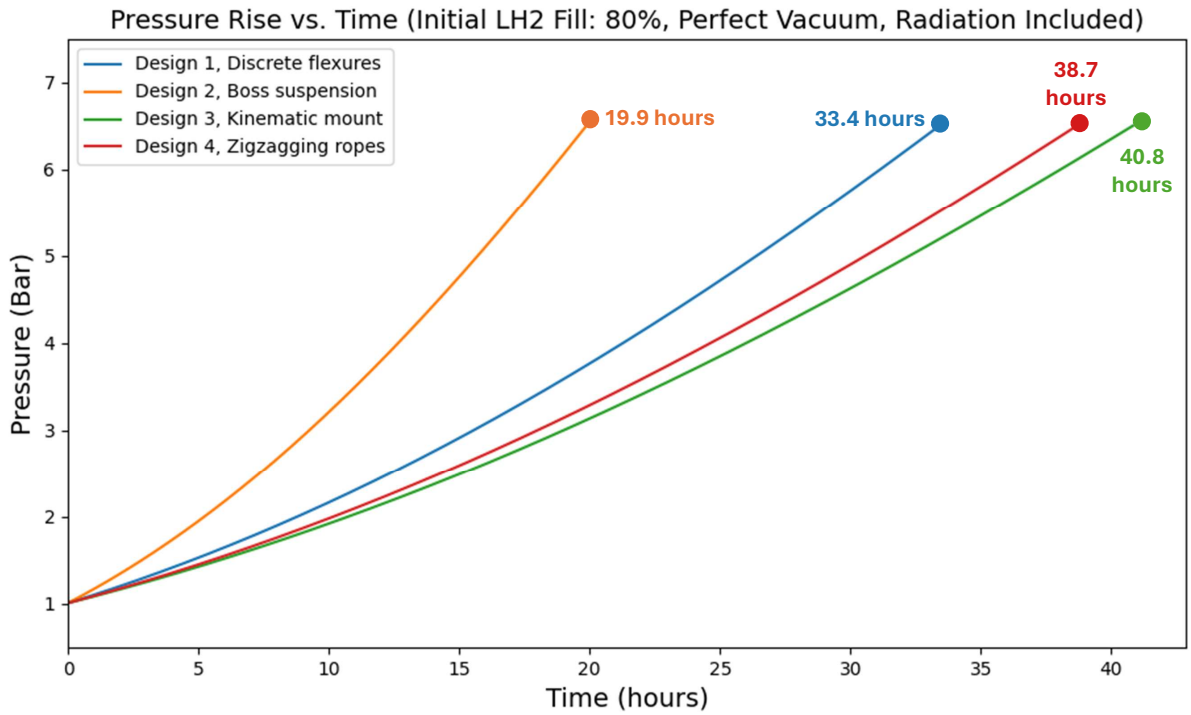

Figure 7.14: Pressure rise vs time for different designs (P_{vent} = 6.5 bar, Strat. factor = 2, inner vessel volume = 91L)

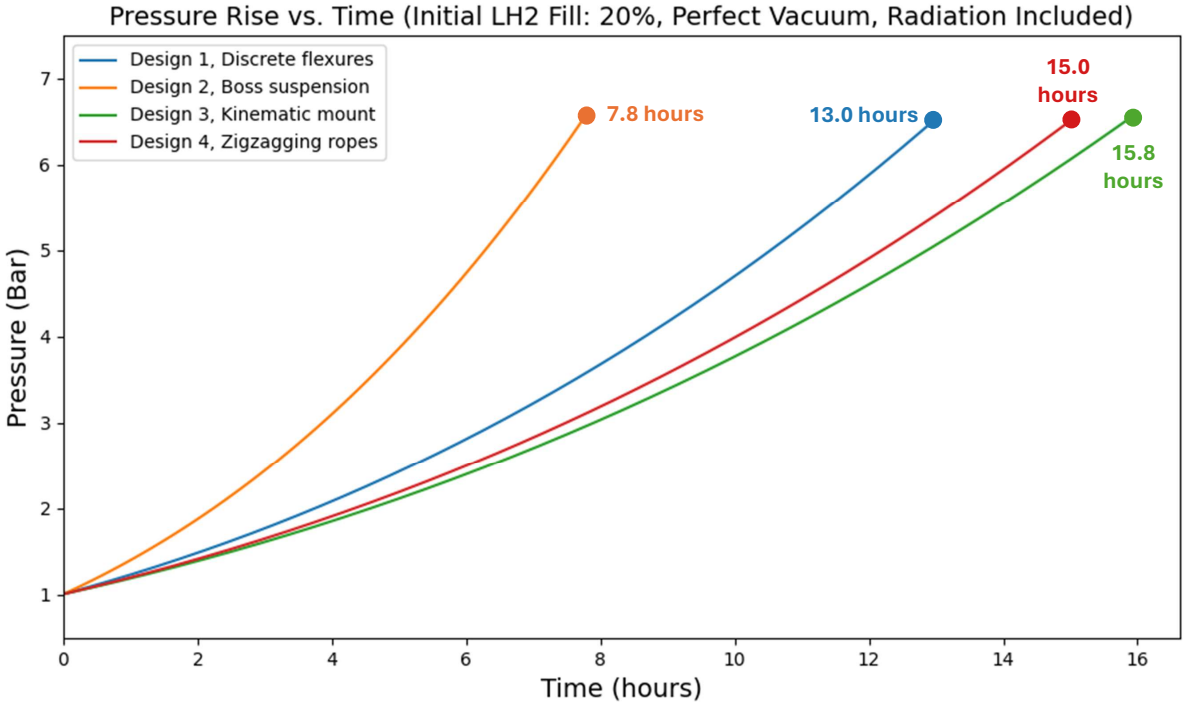

Figure 7.15: Pressure rise vs time for different designs (P_{vent} = 6.5 bar, Strat. factor = 2, inner vessel volume = 91L)

Figures 7.14 and 7.15 illustrate time-to-vent scenarios for two different initial fill rates. The 80% initial LH2 fill rate corresponds to the minimum amount of LH2 required for a given mission as per REQ-14. The 20% initial LH2 fill represents an arbitrary scenario in which some LH2 remains in the tank after a mission that did not fully consume the fuel. For both scenarios, the calculated radiation value of 1.5

W from Section 4.4.1 was added. A perfect vacuum is currently assumed, as gas conduction from H2 permeation varies over time. Finally, a stratification factor of 2 is applied in line with the discussion from Section 2.2.2.

It should be emphasized that the time-to-vent is highly influenced by the heat transfer from gas conduction in the vacuum space, as discussed in Section 2.3.2 of the literature review. The analysis in Section 4.4.2 showed that hydrogen permeation through an AS4-PEEK composite inner vessel could result in molecular gas conduction of 35 W after only 5 hours. This estimation assumes the absence of interconnected micro-cracks in the matrix. If interconnected micro-cracks were present, hydrogen leakage into the vacuum space would be much more severe, leading to even greater heat transfer and a quicker vent time. Another important consideration in this analysis is that the heat transfer from the piping is neglected. In a realistic system, the LH2 fill line, vent line, and GH2 extraction line create a thermal path between the outer vacuum shell and the inner vessel. While wrapping these pipes around the inner vessel to increase the thermal path length and adding insulation are effective strategies to reduce heat transfer, this aspect should not be overlooked in detailed design stages.

Consequently, the graphs in Figures 7.14 and 7.15 are not meant to provide precise time-to-vent values but rather to compare different support structure concepts under the main assumption of a perfect vacuum. In reality, assuming an ideal vacuum and neglecting other sources of heat leakage is both incorrect and potentially dangerous.

Given this context, the results show that the Kevlar rope designs (Design 3 and 4) have the smallest heat transfer and therefore the longest time-to-vent. This outcome is intuitive, given the substantially small cross-sectional area of the ropes. The G-10 CR standoff and Teflon flexure combination from Design 1 provide significant resistance to heat transfer. The boss suspension (Design 2) with the G10-CR rod performs well but currently does not meet the target of 1W of REQ-03. However, with design iterations—such as elongating the rod, reducing its diameter, or minimizing its thickness—it is likely that this target requirement can be achieved.

7.5. Influence of Temperature-Dependent Material Properties

As briefly mentioned, the analysis results presented in Sections 7.1 through 7.3 are based on material properties at room temperature. However, this assumption may lead to inaccuracies in the results as material properties are dependent on the temperature.

For instance, in Design 1, the Teflon flexures are known to stiffen at cryogenic temperatures (Table 5.1). From a modal analysis perspective, this increased stiffness would result in a slightly higher fundamental mode than that shown in Figure 7.1. More importantly, stiffer flexures reduce compliance under thermo-mechanical loads, which would likely increase the stress on the aluminum inner vessel beyond the current value of 19.9 MPa, as shown in Figure 7.6.

In the boss suspension of Design 2, minimal changes are expected even with temperature-dependent material properties, as the springs are located at the outer shell interface flanges and are therefore not subjected to cryogenic temperatures.

Designs 3 and 4, which utilize Kevlar ropes, are expected to exhibit changes in stiffness and tensile strength at low temperatures. Duband et al. [47] reported that the stiffness of Kevlar 29 rope increases from 29 GPa to 58 GPa, and the tensile strength increases from 1500 MPa to 1800 MPa when cooled from room temperature to 77K (-196°C). As a result, the fundamental frequency is expected to increase. However, the thermo-mechanical results of Figures 7.8 and 7.9 will remain unaffected, as the contrac-

tion of the inner vessel is accommodated regardless of the properties of the ropes, in accordance with the design intents described in Sections 5.3.2 and 5.4.2.

For the *detailed* design and analysis phase, it would be advantageous to incorporate the temperature-dependent material properties in the structural analysis. This could be done by first performing thermal simulations to get the temperature distribution throughout the structure.

7.6. Concluding Remarks

The purpose of this chapter was to analyze the four inner support structure designs and verify that, at a minimum, the functional and some operational requirements are met:

- Modal analysis was conducted to confirm compliance with functional requirement **REQ-01** and the minimum frequency operational requirement **REQ-04**.
- Thermo-mechanical analysis was used to verify that requirement **REQ-02** was satisfied and that thermal contractions are appropriately accommodated.
- The crashworthiness loading analysis ensured that requirement **REQ-09** is met and that stresses remain below their strength limits in the event of a crash.
- Finally, an analytical heat transfer analysis was performed to ensure that venting will not occur within one hour after refueling, thereby meeting requirement **REQ-12** with a caveat. Specifically, this requirement is met under the assumption that the vacuum integrity is adequately maintained. Additionally, the analysis indicated that three out of four designs currently meet operational requirement **REQ-03**, which limits conductive heat leakage through the inner support structure to 1W.

While these results confirm that the designs are viable on paper, this does not imply that all designs should be developed into prototypes. The next section will focus on evaluating and comparing the designs against performance metrics to determine their practical feasibility.

8

Evaluation and Comparison of Designs

This chapter focuses on the next step in the engineering design process shown in Figure 3.1, which is the “evaluation of the inner support structure concepts”. In contrast to the previous chapter, which focused on analyzing the concepts to ensure they were viable designs by meeting the functional requirements, this chapter compares the performance of different designs against specific metrics to determine the top-performing design(s). The four performance metrics chosen include:

1. Gravimetric efficiency
2. Heat leakage
3. Safety
4. Manufacturing and assembly feasibility

8.1. Performance Metric 1: Gravimetric Efficiency

The first performance metric considered is the effect of the inner support structures on the gravimetric efficiency. As stated in Section, 2.5.2, the equation is calculated as:

$$\eta_{grav} = \frac{m_{LH2}}{m_{LH2} + m_{ss}}$$

where:

- m_{LH2} = Mass of LH2 [kg]
- m_{ss} = Mass of the storage system including inner vessel, outer shell, and support structure [kg]

For the current scope, any auxiliary components, such as valves, sensors, and piping, are omitted in the calculation. Table 8.1 summarises the masses used to calculate the gravimetric efficiencies. Table 8.2 lists the gravimetric efficiencies for both composite constructions and aluminum constructions.

Table 8.1: List of masses used to calculate the gravimetric efficiencies

Component	Composite	Aluminum
Inner vessel mass [kg]	3.15	3.6
Outer shell mass [kg]	4.8	8.4
LH2 mass [kg]	6.2 (95% initial fill volume)	

Design ID	Approximate mass [kg]	Included components
1	0.9	Flexures, standoffs, internal brackets, bolts
2	1.1	G-10 rods, springs, interface flanges
3	1.6	Ropes, adapter flanges, external brackets
4	2.1	Ropes, rings, tensioning systems

Table 8.2: Gravimetric efficiencies of the 4 different designs for composite and aluminum vessel constructions

	Gravimetric efficiency	
Design ID	With composite vessels	With aluminum vessels
1	41.2%	32.5%
2	40.6%	32.1%
3	39.3%	31.3%
4	38.0%	30.4%

As shown by Table 8.2, the gravimetric efficiency for the composite constructions is higher. This is in large part due to the lightness of the composite outer shell. Another observation is that the gravimetric efficiency of the most lightweight design is not drastically more than the heaviest design. For example, the percent difference for gravimetric efficiencies between design 1 and 4 is only 6.67%.

To provide scores to the different designs, a proportional scoring method is used with a baseline of 7. This is to prevent having the heaviest design from getting unfairly penalized. In addition, this method ensures that the resulting scores for either composite or aluminum constructions will be identical. The equation is as follows:

$$\text{Gravimetric Score} = \text{Baseline} + (10 - \text{Baseline}) \times \frac{(\text{Gravimetric Efficiency} - \text{Minimum Efficiency})}{(\text{Maximum Efficiency} - \text{Minimum Efficiency})} \quad (8.1)$$

Table 8.3 below shows the resulting gravimetric efficiency scores as calculated with Equation 8.1. The discrete flexures design has the lightest construction, with the boss suspension being a close second. The designs incorporating ropes are the heaviest due to the additional components required for attaching the ropes. As illustrated in Section 5.4.3, the outer rings of the zigzagging rope design allow for a thinner and therefore lighter outer *aluminum* shell. However, since this benefit is currently observed only for aluminum and not with a quasi-isotropic composite, it was not factored into the gravimetric efficiency score.

Table 8.3: Gravimetric efficiency scores for the four designs

Design ID	Design name	Gravimetric efficiency score
1	Discrete flexures	10.0
2	Boss suspension	9.4
3	Kinematic mount	8.2
4	Zigzagging ropes	7.0

8.2. Performance Metric 2: Heat Leakage

The next performance metric used to evaluate the designs is the amount of heat leakage they allow to enter the tank. Naturally, lower thermal leakage corresponds to a higher performance score, as minimizing heat transfer is crucial for increasing the time before venting.

Table 7.2 presented the approximate heat transfer values for the four designs: 0.7W, 2.1W, 0.3W, and 0.4W, respectively. Although design 2 has the highest thermal leakage at 2.1W, this value is still low and within acceptable limits for the current design case. The operational requirement REQ-03 specifying a minimum heat leakage of 1W is currently considered a ”SHOULD” rather than a ”SHALL,” indicating that while it is a desirable target, it is not an absolute necessity.

For a similar reason as the gravimetric efficiency metric, a proportional scoring method above a baseline is used. This approach prevents Design 2, with its acceptable leakage of 2.1W, from being unfairly penalized. The scoring equation used for this criterion is as follows:

$$\text{Heat-Leakage Score} = \text{Baseline} + (10 - \text{Baseline}) \times \frac{(\text{Maximum Leakage} - \text{Thermal Leakage})}{(\text{Maximum Leakage} - \text{Minimum Leakage})} \quad (8.2)$$

Where the *baseline is chosen to be 5*. In other words, the least performing design will be given a 5.

Table 8.4 is the summary of the heat-leakage scores for each design. The two most thermally efficient designs are those that make use of ropes. As stated in Section 7.4, the boss suspension has the potential to reduce its thermal leakage with some design iterations, but it is unlikely to ever perform better than the rope designs.

Table 8.4: Heat-leakage scores for the four designs

Design ID	Design name	Heat leakage score
1	Discrete flexures	8.9
2	Boss suspension	5.0
3	Kinematic mount	10.0
4	Zigzagging ropes	9.7

8.3. Performance Metric 3: Safety

This section evaluates the safety of each design using a probability-consequence risk matrix, as shown by Table 8.5. For each design, a potential event is identified, along with its associated risk level, an explanation of the assigned score, and possible mitigation strategies.

Table 8.5: Probability-consequence matrix used to evaluate the safety of each designs

		Consequence			
		1	2	3	4
Probability		Minor	Moderate	Major	Critical
4	High	4	8	12	16
3	Moderate	3	6	9	12
2	Low	2	4	6	8
1	Rare	1	2	3	4

Since the goal is to provide the safest designs with the highest scores, the scoring method is inverted and linearized with the following equation:

$$\text{Safety Score} = \text{Max Safety Score} - k \times (\text{Risk Level} - 1) \tag{8.3}$$

Where,

- Max Safety Score = 10
- k = 0.6667 = Decrement factor (i.e. the slope)
- Risk level

Therefore, a risk level of 16 corresponds to a safety score of 0, and a risk level of 1 corresponds to a safety score of 10.

Design 1: Discrete flexures

Potential event: Damage or failure of a flexure during operational conditions caused by excessively cold temperatures and load cycles.

Risk level: Probability (Moderate-3) x Consequence (Moderate-2) = Risk Level 6

Explanation: The loss of Teflon's ductility at cryogenic temperatures can lead to material failure. However, analyses have shown that the strains during operation and crash events remain below the material's failure strain, even at low temperatures. The current design incorporates 8 flexures. Even if one or two flexures are damaged, the remaining flexures can still support the inner vessel, allowing the flight to continue without requiring an emergency landing.

Mitigation: Section 5.1.3 previously discussed a potential mitigation strategy to counteract the effects of cryogenic temperatures using 5mm G-10 standoffs. Figure 8.1 below, which is a repeat of Figure 5.3, illustrates how these standoffs can prevent a portion of the flexures from dropping to -250°C. Additionally, the bracket design can be modified, and the standoff thickness can be increased from 5mm to 10mm or 15mm, ensuring that the Teflon flexure does not fall below its glass transition temperature of -103°C. With these mitigations in place, the probability can be reduced to a Low-2, resulting in a new risk level of 4.

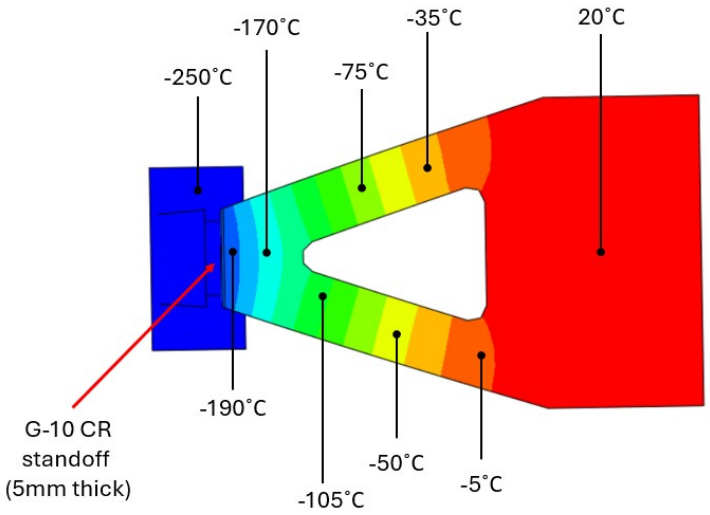

Figure 8.1: Mitigation strategy for the discrete flexure design (previously shown in Figure 5.3)

Design 2: Boss suspension

Potential event: Damage to G-10 rods.

Risk level: Probability (Rare-1) x Consequence (Moderate-2) = Risk Level 2

Explanation: The G-10 rods are primarily subjected to compressive loads, which are well within their cryogenic strength limits. The rod-spring suspension system is designed to be robust. Even if minor cracking or surface damage occurs to the G-10 rods, it would likely not compromise the functionality of the inner support structure.

Mitigation: The boss suspension currently has an acceptable level of risk and therefore mitigation strategies are not considered.

Design 3: Kinematic mount

Potential event: Failure of a rope at a termination.

Risk level: Probability (Moderate-3) x Consequence (Major-3) = Risk Level 9

Explanation: The kinematic mount uses many ropes (five in the front and three in the back) each with their own terminations. Even if high workmanship is guaranteed, there are numerous potential failure points. The failure of one rope would compromise the proper functionality of the inner support structure, and adding redundancy is not evident.

Mitigation: There is currently no mitigation strategy considered for this suspension system.

Design 4: Zigzagging ropes

Potential event: Failure of a rope at a termination or due to damage from bends.

Risk level: Probability (Low-2) x Consequence (Major-3) = Risk Level 6

Explanation: Many mitigation strategies have already been considered to lessen the likelihood of such failures, as detailed in Section 5.4.3. However, the design currently lacks redundancy, which contributes to a Major-3 consequence for a similar reason described for Design 3.

Mitigation: Redundancy can come in the form shown by Figure 8.2, by having two sets of ropes with their own anchor and tensioning systems. Hence, in the event of a rope failure, the consequence would be reduced to a Minor-1 since the inner vessel is still supported with sufficient stiffness. With this implemented, there is a new risk level of 2.

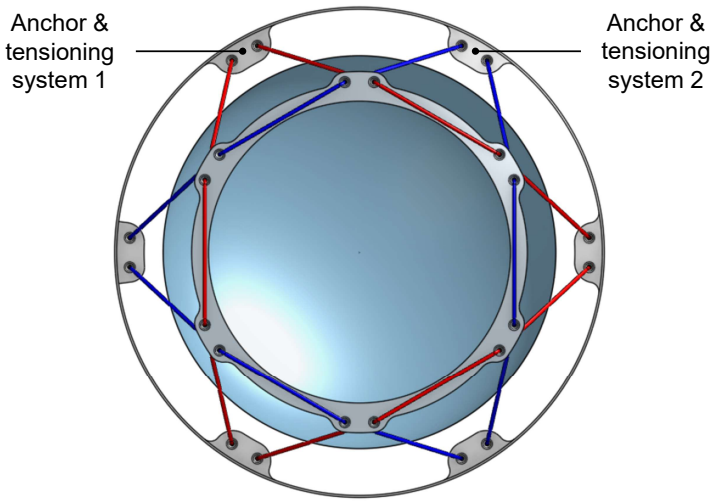

Figure 8.2: Adding redundancy to the zigzagging rope design

Table 8.6 summarizes the safety scores of the four designs before and after implementing mitigation, if applicable. The two safest designs are the Boss Suspension and the Zigzagging Ropes with added redundancy.

Table 8.6: Safety scores for the four designs

Design ID	Design name	Safety score (pre-mitigation)	Safety score (post-mitigation)
1	Discrete flexures	6.7	8.0
2	Boss suspension	9.3	9.3
3	Kinematic mount	4.6	4.6
4	Zigzagging ropes	6.7	9.3

8.4. Performance Metric 4: Manufacturing/Assembly Feasibility

To comprehensively evaluate the manufacturing and assembly feasibility of each design, a scoring system is used that considers three equally weighted factors:

Number of components: Assesses the simplicity of the design since fewer components likely lead to an easier and quicker assembly.

Component complexity and manufacturing feasibility: This factor evaluates both the intricacy of individual parts and the ease with which they can be manufactured. Designs that use off-the-shelf components, such as standard springs or fasteners, are favored, as they reduce the need for custom fabrication and simplify the assembly process. Additionally, designs that can be easily machined or produced using standard manufacturing techniques score higher.

Assembly difficulty: Takes into account the practical challenges involved in putting the design together, with higher scores awarded to designs that can be assembled with minimal effort, standard tools, and without the need for precise alignment or specialized jigs.

Tables 8.7 to 8.9 show the scoring summary for the three considered factors. A brief explanation is also included to support the given scores.

Table 8.7: Scoring Summary for number of components factor

Factor: Number of components		
Design ID	**Score**	**Main components considered**
1	4	Eight flexures each with their own brackets, bolts and standoffs.
2	9	Two sets of G-10 rods and springs.
3	2	Eight ropes, adapter flanges, numerous external brackets each with their own bolts used for tensioning.
4	7	Two sets of ropes, inner and outer rings, and tensioning systems.

Table 8.8: Scoring Summary for the component complexity and manufacturing feasibility factor

Factor: Component complexity and manufacturing feasibility		
Design ID	**Score**	**Main considerations**
1	7	Individual components can be machined using conventional methods.
2	10	Standard springs are used, G-10 rods can be machined easily with a lathe.
3	4	Adapter flanges likely require many machining operations.
4	7	Rings are not complex, but require a few machining operations. Ropes and tensioning system are made from standard parts.

Table 8.9: Scoring Summary for the assembly difficulty factor

Factor: Assembly difficulty		
Design ID	**Score**	**Main considerations**
1	4	Jigs required. Correct assembly of the 8 flexures involves meticulous work.
2	9	Relatively easy assembly. A jig or support may be need to compress the springs during assembly.
3	2	Assembly is cumbersome. Extensive jigs required to assemble the external brackets.
4	6	Jigs required to support the rings while tensioning and assembly.

Finally, Table 8.10 summarizes the scores from the three equally weighted factors considered. The boss suspension is deemed the easiest to manufacture and assemble, mainly due to its design simplicity.

Table 8.10: Manufacturing and assembly scores for the four designs

Design ID	Design name	Manufacturing and assembly feasibility score
1	Discrete flexures	5.0
2	Boss suspension	9.3
3	Kinematic mount	2.7
4	Zigzagging ropes	6.7

8.5. Total Scores and Sensitivity Studies

The score summary for all four designs are shown in Table 8.11 below.

Table 8.11: Summary of the four performance criteria scores for each design

Design ID	Design name	Grav. eff.	Heat leak	Safety (post-mit.)	M&A feasibility	Total score (/40)
1	Discrete flexures	10.0	8.9	8.0	5.0	31.9
2	Boss suspension	9.4	5.0	9.3	9.3	33.0
3	Kinematic mount	8.2	10.0	4.6	2.7	25.5
4	Zigzagging ropes	7.0	9.7	9.3	6.7	32.7

Considering an equal weight of 25% for each of the criteria yields the following results:

Winning design: The boss suspension with a score of 8.3.

Second place design: The zigzagging ropes with a score of 8.2.

Third place design: The discrete flexures with a score of 8.0.

Fourth place design: The kinematic mount with a score of 6.4.

In most practical cases, engineers rarely assign equal weightings to all criteria. To explore the impact of different weightings on the winning design, a sensitivity study was conducted. This study included scenarios where two of the four criteria were each assigned a weight of 0.40, while the other two were given a weight of 0.10. This approach represents situations where engineers aim to prioritize two specific factors over the others. Additionally, the impact of prioritizing a single criterion with a weight of 0.70, while assigning the remaining three criteria weights of 0.10 each, was also examined. The results are presented in Table 8.12.

Table 8.12: Impact of varying weights on the selection of the winning design

Case	Grav.	Heat	Safety	M&A	Winner	Score	Second	Score
0	0.25	0.25	0.25	0.25	Boss	8.3	Zigzag	8.2
1	0.4	0.4	0.1	0.1	Flexure	8.9	Zigzag	8.3
2	0.4	0.1	0.4	0.1	Boss	8.9	Flexure	8.6
3	0.4	0.1	0.1	0.4	Boss	8.9	Flexure	7.7
4	0.1	0.4	0.4	0.1	Zigzag	9.0	Flexure	8.3
5	0.1	0.4	0.1	0.4	Zigzag	8.2	Boss	7.6
6	0.1	0.1	0.4	0.4	Boss	8.9	Zigzag	8.1
7	0.7	0.1	0.1	0.1	Flexure	9.2	Boss	8.9
8	0.1	0.7	0.1	0.1	Zigzag	9.1	Kinematic	8.6
9	0.1	0.1	0.7	0.1	Boss/Zigzag	8.9	-	-
10	0.1	0.1	0.1	0.7	Boss	8.9	Zigzag	7.3

8.6. Concluding Remarks

This chapter evaluated the four inner support structure designs against four performance metrics: gravimetric efficiency, heat leakage prevention, safety, and manufacturing and assembly feasibility. Based on the tabulated results in Table 8.12, the following conclusions can be drawn:

- The **boss suspension (Design 2)** is recommended in six out of the eleven cases. It excels in situations that prioritize a combination of safety, high gravimetric efficiency, and ease of manufacturing and assembly.
- The **zigzagging ropes (Design 4)** design is recommended in four out of the eleven cases. It nearly tied with the boss suspension under equal weighting conditions. For scenarios where low heat leakage is critical without compromising safety, the zigzagging ropes design is an optimal choice.
- The **discrete flexure (Design 1)** design performed best when gravimetric efficiency and heat leakage were prioritized. It ranked second in several scenarios, indicating that it is a performative design. However, its lower scores in safety and manufacturing and assembly limit its overall ranking compared to other designs.
- The **kinematic mount (Design 3)** design, however, was not effective in most cases, showing it to be weaker compared to the alternatives. Therefore, it is not recommended for further pursuit.

9

Conclusion

The goal of this thesis was to design effective internal support structures for double-walled liquid hydrogen (LH2) vessels for aircraft use. This research was grounded in a practical application through a collaboration with the AeroDelft team, who are adapting a Sling 4 aircraft for hydrogen-powered electric propulsion. As part of their next milestone for the Phoenix project, AeroDelft aims to store 6 kg of LH2 to meet their mission requirements, which necessitates the design of a double-walled vessel. Given the importance of the internal support structure in such a vessel, this thesis focused on addressing the following main research question:

> **What design methodology would facilitate the development of effective inner support structures for a double-walled vessel used in a small liquid hydrogen-powered aircraft?**

To begin, functional, operational, and constraint requirements were established to define the boundary conditions for the designs. A baseline design for the inner vessel and outer shell was then developed based on AeroDelft's specifications, recognizing that the inner support structure interfaces with both components. Therefore, it was essential not to treat these components as isolated "black box" entities.

Subsequently, four distinct concepts for the internal support structure were introduced. Each concept emphasized specific design intentions and important considerations. These designs were either inspired by different engineering applications, modified and built upon existing solutions, or were built on fundamental engineering principles.

The concepts were analyzed in terms of modal, thermo-mechanical, crash loads, and heat leakage to assess their viability and ability to meet the basic functional requirements of an internal support structure. To identify the most optimal design(s), the concepts were evaluated and compared based on key performance metrics: gravimetric efficiency, heat leakage, safety, and feasibility of manufacturing and assembly. The results indicated that the **boss suspension** design emerged as the best option, offering safety, ease of manufacturing and assembly, and adequate thermal insulation for AeroDelft's needs. However, the **zigzagging ropes** design also proved highly effective in scenarios where minimizing heat leakage is critical, without compromising safety. The **discrete flexures** design was identified as an optimal choice when both gravimetric efficiency and thermal insulation are priorities. Finally, while the **kinematic mount** design was viable in theory, it was found to be less effective for AeroDelft's application due to its large component count and the complexity of assembly.

10

Looking ahead and Future Recommendations

Referring to Figure 3.1 in the methodology section, the scope of this thesis concluded with the “Evaluation of Inner Support Structure Concepts”. The logical next step is to further develop the chosen inner support structure design(s), paving the way for a prototype build.

In parallel with this development, it would be beneficial to collaborate with the designers of the propellant feed systems. For double-walled vessels of this size, the piping that connects to and from the tank often wraps around the inner vessel to increasing the thermal path. Understanding the space taken by this piping can help optimize the dimensions of both the inner vessel and the support structure, potentially enhancing gravimetric efficiency and thermal resistance. For instance, in the case of the boss suspension design, increasing the radius of the inner vessel and reducing its length could be advantageous. This adjustment would lengthen the G-10 rods, thereby improving their resistance to heat transfer. For the zigzagging rope design, enlarging the inner vessel would result in longer ropes with more shallow angles. For the discrete flexure design, the length of the inner vessel can be extended to store a greater volume of LH2. As the design of the double-walled vessel progresses, there is an opportunity to refine the inner support structure(s) further.

Additionally, it is recommended to conduct standalone tests on the selected support structure design(s). For instance, a test jig could be constructed for the zigzagging rope design to apply tension and evaluate the limits of the anchor and tensioning system (Figure 5.8). If the discrete flexure design is further developed, cyclic testing of Teflon flexures at cryogenic temperatures could provide valuable insights into their durability under such conditions. Additionally, heat transfer tests on the flexure/G-10 standoff combination, shown in Figure 5.3, could assess the standoff’s effectiveness in preventing the Teflon flexure from dropping below its glass transition temperature. These component-level tests are essential for validating the proposed designs and ensuring their safety and performance once in operation.

References

[1] *Dawn, Com&Sens and ESA partner on smart composite overwrapped pressure vessels for space*. URL: https://www.dawnaerospace.com/latest-news/smartcopvs (visited on 09/14/2024).

[2] T. Yusaf et al. "Sustainable hydrogen energy in aviation – A narrative review". en. In: *International Journal of Hydrogen Energy* 52 (Jan. 2024), pp. 1026–1045. ISSN: 03603199. DOI: 10.1016/j.ijhydene.2023.02.086. URL: https://linkinghub.elsevier.com/retrieve/pii/S0360319923009187 (visited on 08/20/2024).

[3] E.J. Adler and J.R.R.A. Martins. "Hydrogen-powered aircraft: Fundamental concepts, key technologies, and environmental impacts". en. In: *Progress in Aerospace Sciences* 141.100922 (Aug. 2023). DOI: 10.1016/j.paerosci.2023.100922.

[4] K.T. Møller et al. "Hydrogen - A sustainable energy carrier". en. In: *Progress in Natural Science: Materials International* 27.1 (Feb. 2017), pp. 34–40. ISSN: 10020071. DOI: 10.1016/j.pnsc.2016.12.014. URL: https://linkinghub.elsevier.com/retrieve/pii/S1002007116303240 (visited on 08/20/2024).

[5] J.W. Sheffield, K.B. Martin, and R. Folkson. "Electricity and hydrogen as energy vectors for transportation vehicles". en. In: *Alternative Fuels and Advanced Vehicle Technologies for Improved Environmental Performance*. Elsevier, 2014, pp. 117–137. ISBN: 978-0-85709-522-0. DOI: 10.1533/9780857097422.1.117. URL: https://linkinghub.elsevier.com/retrieve/pii/B9780857095220500054 (visited on 08/20/2024).

[6] A. Goldmann et al. "A Study on Electrofuels in Aviation". en. In: *Energies* 11.2 (Feb. 2018), p. 392. ISSN: 1996-1073. DOI: 10.3390/en11020392. URL: https://www.mdpi.com/1996-1073/11/2/392 (visited on 08/20/2024).

[7] *AeroDelft: Our future flies in clean skies*. URL: https://aerodelft.nl/ (visited on 09/02/2024).

[8] A. Huber. "Air-coupled Ultrasonic Inspection of Thermoplastic Composite Structures for Aerospace Vehicles". en. In: *Research and Review Journal of Nondestructive Testing* 1.1 (Aug. 2023). ISSN: 2941-4989. DOI: 10.58286/28105. URL: https://www.ndt.net/search/docs.php3?id=28105 (visited on 09/13/2024).

[9] M. Nachtane et al. "An Overview of the Recent Advances in Composite Materials and Artificial Intelligence for Hydrogen Storage Vessels Design". en. In: *Journal of Composites Science* 7.3 (Mar. 2023). Number: 3 Publisher: Multidisciplinary Digital Publishing Institute, p. 119. ISSN: 2504-477X. DOI: 10.3390/jcs7030119. URL: https://www.mdpi.com/2504-477X/7/3/119.

[10] H. Reynolds. "Pressure Vessel Design, Fabrication, Analysis, and Testing". en. In: *Composite Filament Winding*. Ed. by S.T. Peters. ASM International, Sept. 2011, pp. 115–148. DOI: 10.31399/asm.tb.cfw.t52860115.

[11] S.T. Peters, ed. *Composite Filament Winding*. ASM International, Sept. 2011. ISBN: 978-1-62708-338-6. DOI: 10.31399/asm.tb.cfw.9781627083386. URL: https://doi.org/10.31399/asm.tb.cfw.9781627083386 (visited on 01/11/2024).

[12] M. W. Hyer. *Stress Analysis of Fiber-Reinforced Composite Materials*. The McGraw-Hill Companies Inc., 1998.

[13] Z. Gürdal, S. IJsselmuiden, and J. Van Campen. “Composite Laminate Optimization with Discrete Variables”. en. In: *Encyclopedia of Aerospace Engineering*. Ed. by Richard Blockley and Wei Shyy. 1st ed. Wiley, Sept. 2010. ISBN: 978-0-470-75440-5 978-0-470-68665-2. DOI: 10.1002/9780470686652.eae499. URL: https://onlinelibrary.wiley.com/doi/10.1002/9780470686652.eae499 (visited on 11/07/2023).

[14] R.S. Khurmi and J.K. Gupta. *A textbook of machine design*. 14th ed. New Delhi: Eurasia Publishing House, 2015.

[15] M. Xia, K. Kemmochi, and H. Takayanagi. “Analysis of filament-wound fiber-reinforced sandwich pipe under combined internal pressure and thermomechanical loading”. en. In: *Composite Structures* (2001).

[16] V. K. Poorte et al. “Structural integration of a full-composite, double-walled, vacuum-insulated, cryo-compressed tank for the Flying V: a numerical study”. en. In: *Proceedings of the AIAA SCITECH 2024 Forum* (2024). Publisher: American Institute of Aeronautics and Astronautics Inc. (AIAA). DOI: 10.2514/6.2024-0834. URL: https://repository.tudelft.nl/islandora/object/uuid%3A2539af15-70fa-4876-9540-316a12771776 (visited on 01/24/2024).

[17] R.P. Reed and M. Golda. “Cryogenic properties of unidirectional composites”. en. In: *Cryogenics* 34.11 (Jan. 1994), pp. 909–928. ISSN: 00112275. DOI: 10.1016/0011-2275(94)90077-9. URL: https://linkinghub.elsevier.com/retrieve/pii/0011227594900779 (visited on 04/13/2024).

[18] Z. Sápi and R. Butler. “Properties of cryogenic and low temperature composite materials – A review”. In: *Cryogenics* 111 (Oct. 2020), p. 103190. ISSN: 0011-2275. DOI: 10.1016/j.cryogenics.2020.103190. URL: https://www.sciencedirect.com/science/article/pii/S0011227520301922 (visited on 11/22/2023).

[19] I. Katsivalis et al. “Hydrogen permeability of thin-ply composites after mechanical loading”. en. In: *Composites Part A: Applied Science and Manufacturing* 176 (Jan. 2024), p. 107867. ISSN: 1359835X. DOI: 10.1016/j.compositesa.2023.107867. URL: https://linkinghub.elsevier.com/retrieve/pii/S1359835X23004438 (visited on 06/07/2024).

[20] M. Flanagan et al. “Permeability of carbon fibre PEEK composites for cryogenic storage tanks of future space launchers”. en. In: *Composites Part A: Applied Science and Manufacturing* 101 (Oct. 2017), pp. 173–184. ISSN: 1359835X. DOI: 10.1016/j.compositesa.2017.06.013. URL: https://linkinghub.elsevier.com/retrieve/pii/S1359835X17302403 (visited on 06/07/2024).

[21] W. D. Callister and D. G. Rethwisch. “Polymer Structures”. In: *Materials Science and Engineering, An Introduction*. 9th ed. John Wiley & Sons, Inc., 2014, pp. 545–579.

[22] J.B. Schutz. “Properties of composite materials for cryogenic applications”. en. In: *Cryogenics* 38.1 (Jan. 1998), pp. 3–12. ISSN: 00112275. DOI: 10.1016/S0011-2275(97)00102-1. URL: https://linkinghub.elsevier.com/retrieve/pii/S0011227597001021 (visited on 04/26/2024).

[23] R.K. Ahluwalia and J.K. Peng. “Dynamics of cryogenic hydrogen storage in insulated pressure vessels for automotive applications”. en. In: *International Journal of Hydrogen Energy* 33.17 (Sept. 2008), pp. 4622–4633. ISSN: 03603199. DOI: 10.1016/j.ijhydene.2008.05.090. URL: https://linkinghub.elsevier.com/retrieve/pii/S0360319908006708 (visited on 03/22/2024).

[24] E. D. M. Ramos. “Enabling Conceptual Design and Analysis of Cryogenic In-Space Vehicles Through the Development of an Extensible Boil-Off Model”. PhD thesis. Georgia Institute of Technology, 2021.

[25] N.T. Van Dresar, C.S. Lin, and M.M. Hasan. “Self-Pressurization of a Flightweight Liquid Hydrogen Tank: Effects of Fill Level at Low Wall Heat Flux”. en. In: (1992).

[26] D. Verstraete. “The Potential of Liquid Hydrogen for long range aircraft propulsion”. en. In: (Apr. 2009). Accepted: 2010-01-04T14:28:34Z Publisher: Cranfield University. URL: https://dspace.lib.cranfield.ac.uk/handle/1826/4089 (visited on 02/29/2024).

[27] C. S. Lin, N. T. Van Dresar, and M. Hasan. “Pressure Control Analysis of Cryogenic Storage Systems”. en. In: *Journal of Propulsion and Power* 20.3 (May 2004), pp. 480–485. ISSN: 0748-4658, 1533-3876. DOI: 10.2514/1.10387. URL: https://arc.aiaa.org/doi/10.2514/1.10387 (visited on 03/05/2024).

[28] G. Onorato, P. Proesmans, and M. F. M. Hoogreef. “Assessment of hydrogen transport aircraft: Effects of fuel tank integration”. en. In: *CEAS Aeronautical Journal* 13.4 (Oct. 2022), pp. 813–845. ISSN: 1869-5582, 1869-5590. DOI: 10.1007/s13272-022-00601-6. URL: https://link.springer.com/10.1007/s13272-022-00601-6 (visited on 11/16/2023).

[29] K. Breisacher and J. Moder. “Computational Fluid Dynamics (CFD) Simulations of Jet Mixing in Tanks of Different Scales”. en. In: *Computational Fluid Dynamics* (2010).

[30] T. L. Bergman and F. P. Incropera, eds. *Fundamentals of heat and mass transfer*. en. 7th ed. Hoboken, NJ: Wiley, 2011. ISBN: 978-0-470-50197-9.

[31] Y. A. Çengel and A. J. Ghajar. *Heat and mass transfer: fundamentals & applications*. en. 5th edition. New York, NY: McGraw-Hill Education, 2015. ISBN: 978-0-07-339818-1.

[32] J.A. Clark and M. E. Korybalski. “Algebraic methods for the calculation of radiation exchange in an enclosure”. en. In: *Wärme- und Stoffübertragung* 7.1 (Mar. 1974), pp. 31–44. ISSN: 0042-9929. DOI: 10.1007/BF01438318. URL: http://link.springer.com/10.1007/BF01438318 (visited on 04/09/2024).

[33] T. M. Flynn. *Cryogenic engineering*. en. 2nd ed., rev. and expanded. New York: Marcel Dekker, 2005. ISBN: 978-0-8247-5367-2.

[34] M. Donabedian et al. “Insulation”. In: *Spacecraft Thermal Control Handbook*. 2nd Edition. Vol. Volume 1 - Fundamental Technologies. American Institute of Aeronautics and Astronautics/Aerospace Press (AIAA), 2002.

[35] A. Roth. *Vacuum Technology Part I*. Oct. 1972.

[36] R.J. Corrucini. “Gaseous heat conduction at low pressures and temperatures”. In: Vol. VII & VIII (1959). DOI: https://doi.org/10.1016/0042-207X(59)90766-3.

[37] E. T. Malroy. “Free Molecular Heat Transfer Programs for Setup and Dynamic Updating the Conductors in Thermal Desktop”. en. In: (2007).

[38] T. P. Sarafin and W. J. Larson. *Spacecraft Structures and Mechanisms: From Concept to Launch*. Microcosm, Inc. & Kluwer Academic Publishers, 1995. ISBN: 978-0-7923-3476-7.

[39] E21 Committee. *Test Method for Total Mass Loss and Collected Volatile Condensable Materials from Outgassing in a Vacuum Environment*. en. 2021. DOI: 10.1520/E0595-15R21. URL: http://www.astm.org/cgi-bin/resolver.cgi?E595-15R21 (visited on 04/10/2024).

[40] R. Pastore et al. “Outgassing effect in polymeric composites exposed to space environment thermal-vacuum conditions”. en. In: *Acta Astronautica* 170 (May 2020), pp. 466–471. ISSN: 00945765. DOI: 10.1016/j.actaastro.2020.02.019. URL: https://linkinghub.elsevier.com/retrieve/pii/S0094576520300813 (visited on 04/10/2024).

[41] R. Ahluwalia et al. “Onboard Liquid Hydrogen Storage for Long Haul Trucks”. en. In: (2022). URL: https://www.energy.gov/sites/default/files/2022-03/Liquid%20H2%20Workshop-ANL2.pdf (visited on 09/16/2024).

[42] . *How to store liquid hydrogen for zero-emission flight*. Dec. 2021. URL: https://www.airbus.com/en/newsroom/news/2021-12-how-to-store-liquid-hydrogen-for-zero-emission-flight.

[43] A. W. Raymond and J. Reiter. “Modeling and testing of cryo-adsorbent hydrogen storage tanks with improved thermal isolation”. In: *AIP Conference Proceedings* 1434.1 (June 2012), pp. 765–772. ISSN: 0094-243X. DOI: 10.1063/1.4706989. URL: https://doi.org/10.1063/1.4706989 (visited on 11/22/2023).

[44] *Kevlar® Aramid Fiber Technical Guide*. en. 2017. URL: https://www.dupont.com/content/dam/dupont/amer/us/en/safety/public/documents/en/Kevlar_Technical_Guide_0319.pdf.

[45] *Kevlar Supports for Cryogenic Vessels*. en. 2022. URL: https://www.mtm-inc.com/kevlar-supports-for-cryogenic-vessels.html (visited on 11/27/2023).

[46] G.M. Voellme et al. “A Cryogenic, Insulating Suspension System for the High resolution Airborne Wideband Camera (HAWC) and Submillemeter And Far Infrared Experiment (SAFIRE) Adiabatic Demagnetization Refrigerators (ADRs)”. en. In: (2002).

[47] L. Duband, L. Hui, and A. Lange. “Thermal isolation of large loads at low temperature using Kevlar rope”. In: *Cryogenics* 33.6 (June 1993), pp. 643–647. ISSN: 0011-2275. DOI: 10.1016/0011-2275(93)90124-7. URL: https://www.sciencedirect.com/science/article/pii/0011227593901247 (visited on 11/23/2023).

[48] E. Lisowski, W. Czyżycki, and K. Łazarczyk. “Simulation and experimental research of internal supports in mobile cryogenic tanks”. In: (Jan. 2010).

[49] W. Czyżycki. “Modeling of Heat Flow Through Multilayer Internal Supports of Cryogenic Vessels”. en. In: (2015).

[50] V. Norouzifard, S.M. Hosseini, and E. Alizadeh. “Investigating the effect of metal-polymer internal support on reducing the heat transfer rate of mobile cryogenic vessels”. en. In: *Heat and Mass Transfer* 57.2 (Feb. 2021), pp. 269–282. ISSN: 1432-1181. DOI: 10.1007/s00231-020-02950-6. URL: https://doi.org/10.1007/s00231-020-02950-6 (visited on 11/10/2023).

[51] G. Tzoumakis, K. Fotopoulos, and G. Lampeas. “Multi-Physics Digital Model of an Aluminum 2219 Liquid Hydrogen Aircraft Tank”. en. In: *Aerospace* 11.2 (Feb. 2024), p. 161. ISSN: 2226-4310. DOI: 10.3390/aerospace11020161. URL: https://www.mdpi.com/2226-4310/11/2/161 (visited on 03/22/2024).

[52] B. Nitin, P. Sandilya, and G. Chakraborty. “Optimal design of a helical coil support for dewars in fuel cell applications”. en. In: *Environmental Science and Pollution Research* 30.10 (Feb. 2023), pp. 24963–24974. ISSN: 1614-7499. DOI: 10.1007/s11356-022-20286-y. URL: https://doi.org/10.1007/s11356-022-20286-y (visited on 02/04/2024).

[53] *Thermally Insulating, Kinematic Tensioned-Fiber Suspension*. Oct. 2004. URL: https://www.techbriefs.com/component/content/article/674-gsc-14743 (visited on 04/11/2024).

[54] P. Kittel. “Comparison of Dewar supports for space applications”. en. In: *Cryogenics* 33.4 (Apr. 1993), pp. 429–434. ISSN: 00112275. DOI: 10.1016/0011-2275(93)90172-K. URL: https://linkinghub.elsevier.com/retrieve/pii/001122759390172K (visited on 04/15/2024).

[55] H. Cease et al. “Measurement of mechanical properties of three epoxy adhesives at cryogenic temperatures for CCD construction”. en. In: (2006).

[56] Y. Haik and T. M. M. Shahin. *Engineering design process*. en. 2nd ed. OCLC: ocn681714557. Stamford, CT: Cengage Learning, 2011. ISBN: 978-0-495-66814-5.

[57] *NASA Systems Engineering Handbook*. Dec. 2007. ISBN: 978-0-16-079747-7.

[58] K. Ahlborn. “Durability of carbon fibre reinforced plastics with thermoplastic matrices under cyclic mechanical and cyclic thermal loads at cryogenic temperatures”. en. In: *Cryogenics* 31.4 (Apr. 1991), pp. 257–260. ISSN: 00112275. DOI: 10.1016/0011-2275(91)90088-E. URL: https://linkinghub.elsevier.com/retrieve/pii/001122759190088E (visited on 06/26/2024).

[59] J.G. Funk and G.F. Sykes. “The Effects of Simulated Space Environmental Parameters on Six Commercially Available Composite Materials”. en. In: (1989). URL: https://ntrs.nasa.gov/citations/19890010014.

[60] C.T. Sun and K.J. Yoon. “Elastic-Plastic Analysis of AS4/PEEK Composite Laminate Using a One-Parameter Plasticity Model”. en. In: *Journal of Composite Materials* 26.2 (Feb. 1992), pp. 293–308. ISSN: 0021-9983, 1530-793X. DOI: 10.1177/002199839202600208. URL: http://journals.sagepub.com/doi/10.1177/002199839202600208 (visited on 06/26/2024).

[61] W. Tan and B.G. Falzon. “Modelling the crush behaviour of thermoplastic composites”. en. In: *Composites Science and Technology* 134 (Oct. 2016), pp. 57–71. ISSN: 02663538. DOI: 10.1016/j.compscitech.2016.07.015. URL: https://linkinghub.elsevier.com/retrieve/pii/S026635381630745X (visited on 06/26/2024).

[62] L. Parnas and N. Katırcı. “Design of fiber-reinforced composite pressure vessels under various loading conditions”. en. In: *Composite Structures* 58.1 (Oct. 2002), pp. 83–95. ISSN: 02638223. DOI: 10.1016/S0263-8223(02)00037-5. URL: https://linkinghub.elsevier.com/retrieve/pii/S0263822302000375 (visited on 06/30/2024).

[63] G.D Brewer. “4.4 Fuel Containement System”. In: *Hydrogen Aircraft Technology*. CRC Press Inc., 1991, pp. 151–211.

[64] V. Jusko, S. Al Ghafri, and E. May. *BoilFAST*. 2024. URL: https://www.fsr.ecm.uwa.edu.au/software/boilfast/ (visited on 08/30/2024).

[65] *Plastics in Vacuum Applications*. 2022. URL: https://www.mtm-inc.com/plastics-in-vacuum-applications.html (visited on 07/20/2024).

[66] G. Calleja et al. “Where is the glass transition temperature of poly(tetrafluoroethylene)? A new approach by dynamic rheometry and mechanical tests”. en. In: *European Polymer Journal* 49.8 (Aug. 2013), pp. 2214–2222. ISSN: 00143057. DOI: 10.1016/j.eurpolymj.2013.04.028. URL: https://linkinghub.elsevier.com/retrieve/pii/S0014305713002164 (visited on 07/17/2024).

[67] M. Van De Voorde. “Results of physical tests on polymers at cryogenic temperatures”. en. In: *Cryogenics* 16.5 (May 1976), pp. 296–302. ISSN: 00112275. DOI: 10.1016/0011-2275(76)90321-0. URL: https://linkinghub.elsevier.com/retrieve/pii/0011227576903210 (visited on 08/06/2024).

[68] *Material Properties: Teflon*. URL: https://trc.nist.gov/cryogenics/materials/Teflon/Teflon_rev.htm (visited on 08/06/2024).

[69] A. Fischer and B. Mermelstein. “A compilation of low outgassing polymeric materials normally recommended for GSFC cognizant spacecraft”. In: (July 1971). URL: https://ntrs.nasa.gov/citations/19710027437.

[70] M. B. Kasen et al. “Mechanical, Electrical, and Thermal Characterization of G-10Cr and G-11Cr Glass-Cloth/Epoxy Laminates Between Room Temperature and 4 K”. In: *Advances in Cryogenic Engineering Materials: Volume 26*. Ed. by A. F. Clark and R. P. Reed. Boston, MA: Springer US, 1980, pp. 235–244. ISBN: 978-1-4613-9859-2. DOI: 10.1007/978-1-4613-9859-2_24. URL: https://doi.org/10.1007/978-1-4613-9859-2_24.

[71] Lesjofors. *The Sping Catalogue #15*. URL: https://www.lesjoforsab.com/wp-content/uploads/downloads/stock-springs-catalogue/lesjofors_stockspring_catalogue_-no15_2020.pdf (visited on 07/26/2024).

[72] R.P. Reed and M. Golda. “Cryogenic composite supports: a review of strap and strut properties”. en. In: *Cryogenics* 37.5 (May 1997), pp. 233–250. ISSN: 00112275. DOI: 10.1016/S0011-2275(97)00004-0. URL: https://linkinghub.elsevier.com/retrieve/pii/S0011227597000040 (visited on 04/12/2024).

[73] J. O. Almen and A. Laszlo. “The Uniform-Section Disk Spring”. en. In: *Journal of Fluids Engineering* 58.4 (May 1936), pp. 305–314. ISSN: 0097-6822. DOI: 10.1115/1.4020233. URL: https://asmedigitalcollection.asme.org/fluidsengineering/article/58/4/305/1158146/The-Uniform-Section-Disk-Spring (visited on 07/27/2024).

[74] *Fiber Rope Termination*. 2023. URL: https://www.applied-fiber.com/product-options/fiber-rope-termination/.

[75] P. J. Shirron et al. “Design and predicted performance of the 3-stage ADR for the Soft-X-ray Spectrometer instrument on Astro-H”. en. In: *Cryogenics* 52.4-6 (Apr. 2012), pp. 165–171. ISSN: 00112275. DOI: 10.1016/j.cryogenics.2012.01.019. URL: https://linkinghub.elsevier.com/retrieve/pii/S0011227512000203 (visited on 07/08/2024).

[76] D. Madier. “Defining Finite Element Analysis”. In: *Practical Finite Element Analysis for Mechanical Engineers*. First Edition. FEA Academy, 2020. ISBN: 978-1-9990475-0-4.

[77] D. Madier. “The Library of Elements”. In: *Practical Finite Element Analysis for Mechanical Engineers*. First Edition. FEA Academy, 2020, pp. 115–151. ISBN: 978-1-9990475-0-4.

[78] D. Madier. “Meshing”. In: *Practical Finite Element Analysis for Mechanical Engineers*. First Edition. FEA Academy, 2020, pp. 153–193. ISBN: 978-1-9990475-0-4.

[79] D. Madier. “Normal Mode Analysis”. In: *Practical Finite Element Analysis for Mechanical Engineers*. First Edition. FEA Academy, 2020, pp. 583–598. ISBN: 978-1-9990475-0-4.

[80] *Material Properties: Kevlar 49 (Fiber)*. URL: https://trc.nist.gov/cryogenics/materials/Kevlar49/kevlarfiber.htm (visited on 08/06/2024).

[81] *Material Properties: G-10 CR (Fiberglass Epoxy)*. URL: https://trc.nist.gov/cryogenics/materials/G-10%20CR%20Fiberglass%20Epoxy/G10CRFiberglassEpoxy_rev.htm (visited on 07/24/2024).

A

Thermodynamic Derivation

For a dormant tank, there is no mass flow in or out of the tank ($\dot{m}_{H_2}^{in} = \dot{m}_{H_2}^{out} = 0$) and no work from an electric heating element ($W_{electric} = 0$). Although, the presence of parasitic heat leakage is unavoidable ($Q_{leak} \neq 0$). In differential form, the energy balance used for the dormancy model is given as:

$$\frac{d(m_{H_2} u_{H_2})}{dt} = Q_{leak} \tag{A.1}$$

Namely, the change in the system's internal energy is solely caused by parasitic heat leakage from the environment.
The mass of the hydrogen in the tank, when present as a gas-liquid mixture is given as:

$$m_{H_2} = m_g + m_l \tag{A.2}$$

The total internal energy within the tank can be also be written as:

$$m_{H_2} u_{H_2} = m_g u_g + m_l u_l \tag{A.3}$$

The enthalpy of fluid, H, defined as the sum of its internal energy and the product of its pressure and volume:

$$h = u + Pv = u + P/\rho \tag{A.4}$$

Combining A.3 and letting $u = h - P/\rho$ from equation A.4 in the energy balance equation of A.1:

$$\frac{d(m_{H_2} U_{H_2})}{dt} = \frac{d(m_g h_g)}{dt} + \frac{d(m_l h_l)}{dt} - \frac{d\left(m_g \frac{P}{\rho_g}\right)}{dt} - \frac{d\left(m_l \frac{P}{\rho_l}\right)}{dt} = Q_{leak} \tag{A.5}$$

The enthalpy, mass and densities of the gas and liquid, and the homogeneous pressure are all functions of the time. Isolating and expanding each of the terms in A.5 gives:

$$\begin{aligned}
\frac{d(m_g h_g)}{dt} &= (h_g)\frac{dm_g}{dt} + (m_g)\frac{dh_g}{dt} \\
\frac{d(m_l h_l)}{dt} &= (h_l)\frac{dm_l}{dt} + (m_l)\frac{dh_l}{dt} \\
\frac{d\left(m_g \frac{P}{\rho_g}\right)}{dt} &= \left(\frac{P}{\rho_g}\right)\frac{dm_g}{dt} + (m_g P)\frac{d(1/\rho_g)}{dt} + \left(\frac{m_g}{\rho_g}\right)\frac{dP}{dt} \\
\frac{d\left(m_l \frac{P}{\rho_l}\right)}{dt} &= \left(\frac{P}{\rho_l}\right)\frac{dm_l}{dt} + (m_l P)\frac{d(1/\rho_l)}{dt} + \left(\frac{m_g}{\rho_l}\right)\frac{dP}{dt}
\end{aligned} \tag{A.6}$$

Using the expanded terms of A.6 and noting that $\frac{d(1/\rho)}{dt} = \frac{-1}{\rho^2}\frac{d\rho}{dt}$, the energy balance from equation A.1 becomes,

$$(h_g - h_l)\frac{dm_g}{dt} + (m_g)\frac{dh_g}{dt} + (m_l)\frac{dh_l}{dt} - \left(\frac{m_g}{\rho_g} + \frac{m_l}{\rho_l}\right)\frac{dP}{dt} - P\left(\frac{1}{\rho_g}\frac{dm_g}{dt} + \frac{1}{\rho_l}\frac{dm_l}{dt} - \left(\frac{m_g}{\rho_g^2}\frac{d\rho_g}{dt} + \frac{m_l}{\rho_l^2}\frac{d\rho_l}{dt}\right)\right) = Q_{leak} \tag{A.7}$$

Equation A.7 can be simplified considerably by introducing an equation for the total volume, V, and by also considering that change of the volume over time is equal to zero. Namely,

$$V = V_g + V_l = \frac{m_g}{\rho_g} + \frac{m_l}{\rho_l} \tag{A.8}$$

$$\frac{dV}{dt} = \left(\frac{1}{\rho_g}\frac{dm_g}{dt} + \frac{1}{\rho_l}\frac{dm_l}{dt} - \left(\frac{m_g}{\rho_g^2}\frac{d\rho_g}{dt} + \frac{m_l}{\rho_l^2}\frac{d\rho_l}{dt}\right)\right) = 0 \tag{A.9}$$

Hence, equation A.7 simplifies down to,

$$(h_g - h_l)\frac{dm_g}{dt} + (m_g)\frac{dh_g}{dt} + (m_l)\frac{dh_l}{dt} - (V)\frac{dP}{dt} = Q_{leak} \tag{A.10}$$

We require expression for $\frac{dh_g}{dt}$ and $\frac{dh_l}{dt}$. In thermodynamic theory, the state postulate expresses that the state (i.e properties) of a substance is fully defined by any two intensive properties such as the temperature, pressure, and density. In this analysis, the two intensive properties chosen are temperature and pressure. Namely, $h = h(P, T)$. The differential forms lead to the following partial differential equations:

$$\begin{aligned}
\frac{dh_g}{dt} &= \left(\frac{\partial h_g}{\partial P}\right)_T \frac{dP}{dt} + \left(\frac{\partial h_g}{\partial T}\right)_P \frac{dT}{dt} \\
\frac{dh_l}{dt} &= \left(\frac{\partial h_l}{\partial P}\right)_T \frac{dP}{dt} + \left(\frac{\partial h_l}{\partial T}\right)_P \frac{dT}{dt}
\end{aligned} \tag{A.11}$$

Furthermore, since the gas-liquid mixture is assumed to be a saturated mixture, the pressure in the tank is always equal to the saturated pressure at a given temperature. Namely, $P = P_s(T)$. In differential form we get:

$$\frac{dP}{dt} = \left(\frac{dP_s}{dT}\right)\frac{dT}{dt} \tag{A.12}$$

Combining, equations A.12, A.11, and A.10, the following relation for the change of temperature over time is obtained:

$$\frac{dT}{dt} = \frac{(h_l - h_g)\frac{dm_g}{dt} + Q_{leak}}{m_l \left(\frac{\partial h_l}{\partial T}\right)_P + m_g \left(\frac{\partial h_g}{\partial T}\right)_P + \left(m_l \left(\frac{\partial h_l}{\partial P}\right)_T + m_g \left(\frac{\partial h_g}{\partial T}\right) - V\right)\frac{dP_s}{dT}} \tag{A.13}$$

We can get an expression for the rate of change of the gas mass over time by reconsidering equation A.9. In addition, as was done for the enthalpy, we can get expressions for $\frac{\rho_g}{dt}$ and $\frac{\rho_l}{dt}$:

$$\begin{aligned} \frac{d\rho_g}{dt} &= \left(\frac{\partial \rho_g}{\partial P}\right)_T \frac{dP}{dt} + \left(\frac{\partial \rho_g}{\partial T}\right)_P \frac{dT}{dt} \\ \frac{d\rho_l}{dt} &= \left(\frac{\partial \rho_l}{\partial P}\right)_T \frac{dP}{dt} + \left(\frac{\partial \rho_l}{\partial T}\right)_P \frac{dT}{dt} \end{aligned} \tag{A.14}$$

Combining equations A.14 and A.9, we get:

$$\frac{dm_g}{dt} = \frac{\frac{m_g}{\rho_g^2}\left(\left(\frac{\partial \rho_g}{\partial P}\right)_T \frac{dP}{dt} + \left(\frac{\partial \rho_g}{\partial T}\right)_P \frac{dT}{dt}\right) + \frac{m_l}{\rho_l^2}\left(\left(\frac{\partial \rho_l}{\partial P}\right)_T \frac{dP}{dt} + \left(\frac{\partial \rho_l}{\partial T}\right)_P \frac{dT}{dt}\right)}{\left(\frac{1}{\rho_g} - \frac{1}{\rho_l}\right)} \tag{A.15}$$

In a closed system, the increase in the mass of the gas due to continuous vaporization corresponds to a loss of mass in the liquid phase. Consequently, the following relationship holds:

$$\frac{dm_l}{dt} = -\frac{dm_g}{dt} \tag{A.16}$$

The thermodynamic state of hydrogen within a tank can be determined by solving the following system of coupled ordinary differential equations. These equations describe the transient evolution of pressure, temperature, and the masses of gas and liquid phases.

$$\begin{aligned} \frac{dP}{dt} &= \left(\frac{dP_s}{dT}\right)\frac{dT}{dt} \\ \frac{dm_g}{dt} &= \frac{\frac{m_g}{\rho_g^2}\left(\left(\frac{\partial \rho_g}{\partial P}\right)_T \frac{dP}{dt} + \left(\frac{\partial \rho_g}{\partial T}\right)_P \frac{dT}{dt}\right) + \frac{m_l}{\rho_l^2}\left(\left(\frac{\partial \rho_l}{\partial P}\right)_T \frac{dP}{dt} + \left(\frac{\partial \rho_l}{\partial T}\right)_P \frac{dT}{dt}\right)}{\left(\frac{1}{\rho_g} - \frac{1}{\rho_l}\right)} \\ \frac{dm_l}{dt} &= -\frac{dm_g}{dt} \\ \frac{dT}{dt} &= \frac{(h_1 - h_g)\frac{dm_g}{dt} + Q_{leak}}{m_l \left(\frac{\partial h_l}{\partial T}\right)_P + m_g \left(\frac{\partial h_g}{\partial T}\right)_P + \left(m_l \left(\frac{\partial h_l}{\partial P}\right)_T + m_g \left(\frac{\partial h_g}{\partial T}\right) - V\right)\frac{dP_s}{dT}} \end{aligned} \tag{A.17}$$

Where,

- h_g, h_l = Specific enthalpy of gaseous hydrogen and mass of liquid hydrogen, respectively [J/kg]
- m_g, m_l = Mass of gaseous hydrogen and mass of liquid hydrogen, respectively [kg]
- P = Homogeneous pressure [Pa]
- P_s = Saturated pressure at a given temperature [Pa]
- Q_{leak} = Heat leakage in the tank [W]
- ρ_g, ρ_l = Density of gaseous hydrogen and mass of liquid hydrogen, respectively [kg/m^3]
- T = Homogeneous temperature [K]
- u_{H_2}= Specific internal energy of the hydrogen in the tank [J/kg]
- V = Internal volume of the tank [m^3]

Equations A.17 can be manipulated algebraically to calculate the derivatives incrementally. In other words, they can be rearranged into the form [A][X] = [C], where [X] represents the vector containing the values of *dP/dt*, *dT/dt*, *dmg/dt*, *dml/dt* and is solved at each time step.

B

Python Code for Self-Pressurization

The following code is the implementation of the Ahluwalia et al. analytical equations to calculate the self-pressurization of LH2 vessel [41]. The module ”CoolProp” was used to retrieve properties of gaseous and liquid hydrogen.

```
import CoolProp.CoolProp as CP # Used to get properties of Hydrogen
import numpy as np
import matplotlib.pyplot as plt

# Defining the Scenarios
# Q_leak is the amount of heat leakage entering the vessel.
# Fill ratio is the percentage of LH2 at the start.
scenarios = [
    {'fill_ratio': 0.40, 'Q_leak': 36.5},
    {'fill_ratio': 0.80, 'Q_leak': 36.5},
    {'fill_ratio': 0.40, 'Q_leak': 1.5},
    {'fill_ratio': 0.80, 'Q_leak': 1.5}
]

Pvent = 6.5*100000 # Convert from Bar to Pa for the venting pressure
stratification_factor = 2 #Doubles the pressure rate for each increment

fig, ax = plt.subplots(figsize=(10, 6))

# List of vertical offsets for annotations to avoid overlapping
offsets = [-0.1, -0.2, 0.1, 0.2]

# Iterate over each scenario
for idx, scenario in enumerate(scenarios):
    fill_ratio_initial = scenario['fill_ratio']
    Q_leak = scenario['Q_leak']

    # Initial conditions
    P0 = 101000 # Initial pressure in Pa
```

```
T0 = CP.PropsSI('T', 'P', P0, 'Q', 0.1, 'ParaHydrogen') # Initial temperature in K
V = 0.091 # Volume in m^3

# Initial masses of gas and liquid hydrogen
mg0 = CP.PropsSI('D', 'T', T0, 'Q', 1, 'ParaHydrogen')*V*(1-fill_ratio_initial) # kg
ml0 = CP.PropsSI('D', 'T', T0, 'Q', 0, 'ParaHydrogen')*V*(fill_ratio_initial) # kg

# Initial densities and enthalpies of gas and liquid hydrogen
rhog0 = CP.PropsSI('D', 'T', T0, 'Q', 1, 'ParaHydrogen')# density of gas
rhol0 = CP.PropsSI('D', 'T', T0, 'Q', 0, 'ParaHydrogen')#density
hg0 = CP.PropsSI('H', 'T', T0, 'Q', 1, 'ParaHydrogen')#kJ/kg
hl0 = CP.PropsSI('H', 'T', T0, 'Q', 0, 'ParaHydrogen')#kJ/kg

# Initial vapor quality
x0 = mg0/(mg0+ml0) #unitless

# Store initial conditions
initial_conditions = [P0, T0, mg0, ml0]

# Initialize lists to store time series data
P = [P0]
T = [T0]
mg = [mg0]
ml = [ml0]
rhog = [rhog0]
rhol = [rhol0]
hg = [hg0]
hl = [hl0]
x = [x0]
Ps = [P0]
time = [0]

dt = 250 # Time step in seconds

# Run the simulation until the pressure reaches the venting pressure
while P[-1]<Pvent:
    # Compute derivatives
    delrhog_delP = CP.PropsSI('d(D)/d(P)|T', 'T', T[-1], 'Q', 1, 'ParaHydrogen')
    delrhol_delP = CP.PropsSI('d(D)/d(P)|T', 'T', T[-1], 'Q', 0, 'ParaHydrogen')
    delrhog_delT = CP.PropsSI('d(D)/d(T)|P', 'P', P[-1], 'Q', 1, 'ParaHydrogen')
    delrhol_delT = CP.PropsSI('d(D)/d(T)|P', 'P', P[-1], 'Q', 0, 'ParaHydrogen')
    delhg_delP = CP.PropsSI('d(H)/d(P)|T', 'T', T[-1], 'Q', 1, 'ParaHydrogen')
    delhl_delP = CP.PropsSI('d(H)/d(P)|T', 'T', T[-1], 'Q', 0, 'ParaHydrogen')
    delhg_delT = CP.PropsSI('d(H)/d(T)|P', 'P', P[-1], 'Q', 1, 'ParaHydrogen')
    delhl_delT = CP.PropsSI('d(H)/d(T)|P', 'P', P[-1], 'Q', 0, 'ParaHydrogen')

    # Small temperature increment to calculate the rate of pressure change with temperature
    T_increment = 6.5e-06
    T_new = T[-1]+T_increment
    P_new = CP.PropsSI('P', 'T', T_new, 'Q', 0.1, 'ParaHydrogen')
    dPs_dT = (P_new-P[-1])/(T_new-T[-1])
```

```
    # Construct the coefficient matrix A
    A21 = -(((mg[-1]/(rhog[-1]**2))*delrhog_delP)+
           ((ml[-1]/(rhol[-1]**2))*delrhol_delP))
    A22 = -(((mg[-1]/(rhog[-1]**2))*delrhog_delT)+
           ((ml[-1]/(rhol[-1]**2))*delrhol_delT))
    A42 = (ml[-1]*delhl_delT)+(mg[-1]*delhg_delT)\
         +(((ml[-1]*delhl_delP)+(mg[-1]*delhg_delP)-V)*dPs_dT)

    A = np.array([[1, -dPs_dT, 0, 0],
                  [A21, A22, (1/rhog[-1])-(1/rhol[-1]), 0],
                  [0, 0, 1, 1],
                  [0, A42, -(hl[-1]-hg[-1]), 0]])

    # Construct the B matrix
    B = np.array([[0],
                  [0],
                  [0],
                  [Q_leak]])

    # Solve the system of linear equations
    differential_matrix = np.linalg.solve(A, B)
    dP_dt = differential_matrix[0, 0]*stratification_factor
    dT_dt = differential_matrix[1, 0]
    dmg_dt = differential_matrix[2, 0]
    dml_dt = differential_matrix[3, 0]

    # Update the state variables
    P.append(P[-1]+(dt*dP_dt))
    T.append(CP.PropsSI('T', 'P', P[-1], 'Q', 0.1, 'ParaHydrogen'))
    if mg[-1]+(dt*dmg_dt)<=0:
        mg.append(0)
    else:
        mg.append(mg[-1]+(dt*dmg_dt))
    ml.append(ml[-1]+(dt*dml_dt))
    x.append(mg[-1]/(mg[-1]+ml[-1]))
    rhog.append(CP.PropsSI('D', 'P', P[-1], 'Q', 1, 'ParaHydrogen'))
    rhol.append(CP.PropsSI('D', 'P', P[-1], 'Q', 0, 'ParaHydrogen'))
    hg.append(CP.PropsSI('H', 'P', P[-1], 'Q', 1, 'ParaHydrogen'))
    hl.append(CP.PropsSI('H', 'P', P[-1], 'Q', 0, 'ParaHydrogen'))
    Ps.append(CP.PropsSI('P', 'T', T[-1], 'Q', 0.5, 'ParaHydrogen'))
    time.append(time[-1]+dt)

# Convert time to hours and pressure to bars for plotting
time_hours = np.array(time)/3600
P_bars = np.array(P)/100000 # Convert pressure from Pa to bars

# Plot the pressure vs time for each scenario
label = f'Fill Rate: {fill_ratio_initial*100}%, Heat Load: {Q_leak} W'
ax.plot(time_hours, P_bars, label=label)
```

```
# Set labels with increased font size
ax.set_xlabel('Time (hours)', fontsize=14)
ax.set_ylabel('Pressure (Bar)', fontsize=14)
ax.set_title('Pressure Rise vs Time for Different Initial Fill Levels and Heat Leaks',
    fontsize=14)
ax.legend()
ax.set_xlim(0, 50)
ax.set_ylim(0.5, 7.3)

plt.show()
```

C

Effective temperature of the non-equilibrium gas

Corrucini [36] defines the temperature ,T, in the denominator of equation 2.16 as:

$$\frac{1}{\sqrt{T}} = \left(\frac{A_1}{A_1 + A_2}\right)\frac{1}{\sqrt{T_1'}} + \left(\frac{A_2}{A_1 + A_2}\right)\frac{1}{\sqrt{T_2'}} \tag{C.1}$$

With,

$$T'_1 = \frac{a_1 T_1[(1-a_2)A_1/A_2 + a_2] + a_2(1-a_1)T_2}{a_2 + a_1(1-a_2)A_1/A_2} \tag{C.2}$$

$$T'_2 = \frac{a_1 T_1(1-a_2)A_1/A_2 + a_2 T_2}{a_2 + a_1(1-a_2)A_1/A_2} \tag{C.3}$$

D

Thermal radiation using the Gebhart method

Considering a double-walled vessel. The cold surface (outer surface of inner vessel) shall be denoted as 1 and the hot surface (inner surface of outer shell) as 2. Typically, the following is known:

- ϵ_1, ϵ_2 = Emissivity surface 1 and 2
- T_1, T_2 = Temperature of surface 1 and 2 [K]
- A_1, A_2 = Area of surface 1 and 2 [m^2]
- F_{11} = 0
- F_{12} = 1
- F_{21} = $(A_1/A_2) \cdot F_{12}$
- F_{22} = $1 - F_{21}$

Using the following relation for to get the Gebhart factors:

$$B_{ij} = F_{ij} \cdot \epsilon_j + \sum_{k=1}^{N}((1 - \epsilon_k) \cdot F_{ik} \cdot B_{kj}) \tag{D.1}$$

Where,

- F_{ij} = View factor from surface i to j
- ϵ = Emissivity of the surface
- N = Amount of surfaces in the enclosure

$$B_{11} = F_{11}\epsilon_1 + (1 - \epsilon_1)F_{11}B_{11} + (1 - \epsilon_2)F_{12}B_{21} = (1 - \epsilon_2)F_{12}B_{21} \tag{D.2}$$

$$B_{12} = F_{12}\epsilon_2 + (1 - \epsilon_1)F_{11}B_{12} + (1 - \epsilon_2)F_{12}B_{22} = F_{12}\epsilon_2 + (1 - \epsilon_2)F_{12}B_{22} \tag{D.3}$$

$$B_{21} = F_{21}\epsilon_1 + (1 - \epsilon_1)F_{21}B_{11} + (1 - \epsilon_2)F_{12}B_{21} \tag{D.4}$$

$$B_{22} = F_{22}\epsilon_2 + (1-\epsilon_2)F_{21}B_{12} + (1-\epsilon_2)F_{22}B_{22} \tag{D.5}$$

Inserting B_{11} from equation D.2 into equation D.4 and solving for B_{21}:

$$B_{21} = \frac{F_{21}\epsilon_1}{(1-(1-\epsilon_1)(1-\epsilon_2)F_{21}F_{12} - (1-\epsilon_2)F_{22})} \tag{D.6}$$

It is then possible to solve for B_{11} through equation D.2.

Noting that the sum of the Gebhart factors for a given surface must be equal to 1, we get:

$B_{12} = 1 - B_{11}$
$B_{22} = 1 - B_{21}$

Finally, the energy transfer from surface 2 to surface 1 is formulated as:

$$Q_{21} = \epsilon_2 \cdot A_2 \cdot B_{21} \cdot \sigma \cdot (T_2^4 - T_1^4) = -(\epsilon_1 \cdot A_1 \cdot B_{12} \cdot \sigma \cdot (T_1^4 - T_2^4)) \tag{D.7}$$

Where,

- $Q21$ = Energy transfer from surface 2 to 1 [W]
- ϵ = Emissivity of surface
- A = Area of surface [m^2]
- B = Gebhart factor
- $\sigma = 5.670x10^{-8}$, Stefan-Boltzmann constant [W/m^2K^4]
- T_i,T_j = Temperatures of surface i and j, respectively [K]